All-Mechanical Receivers

Ruonan Liu

Electrical Engineering and Computer Sciences
University of California at Berkeley

December 1, 2019

All-Mechanical Receivers

by

Ruonan Liu

A dissertation submitted in partial satisfaction of the

requirements for the degree of

Doctor of Philosophy

in

Engineering – Electrical Engineering and Computer Sciences

in the

Graduate Division

of the

University of California, Berkeley

Committee in charge:

Professor Clark T.-C. Nguyen, Chair

Professor Tsu-Jae King Liu

Professor Liwei Lin

Fall 2017

Abstract

All-Mechanical Receivers

by

Ruonan Liu

Doctor of Philosophy in Engineering - Electrical Engineering and Computer Sciences

University of California, Berkeley

Professor Clark T.-C. Nguyen, Chair

In today's connected world, our lives depend heavily on information obtained from networks of sensor nodes and mobile devices. Billons of mobile devices are in communication over these networks at any given time. The trillion sensor vision calls for low-power, low-cost and small-sized wireless sensor nodes, posing ever-increasing constraints on the power consumption of wireless networks. Radio Frequency (RF) Microelectromechanical Systems (MEMS) offer one path towards nano-watt wireless communications.

This dissertation presents the first demonstration of an all-mechanical wireless receiver that employs a micromechanical resonant switch ("resoswitch") to consume zero quiescent power while listening and ~30nW while actively receiving. Here, high-Q mechanical resonance offers frequency selectivity, while mechanical impact switching provides amplification. The mechanical receiver successfully detects and demodulates (in an On-Off-Keying (OOK) fashion) Frequency-Shift-Keying (FSK)-modulated input signals down to -68dBm, a promising sensitivity for low-speed and low-power wireless applications. Because this receiver consumes no power while listening in standby, it obviates the sleep/wake cycles often used by low power sensor networks to save energy. It thus eliminates the need for continuously operating clocks that govern sleep/wake periods, thereby eliminating their power consumption.

If on the other hand one prefers to use more conventional mote transceivers that consume tens of milli-watts when on, then the sleep/wake strategy is paramount to save energy, and the clock sets the power bottleneck. A commercially available real time clock (RTC) typically consumes $1\mu W$ of power, which is considerably more than the tens of nano-watts more applicable for giant sensor networks. Fortunately, even when not used as a wireless transceiver, the all-mechanical circuit herein provides a solution to the clock problem, as well.

Specifically, the second part of this dissertation presents an RF powered wireless clock that feeds on a received FSK-modulated or Continuous-Wave input and generates a local clock output signal,

while consuming only 13nW of battery power, which is more than 50 times lower than an off-the-shelf RTC. Calculations further predict a three-order-of-magnitude power reduction if an on-chip next stage inverter replaces the off-chip discrete component in the current demonstration. The input capacitance of the off-chip inverter is 1.5pF, which translates to nano-watts of power for kilohertz clock frequencies. Use of an on-chip inverter with a few femto-Farads of input capacitance would reduce the power consumption to pico-watts.

Resoswitches as receivers or as clock generators, while very compelling, face several challenges that must be further explored before they can be commercially viable. For instance, the frequency stability of a resoswitch directly determines the error rate of a receiver or the stability of a clock. This frequency stability depends on perturbations of mechanical resonance impact dynamics that create unstable switching and instantaneous frequency jitter, a phenomena referred to as squegging. The quality factor, the contact material property, and the external excitation voltage all affect the squegging dynamics, but controlling these factors is not an easy task. On the other hand, manipulating the electrode configuration can also alter the squegging behavior, and is much easier to design and implement. This dissertation models and experimentally verifies observed squegging phenomena. The methods and models presented here provide a path to improving the stability of resoswitches towards commercial viability for use in future ultra-low power wireless networks.

Dedicated to my parents

Table of Contents

Chapter 1 INTRODUCTION

Trillion Sensor Universe – vision and challenge

As early as 1982 when a modified Coke machine became the first Internet-connected appliance, people have been exploring the concept of the Internet of Things (IoT) – networks of objects embedded with electronics that allow them to communicate and exchange information [1]. Connectivity is now an integral part of our lives. We rely on environments densely populated with sensors to aggregate information and create a multi-dimensional picture of our surroundings. Personal vehicles now have already on average about 100 sensors on board. The future self-driving cars will depend on sensors to navigate traffic and obstacles. The cell phones and electronic wearables today carry at least a dozen sensors from accelerometers to iris scanners. Temperature sensors, ambient sensors and motion sensors fill our smart homes. There are about 15 million connected sensors today, and 200 percent more every year [2]. Besides cost, energy consumption will likely pose a constraint on the network of a daunting number of sensors.

A coin cell battery carries 720J of energy. For a wireless sensor to last more than 1 year, the maximum average power consumption is about 22.8µW while most sensor motes on the market nowadays still consume milliwatts of power. At the same time, more wireless devices are joining the network. The notion of the trillion-sensor network envisions sensors positioned from the tops of buildings to the bottom of the ocean collecting data on air quality, traffic information, submarine earthquakes and so on. These applications call for an enormous number of sensors to cover the vast area. A coin cell battery costs at least 1 dollar today, which multiplies into trillion of dollars when accounting for the huge number of sensors in the network, quickly becoming impossible. Printed batteries offer a much cheaper alternative power source but the available energy decreases to about 1J only for a size of 30mm^2. For sensors to last 1 year, the average power consumption has to be less than 30nW, which is roughly five orders of magnitude lower than what is possible today! Within a sensor node, the wireless communication module is one of the main power consumers [3]. Developing low-power wireless communication technologies is a critical step towards realizing the vision of the trillion-sensor network. The following chapters focus on reducing the power consumption of the wireless receivers.

CHAPTER 1 INTRODUCTION

1.1 RECEIVER ARCHITECTURE

Figure 1(a) shows the schematic of a typical receiver front-end [4]. With millions of devices transmitting and receiving at a given time, the antenna sees a quite dynamic and crowded spectrum. It is the receiver front-end's job to isolate and magnify the signal of importance. A filter right after
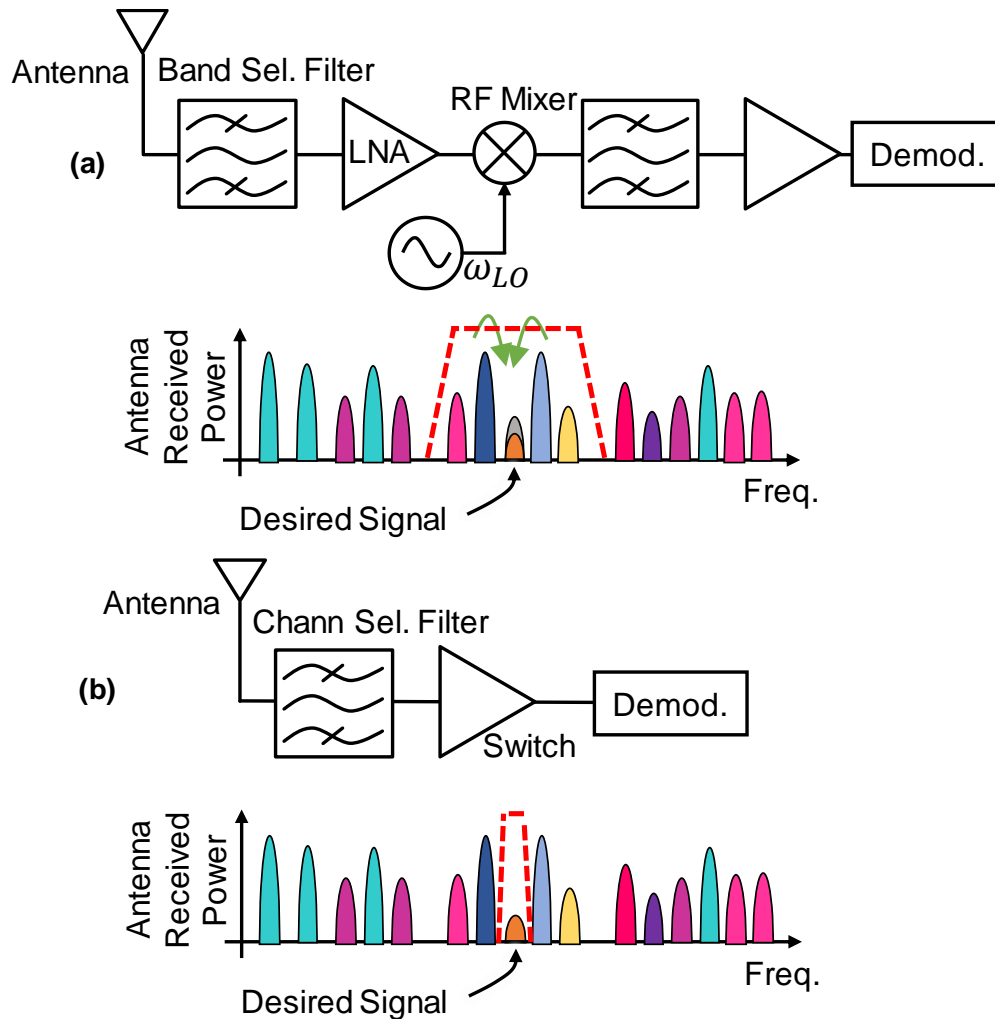
Figure 1: (a) The schematic of the traditional receiver architecture. The antenna picks up a crowded spectrum and the band select filter removes the interferers far from the desired signal. The amplifier needs to be linear across the dynamic range of all signals in band; otherwise, the strong interferers produce spurious signals that can mask the desired signal. The power consumption of the amplifier increases with the dynamic range. The more dynamic range the amplifier handles, the more power it burns. A second filter stage removes the rest of the interferers in band after mixing the signal to lower frequencies. (b) The schematic of a much simpler receiver architecture with a channel select front-end filter. If the channel select filter picks out only the desired signal in the very beginning, the amplifier can be as nonlinear as a switch that consume very little power. The channel-select filter removes all interferers before they can produce any spurious modes.

CHAPTER 1 INTRODUCTION

the antenna removes unwanted interferences and then an amplifier that follows boosts the power of the desired signal. At last, the receiver delivers the filtered and amplified signal to the final analog-to-digital converter and base-band processer. The seemingly straightforward receiver chain faces several challenges and power hogs. The input spectrum to the antenna usually includes high-power interferers close in frequency to the much weaker desired signal. Having a box shape filter that strictly excludes all adjacent frequency channels is extremely difficult to achieve with currently available technologies [5] in mobile devices. Rather, this front-end filter is usually a band-select filter, selecting a band of a few channels, suppressing the interferers far from the desired signal. Then after mixing down to lower intermediate frequency, a second filter stage removes the interferers close to the desired signal as shown in Figure 1(a). This method relaxes the requirement on the front-end filter, however, with the price of more stringent specifications on the amplifier. The input of the amplifier is now a band of signals that might contain strong interferers, together with a weak desired signal very close in frequency. In order for the power of the interferers not to leak into the frequency of the desired signal, the amplifier has to be linear over a large dynamic range, which consumes more power [6]. Therefore, the more interferers the front-end filter removes, the less dynamic range the amplifier has to handle and thus the lower the power consumption.

Since the dynamic range of the amplifier is proportional to the power consumption, using amplifiers as nonlinear as switches can save power. To accommodate the switch amplifier, the
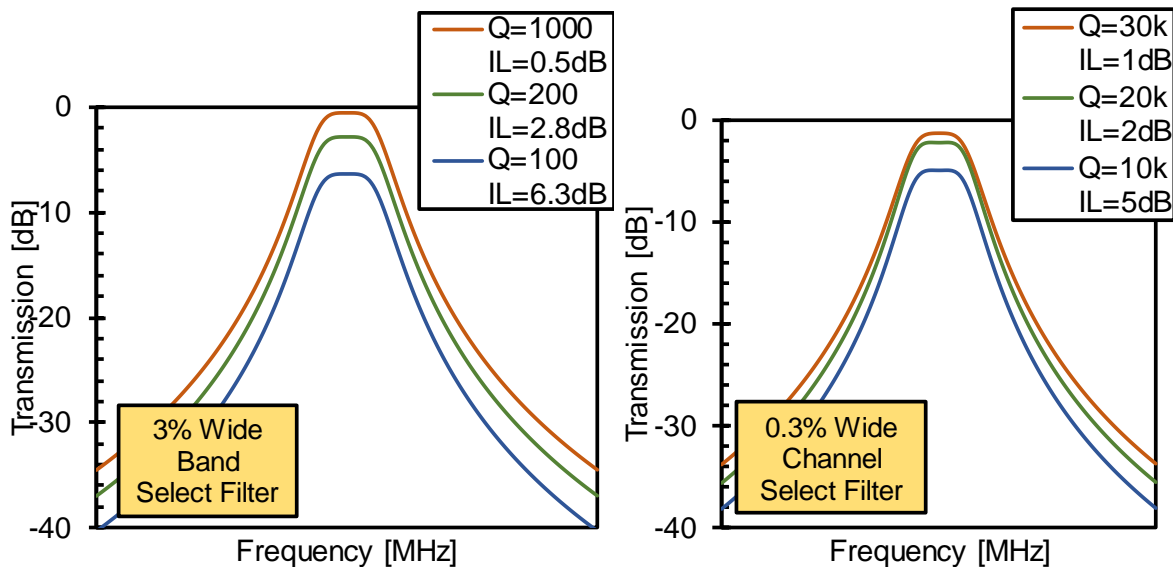
Figure 2: (Left): Frequency responses of a band select filter with a percent bandwidth of 3%. The insertion loss of the filter increases as the Q factor of the constituent resonator decreases. For Q factors of 100, 200 and 1000, the insertion loss is 6.3dB, 2.8dB, and 0.5dB respectively. (Right): Frequency responses of a chancel select filter with a percent bandwidth of 0.3% shows that even with resonators with Q of 30k, the filter suffers from an insertion loss of 1dB.

CHAPTER 1 INTRODUCTION

filter has to suppress all interferers as any interferers can create spurious signals that mask the desired signal through the nonlinear amplifier. For the filter to be able to select only the signal of interest, it has to have a narrow bandwidth with sharp roll-off as shown in Figure 1(b). The most common way to construct the front-end filter is to use several coupled resonators shown in Figure 3 in a half-ladder or cascade topology [7] [8]. The smaller the bandwidth, the higher the quality factor Q the composing resonators need to have in order to maintain the same insertion loss. Figure 2 shows the frequency response of the filters of percent bandwidth of 3%. If the constituent resonators have Q of 1000, the filter has insertion loss of 0.5dB. However, to have the same insertion loss, filters with percent bandwidth of 0.3% needs resonators with Q of over 30,000.

Researchers have studied many high Q resonators technologies [9] [10] [11], but the most promising approach is still the capacitive transduced Microelectromechanical Systems (MEMS) resonators, which easily achieve Qs of 100,000. Several previous works on capacitive MEMS filters [12] [13] [14] describe in details the design and implementation of channel-select filters using high Q resonators.

1.2 NONLINEAR AMPLIFIER

With the filter in place, the switch-like amplifier that follows the filter is also a capacitive resonator, shown in Figure 4. This type of device makes periodic switching contacts while operating on resonance. The input of the switch amplifier excites resonance and if the displacement is large enough to make contact, the output is periodically connecting to V_{DD}, generating large voltage gain. This switch takes an input signal at the resonance frequency and converts it into voltage spikes of amplitude V_{DD} of the same resonance frequency.

There are several distinctions between the resonant switch ("resoswitch") and the traditional RF MEMS switch, which makes the resoswitch a possible candidate for the front-end amplifier.
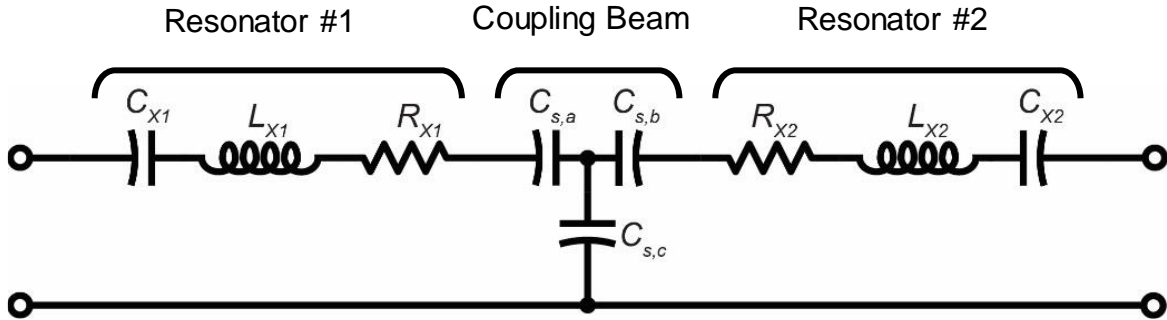

Figure 3: The electrical equivalent circuit of a filter composed of two resonators coupled with a mechanical coupling beam. The coupling beam is equivalent to three capacitors and each resonator is equivalent to a LCR resonance tank [76].

1.2.1 FREQUENCY SENSITIVITY – FILTER AMPLIFIER COMBINATION

The resoswitch amplifier provides gain to the desired signal at a specific frequency channel because the resoswitch responds to only the inputs close to its resonance frequency. Figure 4 shows the displacement frequency response of the resoswitch. The resonance behavior of the mechanical system dictates a biquad frequency response where the displacement reaches maximum at a characteristic resonance frequency with an amplitude Q times larger than when operating at off resonance frequencies. Therefore, only signals around the resonance frequency can excite switching and the resoswitch remains open for any signals outside resonance.

The resoswitch's inherent frequency selectivity is by itself a filtering process. Combined with the switching amplification, the resoswitch functions as a filter-amplifier. The biquad frequency response has a very narrow bandwidth dependent on the Q of the resonator and a very sloped roll-off. The simple single resonator filter can extend into a higher order filter where multiple resonators couple together to form a frequency response with sharper roll-off, providing rejection for interferers in the adjacent channel, and a better-defined pass band that satisfies the signal channel width and [15]. The resoswitch can potentially become a complete filter-switch front-end with the ability to select the desired frequency band and produce the gain needed to demodulate the input signal.

1.2.2 AMPLITUDE SENSITIVITY

As capacitive MEMS devices have Qs of 10,000, a fairly small input voltage on resonance excites enough displacement for the switch to produce an output of amplitude V_{DD}. One distinct difference between the resoswitch and a transistor-based amplifier is that the switch has a hard cut-off input level, below which the resoswitch produce no response at all. The minimum input level at which the resoswitch can switch and generate reliable output is the sensitivity of the resoswitch. The higher the Q, the smaller the input the resoswitch needs to reach a certain displacement. Capacitive resoswitches can have a better sensitivity benefiting from the large Q factors. Wireless receivers require sensitivity of at least -60dBm. Some mobile devices have harsh standard of -100dBm or even lower. Resoswitch based receivers, however preliminary, have demonstrated their ability to receive signals of close to -70dBm, which shows quite promising performance for low-speed wireless sensor applications.

1.3 ZERO QUIESCENT POWER

Linear amplifiers require bias in the middle of the linear gain region in order to take advantage of the high gain, but the biasing itself consumes currents even when the amplifier is idle. Switches have more abrupt a gain characteristic and toggle between on and off. The power consumption of the switching operation theoretically comes from only the dynamic charging and discharging of the load. In reality, when the switch is "off", the transistors still suffer from leakage currents. Although usually as small as a few nano-amperes, the leakage current is still bleeding nano-watts of power from the battery at all times. On the other hand, mechanical devices are by nature passive, which means zero power consumption at rest. Resoswitches are physically isolated from the contact electrodes by an air gap, therefore the leakage is almost negligible, which make resoswitch an ideal candidate for wireless receivers, especially for applications that require the sensors to listen at all times. For example, cell phones receivers are constantly listening so that they will not miss the incoming calls or messages that could happen at any random time.

Capacitive resoswitch require a DC bias voltage, to produce enough charges on the resonator. In this way, the ac input creates a varying electric field between the resonator and the input electrode that produces an electrostatic force and drives the resonator to move in resonance. When the resoswitch is listening, the bias voltage draws zero current, and thus consumes zero power.

1.4 RF POWERED CLOCK

Most of today's wireless sensor motes consume milli-watts of power when actively operating. In order for the sensors motes to sustain a meaningful lifetime on even a coin cell battery, they have to adopt a sleep/wake strategy where the wireless modules are in a low-power sleep mode most of the time and wake up to transmit/receive information on a predefined schedule. A real-time clock
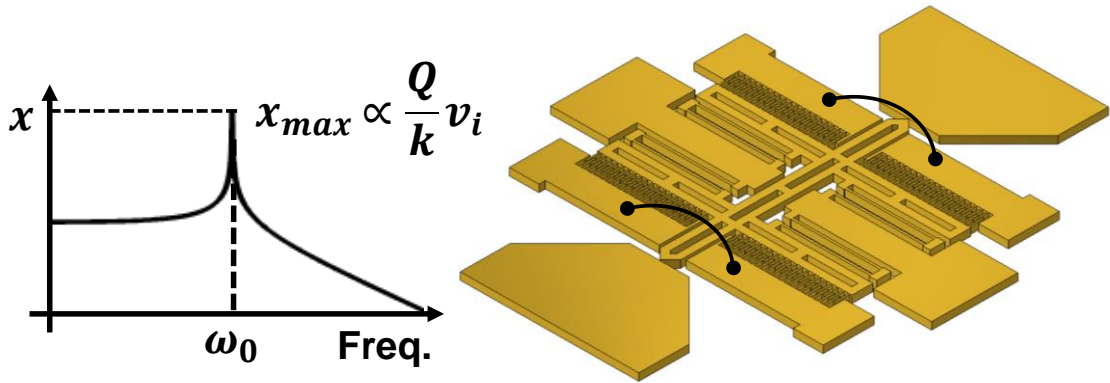

Figure 4: (Right) comb-driven resoswitch explained in detail in Chapter 2. k and v_i represent the stiffness of the resoswitch and the input voltage amplitude. (Left) the displacement frequency response of the resoswitch. At the resonance frequency ω_0, the displacement of the resoswitch is Q times larger than the displacement at low frequencies.

(RTC) runs continuously in the background even in sleep mode to make sure all sensor motes in the network wake up at the same time to communicate with each other. Therefore, the power bottleneck becomes the RTC. Clocks take the form of oscillators with positive feedback amplifiers, which are very power hungry components. In fact, a typical real-time clock (RTC) off the shelf on the market consumes 1µW of power, which is far over the power budget of the 30nW with a printed battery.

Since the mechanical receivers consume little power, they can effortlessly receive wireless clock signals as well. Time transfer already exist in radio watches and armature radios. In the United States, the WWVB station in NIST [16] broadcasts the national standard time kept by the atomic clocks at a carrier frequency of 60kHz. However, the current clock receivers in such watches consume hundreds of micro-watts of power, which is why the watches only turn on the receiver to synchronize the local time with the broadcast standard once every day or even every week to preserve power. The MEMS resoswitches consume nano-watts of power when actively receiving, offering an alternative for RTCs. Having negligible leakage, the only source of power consumption is the dynamic switching power. During each switching cycle, the resoswitch charges the loading capacitors to V_{DD}. At the resting cycle, another set of resoswitch discharges the loading capacitance to ground. The average power consumption is $P = C_{load}V_{DD}^2 f_{switch}$. The loading capacitance is highly dependent on the circuitry implementation of the next stage. For example, if the loading is an inverter gate that smooths out the switching output voltage spikes into square wave clock signals, then the power consumption when the wireless clock is actively receiving is in the range of pico-watts assuming a clock frequency of 1kHz, since an on-chip inverter's gate capacitance is as small as a few femto-Farads.

1.5 CHALLENGES OF RESOSWITCHES

Resoswitch consumes extremely little power when both actively receiving and just listening. However, as an integral part of the wireless communication, frequency stability is a determinant trait. The resoswitch combines the dynamics of resonance with the unpredictable mechanical impacts, which inevitable create disturbances to the resonance dynamics. The natural resonance frequency itself is only a function of material constants and geometric dimensions, creating a relatively stable frequency reference. The added impacts introduce perturbations that alter and can even destroy, under certain conditions, the natural resonance rhyme of the system. Designing and understanding the resoswitch's resonance impact dynamics is key to a stable receiver and a reliable clock generator. Chapter 2 discusses in details the effect of contacts on resonances.

1.6 REVIEW OF RESOSWITCHES

The concept of the resoswitch was first introduced in 2008 [17], demonstrated using a wineglass resonator. The goal is to reduce switch activation voltage and obtain better reliability comparing to traditional RF MEMS switch. The traditional MEMS switch has low stiffness in order to reduce the pull-in voltage. However, weak restoring force also makes the switch susceptible to stiction, which is one of the common causes of failure. The switch becomes stuck to the electrode permanently, degrading the switch's lifetime. The small stiffness also means a low natural frequency, which limits the response speed of the RF MEMS switch. Operating the switch on resonance offers the advantage of the Q-times gain in the displacement, leaving room for larger stiffness and thus stronger restoring force. The natural frequency also increases accordingly. The wineglass resoswitch successfully demonstrated trillions of hot switching cycles without failure. Even after the trillions of cycles of impact, the resoswitch simply drifts in frequency, instead of suffering a catastrophic failure.

The initial motivation of resoswitch is the application of power converters, specifically the DC-DC converter charge pump [18]. The MEMS switch provides higher charge pump efficiency, and can withstand higher DC breakdown voltage [19]. The resoswitches successfully demonstrated a five-stage charge pump charging from V_{DD} = 1V to 5V. Although the resoswitch charge pump requires an ac signal of several volts in amplitude due to the large contact resistance and under optimized switch design, it certainly was the first successful resoswitch application.

Resoswitch power amplifier is yet another demonstration of resoswitch's frequency selectivity and high Q amplification. Al slotted disks [20] resoswitches exhibit improved contact resistance and smaller parasitic resistance, which in turn reduces feedthrough currents. The open slots on wine-glass mode disks add to the displacement gain of the device and demonstrated an impressive Q factor of ~20,000 as well as a power gain of 13.8dB [21].

1.7 OVERVIEW

This dissertation focuses on the design, fabrication and characteristic of resoswitch for wireless receiver application. In addition to the well-studied capacitive resonator design, this dissertation explores perturbations of mechanical switching on resonance dynamics. Chapter 2 discusses in detail the phenomena of irregular switching and the design of the resoswitch to regulate resonance impacts. Chapter 3 describes the development of the microfabrication process in order to achieve high Q and low contact resistance at the same time. Chapter 4 and 5 address the experimental demonstrations of the zero-quiescent-power receiver and the RF powered clock. This is the first demonstration of a promising resoswitch filter amplifier capable of receiving FSK signal of -68dBm of power. The RF-power clock consumes only 13nW of power, which is order of

CHAPTER 1 INTRODUCTION

magnitude better than current available technology. Chapter 6 explains the efforts towards higher frequency receivers and outlines future work. At last, Chapter 7 concludes this dissertation with a summary and future projection.

Chapter 2 RESOSWITCH DESIGN

"Resoswitch" is short for resonant switch, a MEMS switch device. There has been a tremendous amount of research on RF MEMS switches for their low insertion loss, high isolation and negligible leakage current [22]. The MEMS switch is equivalent to a mass spring damper system. As an example, Figure 5 shows a MEMS cantilever. When the dc actuation voltage produces a large enough force, the cantilever pulls in and makes physical contact with the electrode underneath. The expression below describes the voltage amplitude ($V_{pull\text{-}in}$) it takes to close the switch:

$$V_{pull-in} = \sqrt{\left(\frac{8}{27}\frac{k_r d_0^3}{\epsilon A}\right)} \qquad (2.1)$$

where d_0 is the gap spacing and k is the stiffness of the cantilever. For a MEMS switch with a gap spacing of 100nm and a stiffness of 10 N/m, $V_{pull\text{-}in}$ is above 50V [23], which is much larger than what current IC technology can allow for. These switches usually require extra circuitries just to produce the high actuation voltage. In order to reduce $V_{pull\text{-}in}$, the MEMS switches are compliant and have very small gaps. Another challenge the MEMS switch faces is reliability. Unlike the diode based or transistor based switches where the lifetime is usually not a concern [24], MEMS switch contacts start to degrade after tens of thousands of cycles. One of the most common causes for failure is stiction. After the cantilever snaps into the electrode with a high velocity and makes contact, current flows through the mechanical contact points generating heat that causes the cantilever to stick to the electrode. The stiction problem is more severe for compliant structures, as the restoring forces are smaller so that the devices are more prone to stiction.

The resoswitch is different from the traditional RF MEMS switch, in its operating points. Instead of a dc $V_{pull\text{-}in}$, a voltage at the resonance frequency of the device drives it into periodic contact with the electrode. Figure 5 shows the frequency response of the resoswitch and the operating point of the RF MEMS switch versus the resoswitch. At resonance, the displacement of the device is Q times larger than the displacement at low frequencies close to dc, which reduces the actuation voltage by Q times given the same stiffness. Capacitively actuated resonators have Qs of hundreds of thousands, which allows room to stiffen the devices to improve their reliability.

2.1 Comb-Driven Resoswitch

Resoswitches are mechanical resonators with contact electrodes. Comb-driven resoswitches are comb-driven resonators [25] with mechanical stops as shown in Figure 6. The capacitive actuators between comb fingers generate forces in lateral directions that push the shuttle suspended by folded beams. The resonance frequency is:

$$\omega_0 = \sqrt{\left(\frac{k}{m_{eq}}\right)} \tag{2.2}$$

where m_{eq} is the equivalent mass of the comb-drive resonator, given by

$$m_{eq} = m_{shuttle} + \frac{1}{4}m_{truss} + \frac{12}{35}m_{beam} \tag{2.3}$$

The displacement of the shuttle on resonance under a voltage at f_0 is:

$$x_0 = \frac{QF_0}{k} \tag{2.4}$$

where F_0 is the force from the change of the capacitance between the comb fingers:
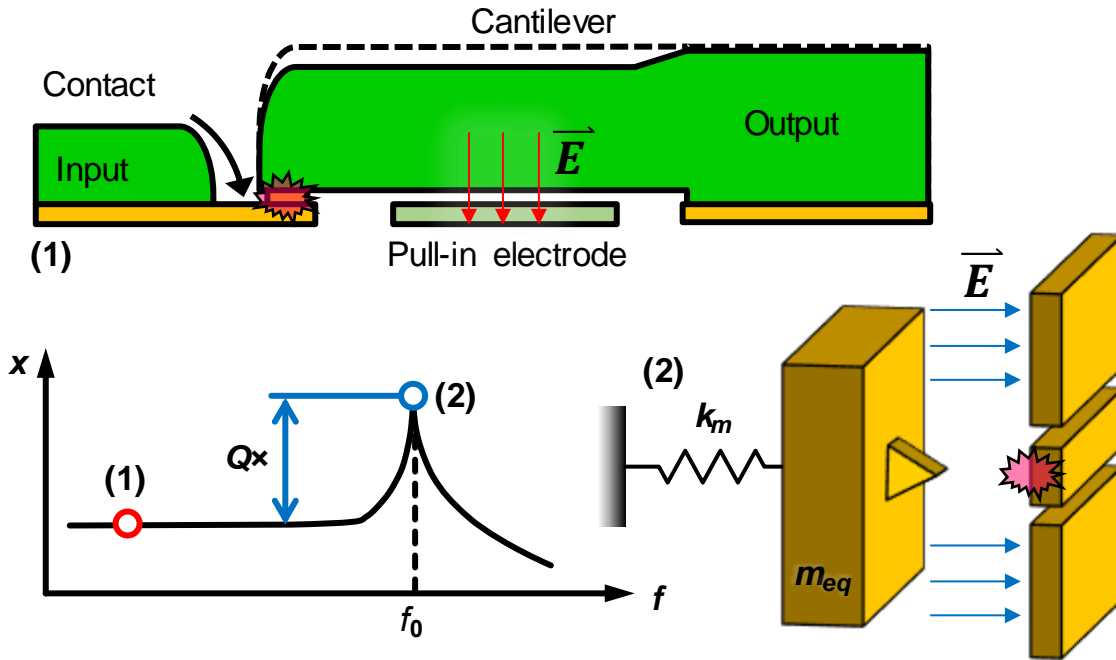
Figure 5 (1): A traditional RF MEMS switch that pulls into the input electrode when experiencing E field from voltages larger than $V_{pull\text{-}in}$. (2): Resonant switch (resoswitch) makes periodic contacts with output electrodes when experiencing E field at the resonance frequency. (3): The frequency response of the switches shows that the switch structure has Q times more displacement when the input is close to the resonance than when the input at low frequency.

$$F_0 = V_P v_i \frac{\partial C}{\partial x} \qquad (2.5)$$

where C is the overlap capacitance between the comb fingers: $C = \frac{N \epsilon L H}{d}$. N is the total number of fingers ϵ is the vacuum permittivity, H is the thickness of the structure and d is the gap spacing between fingers.

In order for the resoswitch to make contact, the minimum requirement is for the displacement of the shuttle to overcome the switch gap – the distance from the tips of the shuttle to the electrode. When the displacement grows just enough to reach the switch gap, $x_0 = g_{switch}$, where g_{switch} is the gap between the shuttle and the contact electrode, the shuttle reaches zero velocity when it touches the contact electrode, thus the contact resistance is enormous. As the displacement keeps increasing, the contact velocity also increases and contact resistance decreases. However, higher velocity impacts also degrade the contacts faster and cause more disturbance to the resonance dynamics. Specifically, every time the shuttle collides with the electrode, it changes its course and picks up a sudden change in phase, which negatively affects the harmony between the driving force and the shuttle's displacement dynamics. The exact impact mechanism depends on many factors such as the contact surfaces area, contact material, surface asperities and so on. To study and predict the interaction of impact and resonance, contact models with proper assumptions are necessary.

2.2 IMPACT DYNAMICS - SQUEGGING

The sudden change in transient responses is usually very difficult to model. Starting from the simplest impact mechanism, where the contact is completely elastic, the shuttle bounces back from
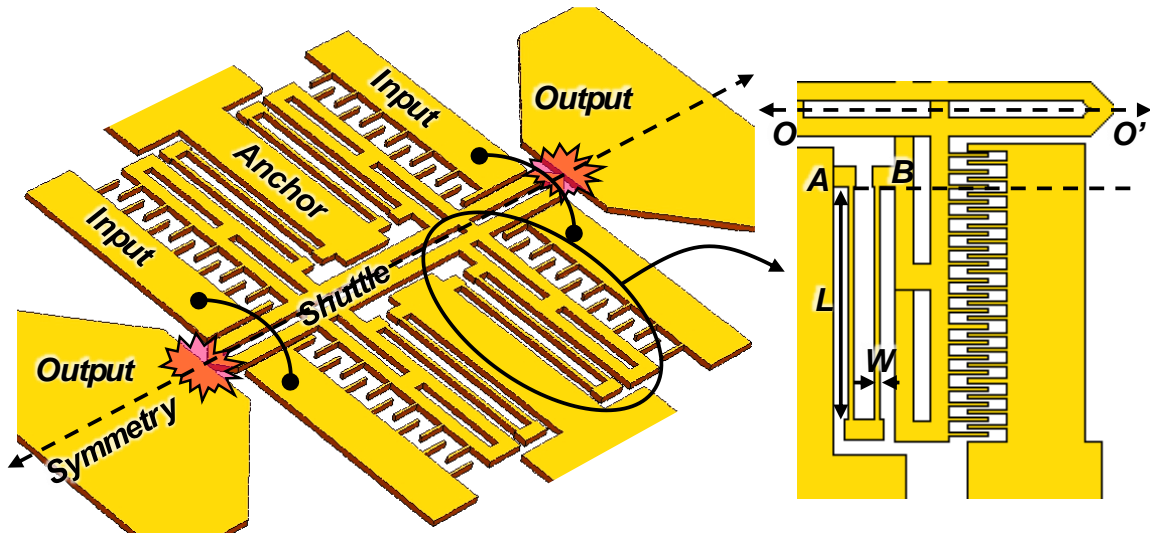
Figure 6: A comb-driven resoswitch is composed of a comb-driven resonator and contact electrodes at the tip of the shuttle.

CHAPTER 2 RESOSWITCH DESIGN

the electrode with the same velocity in magnitude but opposite in direction. At all times, the governing equation of the periodically forced second order system holds:

$$m_{eq}a(t) + bv(t) + kx(t) = F_0\cos(\omega_{drive}t) \tag{2.6}$$

where ω_{drive} is the input drive frequency and $\omega_{drive} = \omega_0$ if driving on resonance. When the shuttle's displacement $x(t) > g_{switch}$, $v(t + \Delta t) = -rv(t)$ where Δt is the sampling time or the time step in transient response and r is the restitution factor, which is a function of impact condition, such as contact material, contact velocity etc. As shown in Figure 7, the resonator follows the

Figure 7 (a): Transient response of a free moving resonator with no contact electrode. (b): With contact electrode, the resoswitch misses contacts every few cycles – squegging. (c): An overlay plot of the transient responses of a free resonator, an impacting resonator and the external excitation force.

forced resonance except when the displacement reaches the switch gap and changes the velocity instantly. Impact is an inheritably nonl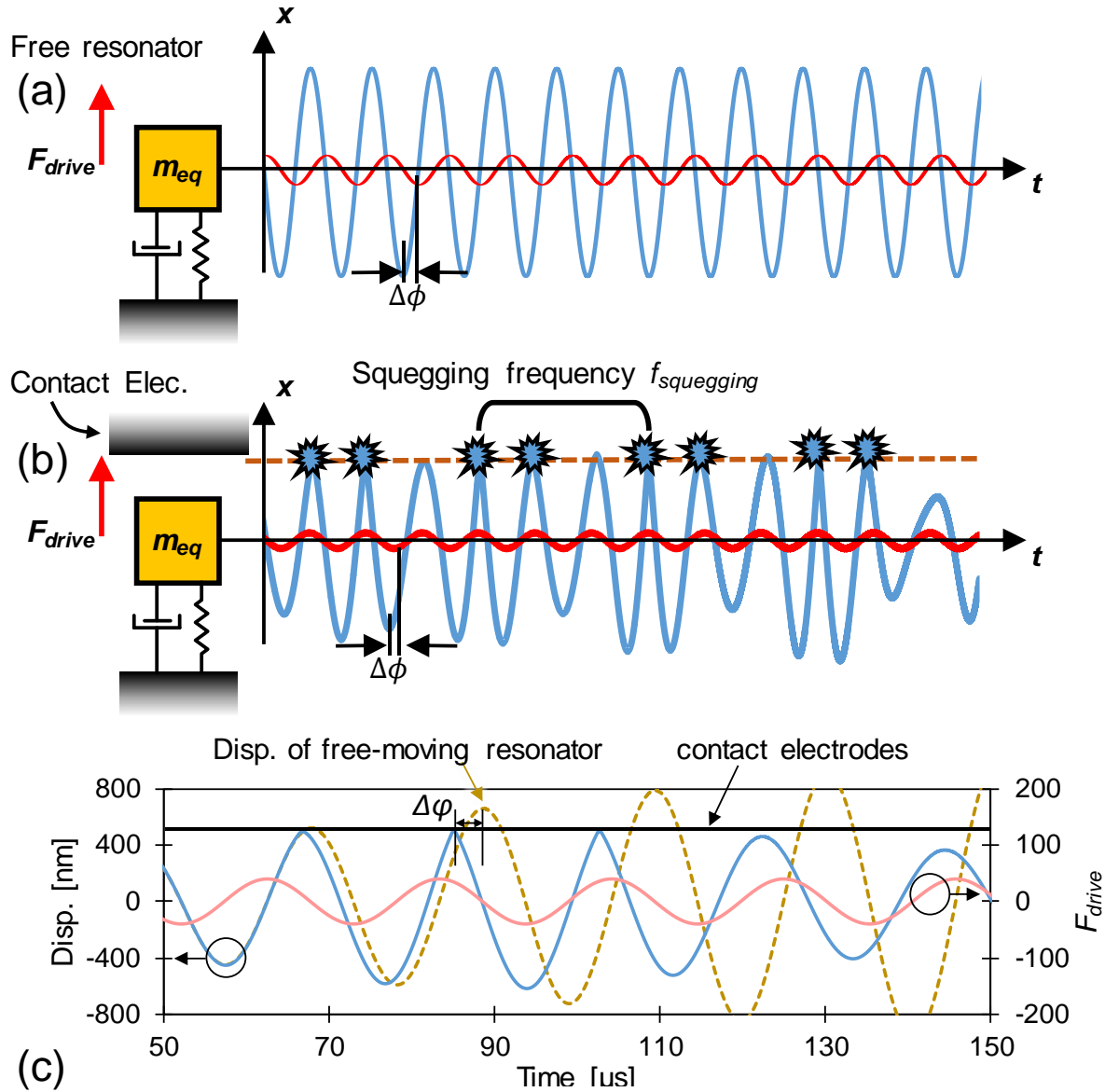inear process, especially when combined with the resonance dynamics. The outcome varies greatly depending on the exact input and impact conditions [26]. The shuttle could make periodic contacts every cycle, which produces contacts at frequency f_{drive}. Alternatively, the shuttle could make impacts less frequently, at a frequency smaller than f_{drive}, or even aperiodically, which many sources describe as chaotic behavior [27], a phenomenon called squegging. The underlying cause for squegging comes from the phase jerk introduced at contacts. Upon impact, the shuttle bounces back and advances $\Delta\varphi$ faster than the driving force. Gradually, $\Delta\varphi$ accumulates and the shuttle is completely out of sync with the driving force and the system losses energy. Then the shuttle's displacement decreases and even stops making contact. Without the disturbance of the contacts, the shuttle's displacement catches up with the drive force and starts to recover in amplitude. Therefore, the displacement dynamics fluctuates at the presence of impacts. A time-domain dynamics model is necessary to capture the impacting effect on top of the second order resonance behavior dictated by the governing equation.

As an example, the rest of this chapter discusses the transient solution of a comb-driven with center frequency f_0=123kHz, using the linear acceleration method and finite element analysis.

The comb-driven resoswitch contains four sets of symmetric folded beams, each of length 50μm and width 1.8μm, as shown in Figure 6. The shuttle, spanning 50μm, splits the comb fingers into top and bottom halves, so that the shuttle is free to resonant laterally and makes contact with the electrode that is g_{switch} away from the tip of the shuttle. The anchor of the folded beams are as close to the shuttle as possible to help alleviate residual stress in folding beams. The folded beams partially relieve residual stress and the total net stress is proportional to the distance between physical anchor and the symmetry line. The structure is symmetric about the x-axis, and the central symmetry line runs across the shuttle that acts like virtual anchor since the stress from top and bottom half of the structure are equal. As anchors stay stationary, any structure between anchors cannot expand or contract to release stress. Assuming the same residual strain across the entire structure, point A in Figure 6 needs to expand ϵL_{AO} to release the stress, but point B is at the anchor and thus cannot move. Therefore, the truss of the folded beams suffers from the residual strain L_{AO}, effectively the distance between the symmetry virtual anchor and the physical anchor.

The total stiffness of the four sets of folded beams k_t (four folded beams in parallel and each folded beam is two guided-guided beams in series) is:

$$k_t = \frac{EW^3H}{12L^3} = 6 \, N/m \qquad (2.7)$$

The shuttle has a total area of 2705 μm^2 and the truss has an area of 140 μm^2, therefore the equivalent mass m_{eq} is:

$$m_{eq} = 1.1e - 11 \, kg \qquad (2.8)$$

CHAPTER 2 RESOSWITCH DESIGN

The resonance frequency is thus

$$f_0 = \frac{1}{2\pi}\sqrt{\frac{k_t}{m_{eq}}} \tag{2.9}$$

The resoswitch has 54 fingers separating by actuation gap of $g_0 = 800nm$. If $V_p = 3V$, $v_{drive} = 0.1V$ amplitude, the driving force amplitude is:

$$F_0 = \frac{V_p v_i N \epsilon H}{g_0} = 7.4nN \tag{2.10}$$

2.3 TRANSIENT BEHAVIOR MODELLING USING THE RESTITUTION FACTOR

This section adopts the central difference method common to numerical structural analysis [28] to develop a preliminary transient response of the impacting resoswitch. Starting with the initial condition of $v(0) = 0, x(0) = 0$, the shuttle's dynamics are constructed at every incremental Δt. At any time, t, the shuttle's behavior is completely described by the corresponding state variables: displacement $x(t)$ and velocity $v(t)$. The state at the next time frame $t+\Delta t, v(t + \Delta t)$ and $x(t + \Delta t)$ are recursively derived from the current state $v(t), x(t)$ and the previous state $v(t - \Delta t)$, $x(t - \Delta t)$.

$$v(t) = \frac{1}{2\Delta t}(x(t + \Delta t) - x(t - \Delta t)) \tag{2.11}$$

$$a(t) = \frac{\frac{1}{\Delta t}(x(t + \Delta t) - x(t)) - \frac{1}{\Delta t}(x(t) - x(t - \Delta t))}{\Delta t} \tag{2.12}$$

$$= \frac{1}{\Delta t^2}(x(t + \Delta t) - 2x(t) + x(t - \Delta t))$$

Substituting equation 2.12 and 2.11 into the governing equation:

$$m_{eq}a(t) + bv(t) + kx(t) = f(t) \tag{2.13}$$

Then solve for the next state variable $x(t + \Delta t)$:

$$\frac{m_{eq}}{\Delta t^2}(x(t + \Delta t) - 2x(t) + x(t - \Delta t)) + kx(t) + \frac{b}{2\Delta t}(x(t + \Delta t) - x(t - \Delta t)) = f(t)$$
$$\left(\frac{m_{eq}}{\Delta t^2} + \frac{b}{2\Delta t}\right)x(t + \Delta t) - \left(\frac{m_{eq}}{\Delta t^2} + k\right)x(t) + \left(\frac{m_{eq}}{\Delta t^2} - \frac{b}{2\Delta t}\right)x(t - \Delta t) = f(t) \tag{2.14}$$

$$x(t + \Delta t) = \frac{\left(\left(\frac{m_{eq}}{\Delta t^2} + k\right)x(t) - \left(\frac{m_{eq}}{\Delta t^2} - \frac{b}{2\Delta t}\right)x(t - \Delta t) + f(t)\right)}{\left(\frac{m_{eq}}{\Delta t^2} + \frac{b}{2\Delta t}\right)} \tag{2.15}$$
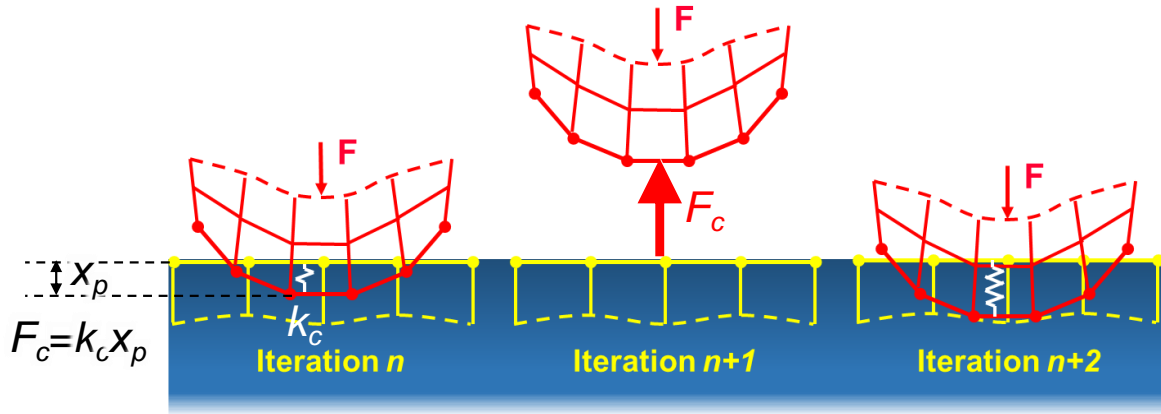
Figure 8 Finite element analysis solves contact by iterating contact stiffness k_c until penetration depth is within the preset limit.

Subsequently, equation 2.15 solves the other next state variable $v(t + \Delta t)$.

When $x(t + \Delta t) > g_{switch}$ or $x(t + \Delta t) < -g_{switch}$, $v(t + \Delta t) = -rv(t + \Delta t)$. As the displacement is large enough to make contact, the velocity scales by a restitution factor r [29].

Here equation (2.15) assumes that contact time is negligible comparing to Δt. Note that these recursive relationships are true only when Δt is small and velocity and acceleration of the shuttle are constant across the time Δt. As a result, the choice of Δt might have an effect on the solution. As long as Δt remains short enough so that the assumptions of constant velocity and acceleration over Δt is valid, the solution holds significance.

2.4 TRANSIENT BEHAVIOR MODELLING USING CONTACT STIFFNESS WITH FINITE ELEMENT ANALYSIS (FEA)

Impact events create sudden changes in the resonator's velocity, and thus cause non-convergence issue in transient analysis. Most FEA solvers model contacts with a contact stiffness based on contact compatibility shown in Figure 8, which means that the nodes within the specified contact surfaces do not travel past the target surfaces by a certain tolerance. When the contact surface meets the target surface, the solver calculates the penetration x_p from the initial starting value of contact stiffness k_c. The penetration distance x_p generates $F_{contact} = k_c x_p$ which acts on the resonator together with F_{drive} should in turn produce displacement of x_p. If the resulting x_p is larger than the penetration tolerance, the solver tries different k_c in several iterations until x_p is within the tolerance [30] [31]. However, if the contact velocity is large, the solver could need an enormous k_c to keep the penetration in check, which would result in non-convergence. This method "pure penalty" considers only contact stiffness to control penetrations. There are methods such as

CHAPTER 2 RESOSWITCH DESIGN

Augmented Lagrange that specifies the contact force a bit differently: $F_{contact} = k_c x_p + \lambda$. The λ factor provides an extra degree of freedom so that the contact force is less dependent on contact stiffness and the solution is easier to converge. The finite element transient analysis is a very slow process as the solution is serial: the solution of the next time depends on the results of the previous time. Therefore, the solver cannot divide and distribute the solving process to take advantage of the computation resources.

2.5 EFFECT OF Q ON IMPACTING RESONANCE DYNAMICS

Figure 9(a) shows the solution of the shuttle's displacement over time at steady state. $f_{drive} = f_0$ and $\Delta t < 10^{-7}$ sec. The shuttle experiences squegging, where impacts take place at a rate of $f_{squegging} = 1800Hz$. Figure 9(b) shows the frequency contents of the displacement envelope,
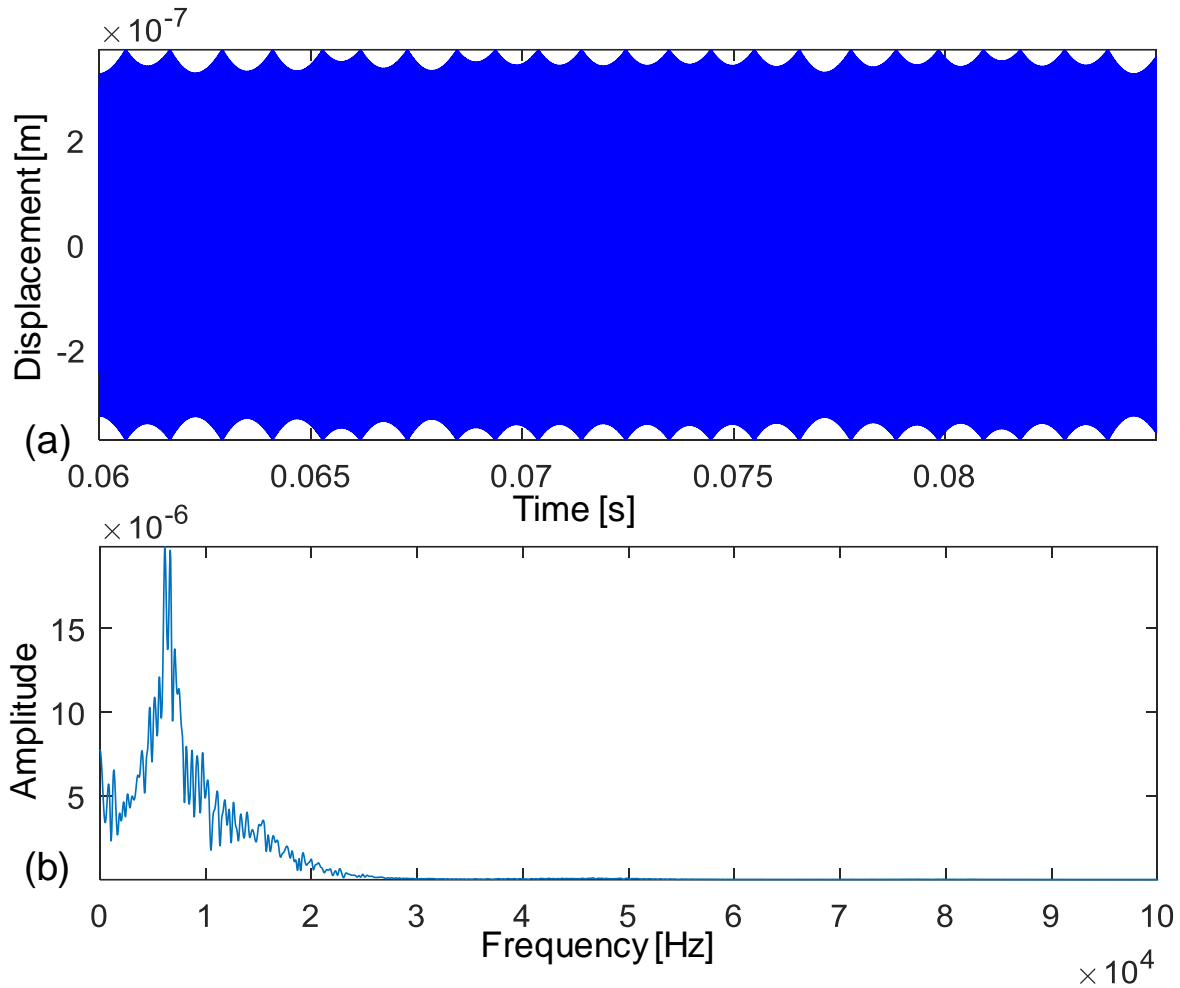
Figure 9 (a) Transient response of the resoswitch with Q of 5000; Restitution factor $= 1$; $g_{switch}/x_{max} = 1/10$. (b) FFT spectrum shows that the time domain response in (a) has a main squegging frequency at about 8000Hz.

CHAPTER 2 RESOSWITCH DESIGN

confirming significant energy content at $f_{squegging}$. The value of the squegging frequency is a function of the restitution factor and the quality factor. The higher the restitution, the more $\Delta\phi$ phase mismatch each impact creates. The response of the system is composed of the effect of initial condition and the forcing response. Impact introduces a $\Delta\phi$ phase lag, which is the initial condition of the next state's response, shifted in phase from the forced response. In the next few cycles after the impact, the response related to $\Delta\phi$ gradually damps out, restoring the system to the forced stable resonance. Intuitively, the higher the Q, the less a loss the system experiences, therefore the longer it takes to damp out the $\Delta\phi$ response. In other words, the higher the quality factor Q, the slower the system responds to changes, which means the more cycles it takes to recover the phase disturbance to make contacts again, thus lower $f_{squegging}$. Figure 13 shows the displacement solution if the resonator has Q of 3000 or 1000. The squegging frequency decreases to 1000Hz. Note that the switching gap scales with the same factor as Q to keep the ratio of d_{switch} and $x_{max} = Q\frac{F_0}{k}$ constant. For example, as Q increases from 5000 to 8000, by a factor of 8/5, d_{switch} scales by the same factor of 8/5. Figure 10 plots $f_{squegging}$ vs. Q, keeping everything else including the ratio of d_{switch} and x_{max} the same.

2.6 EFFECT OF THE RESTITUTION FACTOR ON IMPACTING RESONANCE DYNAMICS

The restitution factor also have an effect on squegging frequency. Q dictates the number of cycles required while the restitution factor predicts how much phase lag each impact creates. The more negative the restitution factor the more phase jerks at each impact, and therefore it takes more cycles to recover. The impact obeys the conservation of the momentum:
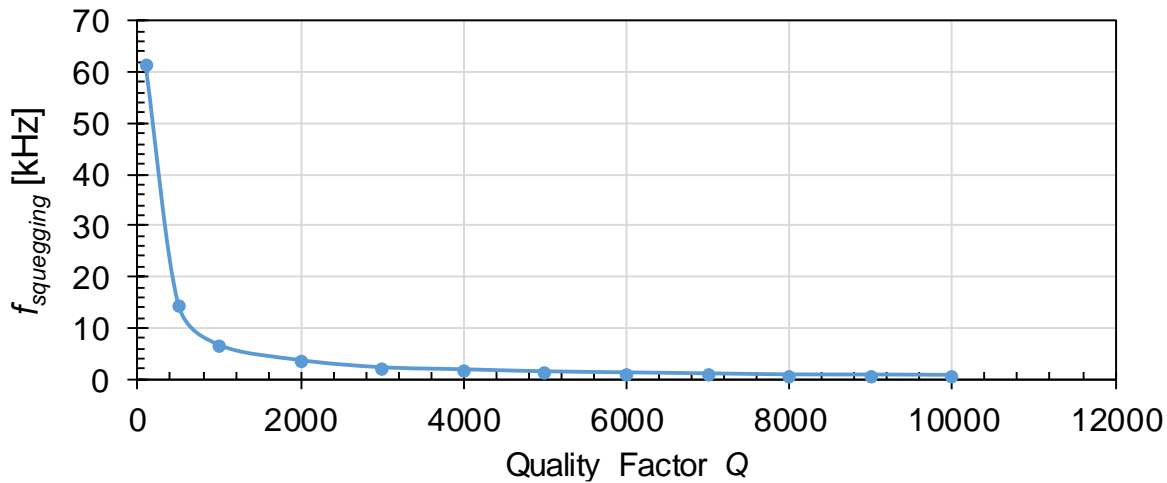

Figure 10 Squegging frequency decrease with the increase of Q, all else stay the same.

CHAPTER 2 RESOSWITCH DESIGN

$$m_{eq}v(t) + m_{anchor}v_{anchor}(t) = m_{eq}v(t + \Delta t) + m_{anchor}v_{anchor}(t + \Delta t) \qquad (2.16)$$

where $v(t)$ and $v(t + \Delta t)$ are the velocities of the shuttle before and after the impact. For perfectly elastic collisions, kinetic energy also conserves before and after the impact:

$$\frac{1}{2}m_{eq}v(t)^2 + \frac{1}{2}m_{anchor}v_{anchor}(t)^2$$
$$= \frac{1}{2}m_{eq}v(t + \Delta t)^2 + \frac{1}{2}m_{anchor}v_{anchor}(t + \Delta t)^2 \qquad (2.17)$$

Solving for $v(t + \Delta t)$ as a function of $v(t)$:

$$v(t + \Delta t) = \frac{v(t)(m_{eq} - m_{anchor}) + 2m_{anchor}v_{anchor}(t)}{m_{eq} + m_{anchor}} \qquad (2.18)$$

In the case of resoswitch, $m_{eq} \ll m_{anchor}$ and $v_{anchor} = 0$. Therefore:
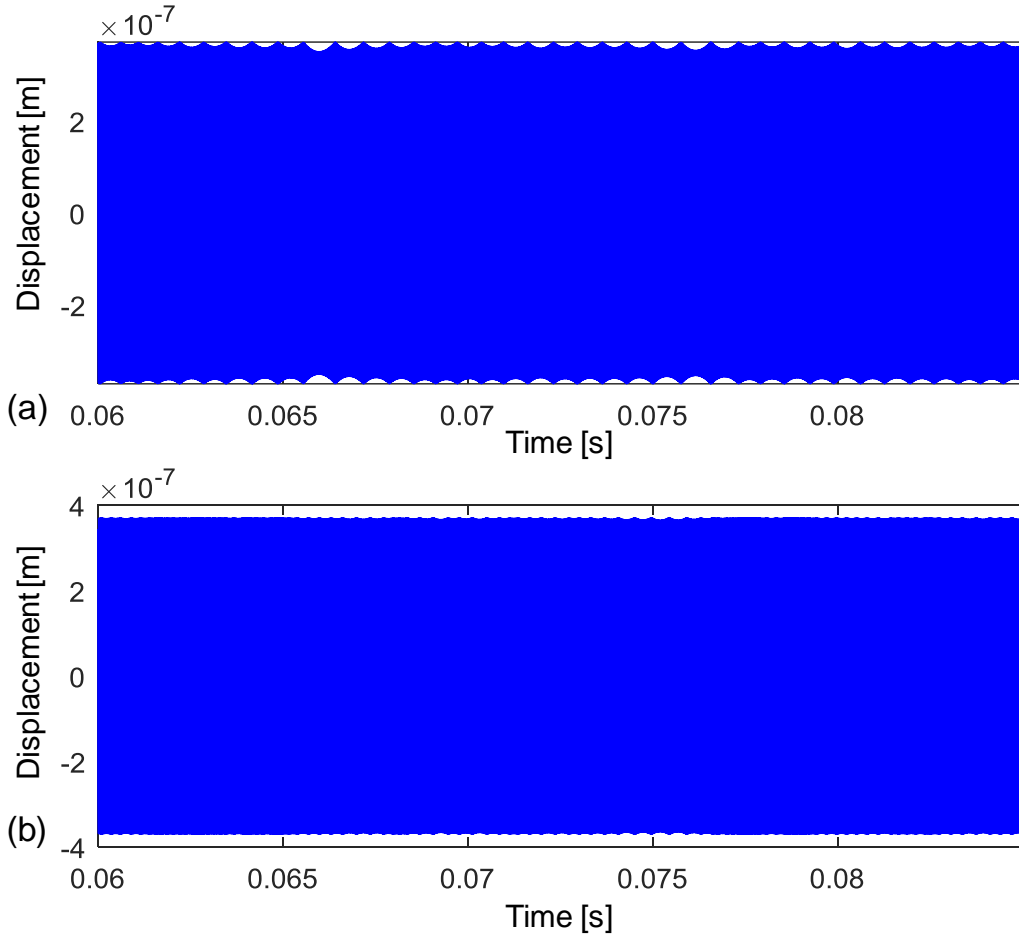

Figure 11 (a) Transient response of the resoswitch with Q of 5000; Restitution factor = 0.9; g_{switch}/x_{max} = 1/10. (b) Transient response of the resoswitch with Q of 5000; Restitution factor = 0.8; g_{switch}/x_{max} = 1/10.

$$v(t + \Delta t) \approx -\frac{v(t)m_{anchor}}{m_{eq} + m_{anchor}} = -v(t) \qquad (2.19)$$

The restitution factor is -1 for perfectly elastic collision. Figure 11 shows the displacement transient responses with a restitution factor of 0.9 and 0.8, where the impact creates little to none disturbance to the resonance. In most applications, the stability of the frequency characteristic component, for example, the resoswitch, dictates the reliability and the resolution of the entire system [32]. In order for the resoswitch to produce a stable switching frequency, the effect of the resonance disturbing impacts should be either tightly controlled or minimized.

2.7 SOFT CONTACTS

Minimizing the perturbation of impact on the resonance so that the resoswitch makes a gentle impact every cycle can help guarantee the resoswitch's stability that then becomes the stability of the natural resonance frequency of the resoswitch determined by the material properties and the geometries. In other words, "soft" contact minimizes the restitution factor.

The restitution factor is a reflection of impact stiffness. For a resonator with a natural frequency of about 100kHz, the contact time is negligible, thus the contact force is responsible for the change in the momentum of the resonator.
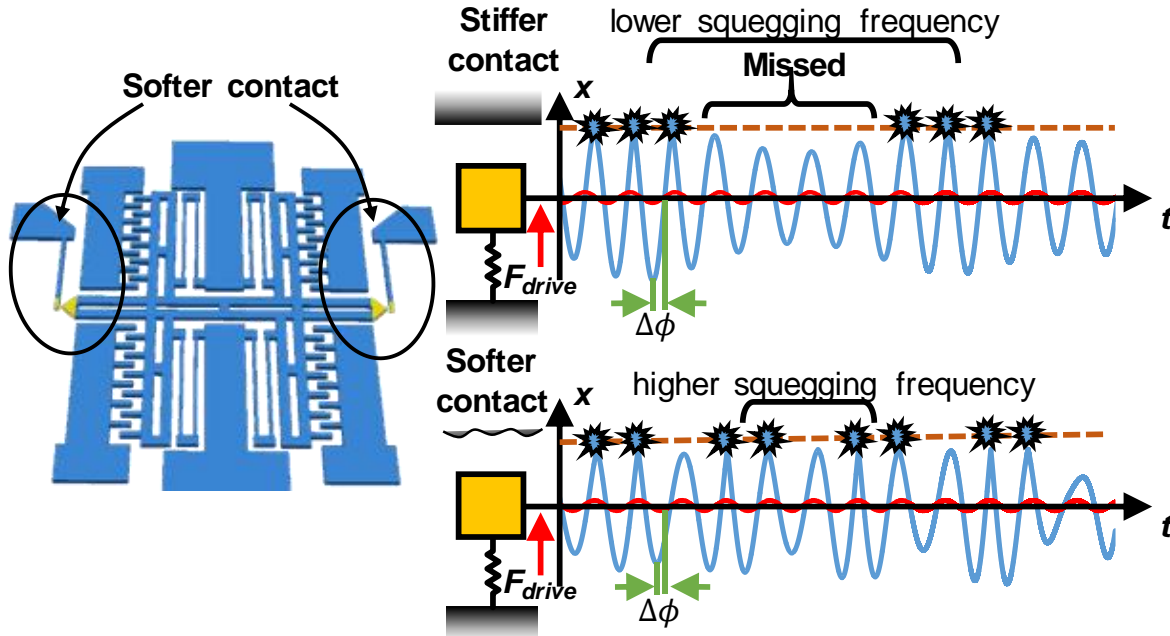

Figure 12: Cantilever electrodes provide soft contacts to the resoswitch. The impact generates less phase lag at each contact, and thus it takes less cycles to restore the regular resonance. The squegging frequency is higher comparing to resoswitch with stiff contact electrodes.

$$F_c t_c = m_{eq} v(1 + r) \tag{2.20}$$

where t_c is the contact time. If r increases, F_c is also higher. With limited penetration depth, the contact stiffness grows proportionally. The contact surfaces and impact materials determine how "hard" the contact is and therefore is partially responsible for contact stiffness. The other half that can change the stiffness is the contact velocity. The restitution factor encompasses some of the impact factors: impact surface material, surface property etc. into one behavioral coefficient, making numerical solutions easier. However, some factors are missing, like impact velocity. The restitution factor only specifies a constant ratio between the velocities before and after impact. In reality, the restitution could be a function of impact velocity. FEM analyses avoid setting a constant restitution factor; rather, it calculates F_c as a fitting factor that satisfies the resonator's dynamics without penetrating into the contact electrode.

Soft contact requires small contact stiffness, but the condition of the contact surface is usually hard to predict and characterize. The contact material needs to be very conductive and physically hard, i.e. high Young's Modulus at the same time. As impact heats up the contact surfaces, the contact material forms native oxide, so it is desirable to have a contact material whose native oxide is also conductive or inert material that does not form oxide. The material properties and native oxide conductivity limit the choice of material to a few noble metals such as Au, Mo, Ru and a few alloys and compound such as TiN. With the additional high Young's Modulus criteria, Ru is most promising. Au has ideal nobility and has perfect conductivity, but it is notoriously soft, therefore it brings bad contact reliability. In conclusion, the limited choice of contact material poses difficulty on fabrication. To make matters worse, the area of the contact surface change due to deformation; the contact surface asperities flatten after thousands of contacts and some amount of mass transfers between the two contacts. In conclusion, the contact material and contact surface contributor to contact stiffness is a very complicated factor and is extremely difficult to control and predict [33].

Therefore, to soften the contact, this section focuses on the target contact-electrode design, introducing "soft contact electrode". The contact electrode is no longer an anchored physical island of material, rather, it moves upon contact. Figure 14 shows a pair of cantilevers as the contact electrodes. The idea is that instead of posing a "hard" displacement limit on the resoswitch with tiny penetration, the cantilever provides a velocity buffer, allowing the impacting velocity of the shuttle decrease. In other words, soft contact electrodes introduce less phase jerk $\Delta\varphi$ upon impacts.

CHAPTER 2 RESOSWITCH DESIGN

Figure 14 shows the FEM transient analysis results with soft cantilever contact electrodes. The two orange and blue curves represent the displacements of the resoswitch and the electrode respectively. The grey colored curve indicates the impact force at each contact. The resoswitch pushes the electrodes at every impact, transferring energy to the electrodes. The cantilever electrodes are themselves another mass-spring-damper second-order systems, except that their natural resonance frequencies are much higher, so that the electrodes act like springs (or electrical equivalence of capacitors) to the resoswitch. The four figures in Figure 14 are the results of impact dynamics under different Q factors. With higher Q, it takes longer for the energy injected into electrodes to dissipate, therefore the electrodes appear to follow the resoswitch for larger displacements and ring for more cycles. In comparison, Figure 13 also shows the transient response of solving the recursive time-domain model. The solution agrees with FEM simulation that the higher the quality factor, the more squegging the resoswitch experiences.
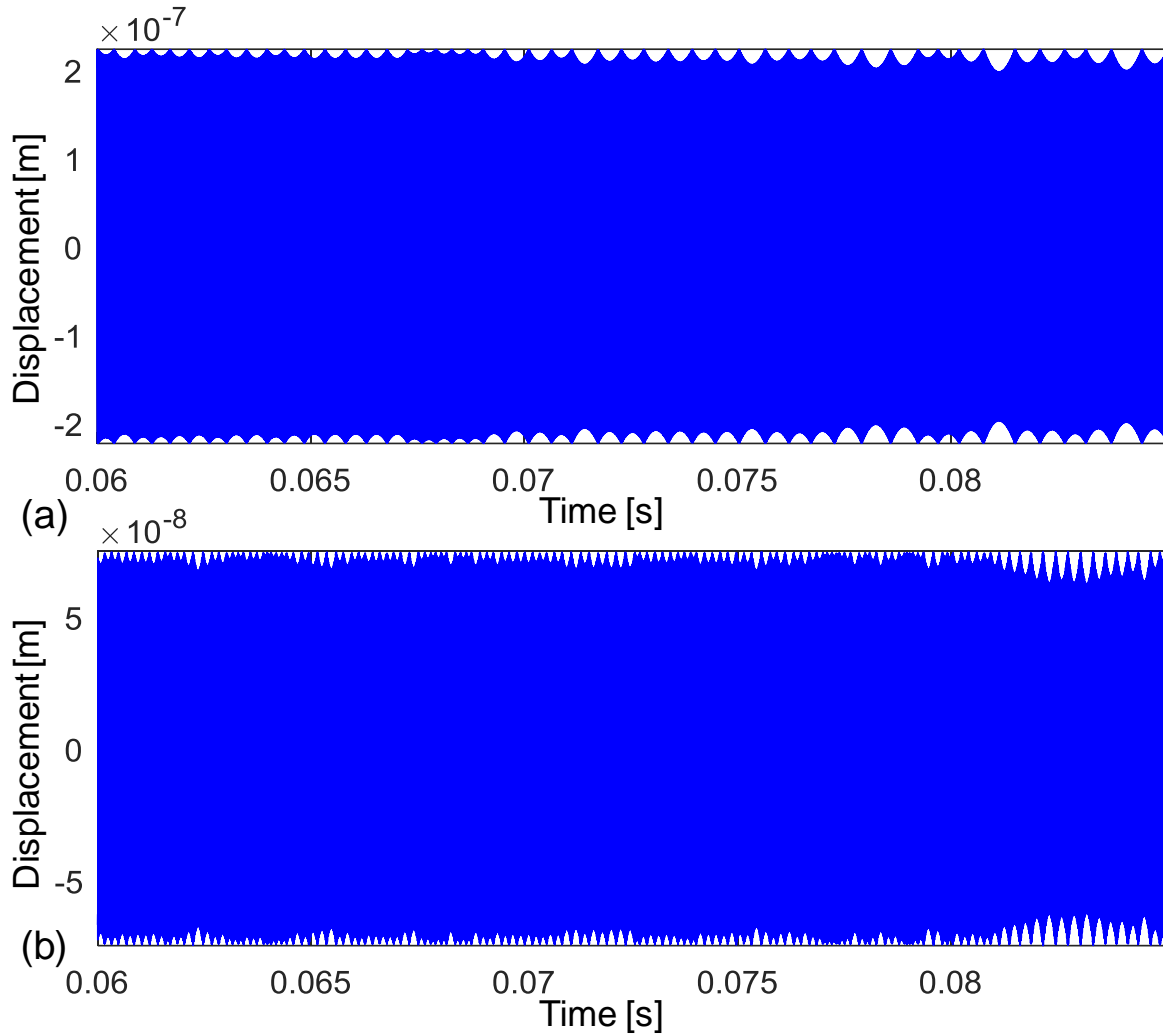

Figure 13 (a) Transient response of the resoswitch with Q of 1000; Restitution factor = 1; g_{switch}/x_{max} = 1/10. (b) Transient response of the resoswitch with Q of 3000; Restitution factor = 1; g_{switch}/x_{max} = 1/10.

CHAPTER 2 RESOSWITCH DESIGN

The stiffness of the cantilever has similar effect on the resoswitch dynamics as the restitution factor. In the previous section, the numerical transient solution predicts that the squegging frequency $f_{squegging}$ increases with decreasing restitution factor. Softer contact electrodes have higher $f_{squegging}$, and make more numbers of contact, but at the same time, experience smaller contact force, as shown in Figure 15. Here, the dynamics indicates that there is a trade-off between the stability of the resoswitch frequency response and contact resistance. If the contact electrodes soften the impact discontinuity, thus the system has better frequency stability, then the contact resistance increases.

Duffing curves often represent the nonlinear behavior of the system. System nonlinearities result in multiple solutions for a single frequency point. Depending on the previous state, or the initial condition of the current state, the resoswitch assumes one of the solutions. Therefore, sweeping the input frequency upwards from low to high has different result than sweeping from high to low. Free moving resonators also suffer from nonlinearity in terms of spring softening or hardening when the displacement is large. Resoswitch contacts add one more nonlinear component to this
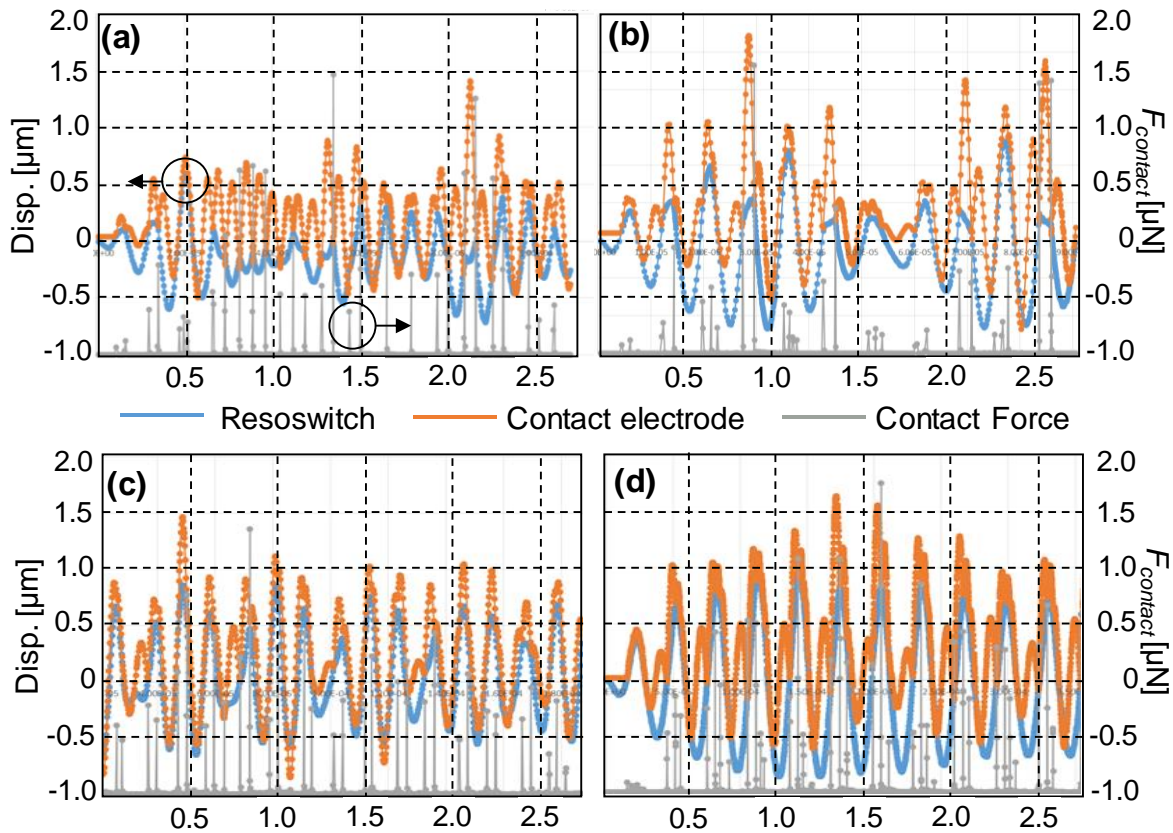

Figure 14 FEM transient analysis results for a resoswitch with different Q values, all other parameters stay the same. The orange curve stands for the displacement of the electrode and the blue curve stands for the displacement of the shuttle. The grey curve represents contact force. Here the cantilever is 1/1000 of the resonator. a): $Q=100$, b) $Q=500$, c) $Q=1000$, d) $Q=5000$.

spring effect. Figure 16 shows the measured transmission magnitude sweeping up from low to high frequencies overlaying with results of down sweeping, from high to low frequencies. Hard-impact contact electrodes have the most distorted duffing curve. Clamp-clamp (cc) beam contact electrodes have higher stiffness than the cantilever contacts [34]. Therefore, the cc beam contact resoswitches suffer from more nonlinearity in the system. The measurement of a pure comb drive without contact electrodes serves as a reference to rule out the spring nonlinearity due to large displacement.
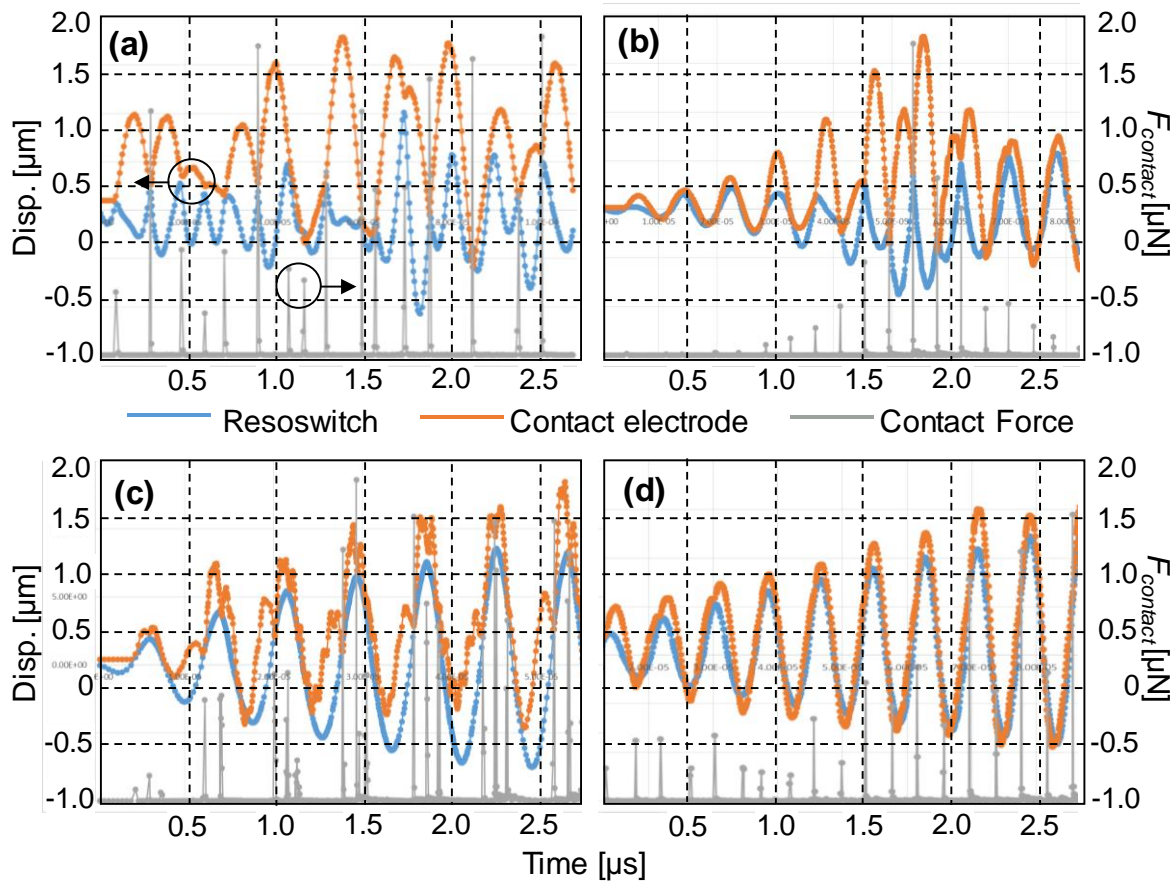
Figure 15 FEM transient analysis results for a resoswitch with different contact cantilever-electrode stiffness k_{canti}, all other parameters stay the same. a) $k_{canti} = k/500$ where k is the stiffness at the shuttle of the resonator. (b) $k_{canti} = k/300$ (c) $k_{canti} = k/200$ (d) $k_{canti} = k/100$

(a) Cantilever contact (dotted line is upsweep plot)

(b) CCBeam Contact (dotted line is upsweep plot)
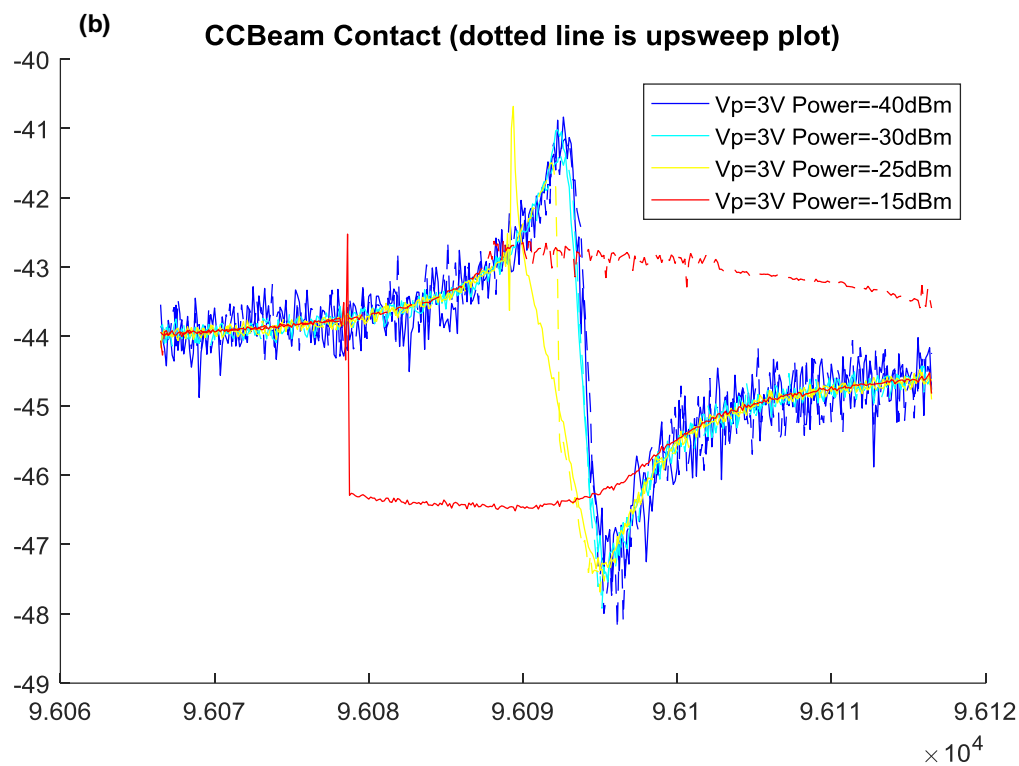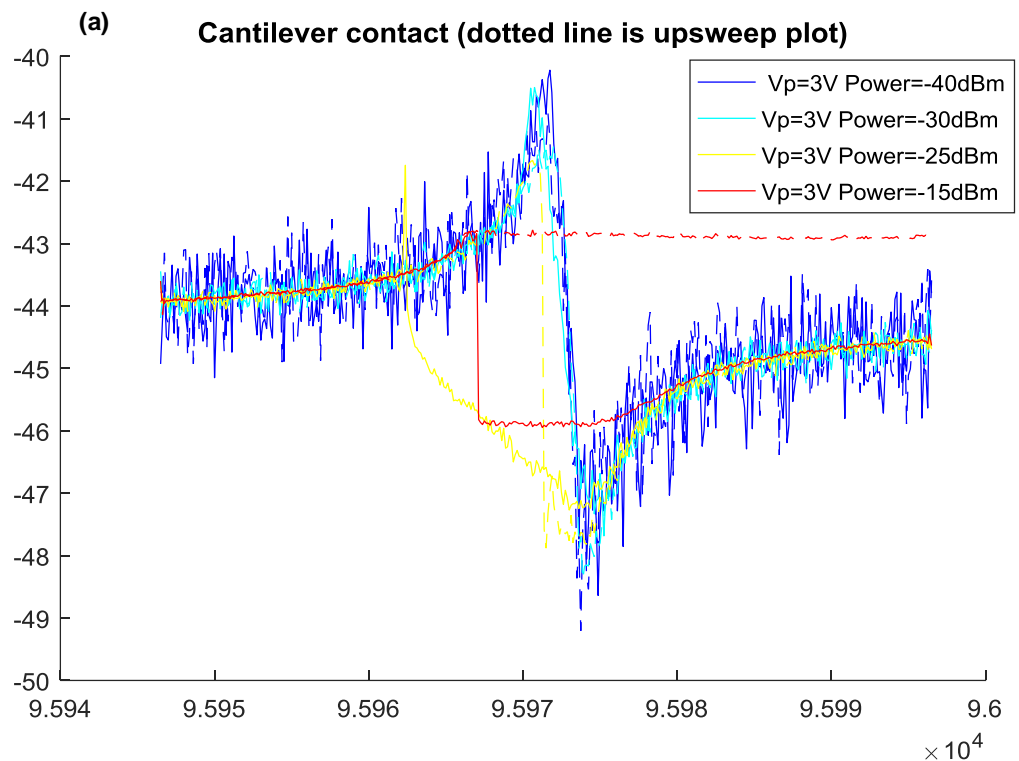
Figure 16 Frequency transmission magnitude of resoswitches with different contact electrodes. (a) Cantilever contact electrodes. (b) Clamp-clamp beam contact electrodes. (c) Comb drive resonators with no contact electrodes. (d) Anchored hard contact electrodes.

2.8 EFFECT OF THE G_{SWITCH}/X_{MAX} RATIO ON IMPACTING RESONANCE DYNAMICS

Another parameter affecting $f_{squegging}$ is the switch gap g_{switch}, defined as the ratio of the physical gap spacing g_{switch} and the maximum displacement the resonator can achieve if there were no contact electrode x_{max}. With everything else staying the same, smaller g_{switch}/x_{max} gives larger $f_{squegging}$. As the g_{switch}/x_{max} ratio increases, the resoswitch has more room to move and the impact velocity increases. Therefore, there is more disturbance to the resonance and thus larger $f_{sq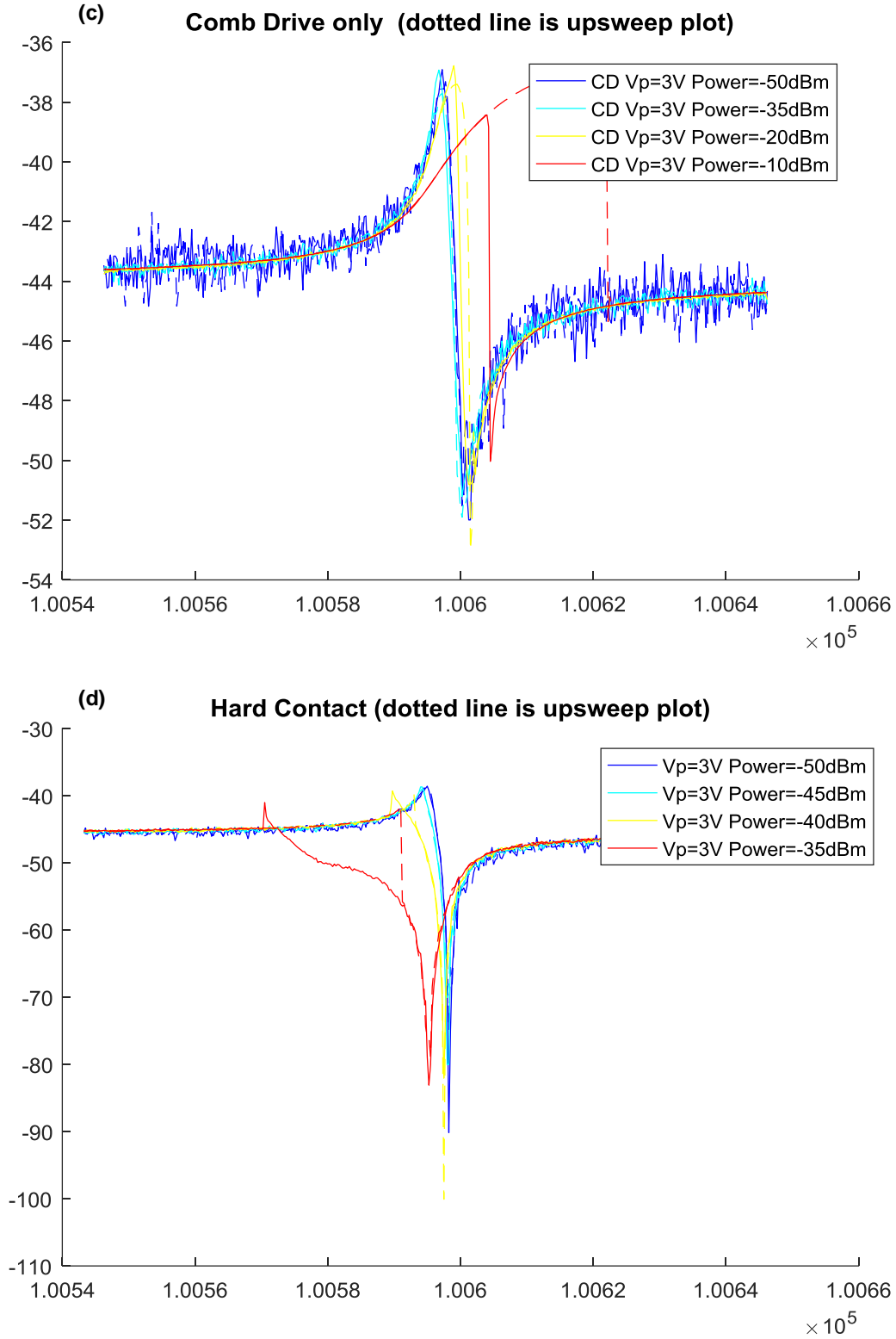uegging}$, which requires smaller Δt in the transient simulation. The numerical stability of the central difference method depends on the choice of Δt, thus limits the efficiency of the simulation. The Newmark-β method approximates the next state variables as:

$$x(t + \Delta t) \approx x(t) + \Delta t v(t) + \Delta t^2 \big((1 - 0.5\beta_2)a(t) + \beta_2 a(t + \Delta t)\big) \tag{2.21}$$

$$v(t + \Delta t) = v(t) + \Delta t\big((1 - \beta_1)a(t) + \beta_1 a(t + \Delta t)\big) \tag{2.22}$$

Substituting $\delta f(t) = f(t + \Delta t) - f(t)$, $\delta x(t) = x(t + \Delta t) - x(t)$ $\delta v(t) = v(t + \Delta t) - v(t)$ and $\delta a(t) = a(t + \Delta t) - a(t)$:

$$\delta a(t) = \frac{1}{\beta \Delta t^2}\delta x(t) - \frac{1}{\beta \Delta t}v(t) - \frac{1}{2\beta}a(t) \tag{2.23}$$

$$\delta v(t) = \frac{\beta_1}{\beta_2 \Delta t}\delta x(t) - \frac{\beta_1}{\beta_2}v(t) + \Delta t\left(1 - \frac{\beta_1}{2\beta_2}\right)a(t) \tag{2.24}$$

With the governing equation: $m_{eq}\delta a(t) + b\delta v(t) + k\delta x(t) = \delta f(t)$

$$\delta x(t) = \frac{\delta f(t) + \left(\dfrac{m_{eq}}{\beta_2 \Delta t} + \dfrac{b\beta_1}{\beta_2}\right)v(t) + \left(\dfrac{m_{eq}}{2\beta_2} - b\Delta t\left(1 - \dfrac{\beta_1}{2\beta_2}\right)\right)a(t)}{\left(\dfrac{m_{eq}}{\beta_2 \Delta t^2} + k + \dfrac{b\beta_1}{\beta_2 \Delta t}\right)} \tag{2.25}$$

Therefore,

$$x(t + \Delta t)$$

$$= x(t) + \frac{f(t + \Delta t) - f(t) + \left(\dfrac{m_{eq}}{\beta_2 \Delta t} + \dfrac{b\beta_1}{\beta_2}\right)v(t) + \left(\dfrac{m_{eq}}{2\beta_2} - b\Delta t\left(1 - \dfrac{\beta_1}{2\beta_2}\right)\right)a(t)}{\left(\dfrac{m_{eq}}{\beta_2 \Delta t^2} + k + \dfrac{b\beta_1}{\beta_2 \Delta t}\right)} \tag{2.26}$$

$$v(t + \Delta t) = v(t) + \frac{\beta_1}{\beta_2 \Delta t}\delta x(t) - \frac{\beta_1}{\beta_2}v(t) + \Delta t\left(1 - \frac{\beta_1}{2\beta_2}\right)a(t) \tag{2.27}$$

Here β_1 and β_2 are scaling factors that help with numerical stability of the transient solution. In particular, when $\beta_1 = 0.5, \beta_2 = 0$, the Newmark-β method reduces to central difference method.

CHAPTER 2 RESOSWITCH DESIGN

In the case of resoswitch, $\beta_1 = 0.5, \beta_2 = 0.09$ provides the best results in terms of numerical stability. Using the Newmark-β method, Figure 17 shows the response of a resoswitch with g_{switch}/x_{max} of 1/20 versus 1/10.

For a free-moving resonator, the highest velocity happens when the resonator is at equilibrium, which is displacement = 0. Therefore, to obtain higher contact velocity, the contact electrode needs to be close to displacement = 0 position. However, on the other hand, the velocity of the resonator with no mechanical stops is proportional to the displacement the resonator travels. If the contact electrode severely limits the resonator's displacement, then the resonator will not get a change ramp up in velocity. Thus, the impact velocity is not a monotonic function of switching gap. Rather, there is a maximum at about a ratio of 0.33 ($g_{switch}/x_{max} = 0.33$), shown in Figure 18.

The contact resistance scales inversely with impact velocity. For contact materials such as polysilicon that forms native oxide, the contact velocity has to be large to break through the surface native oxide and make electrical contacts. However, for metals, charge transfers can happen at a
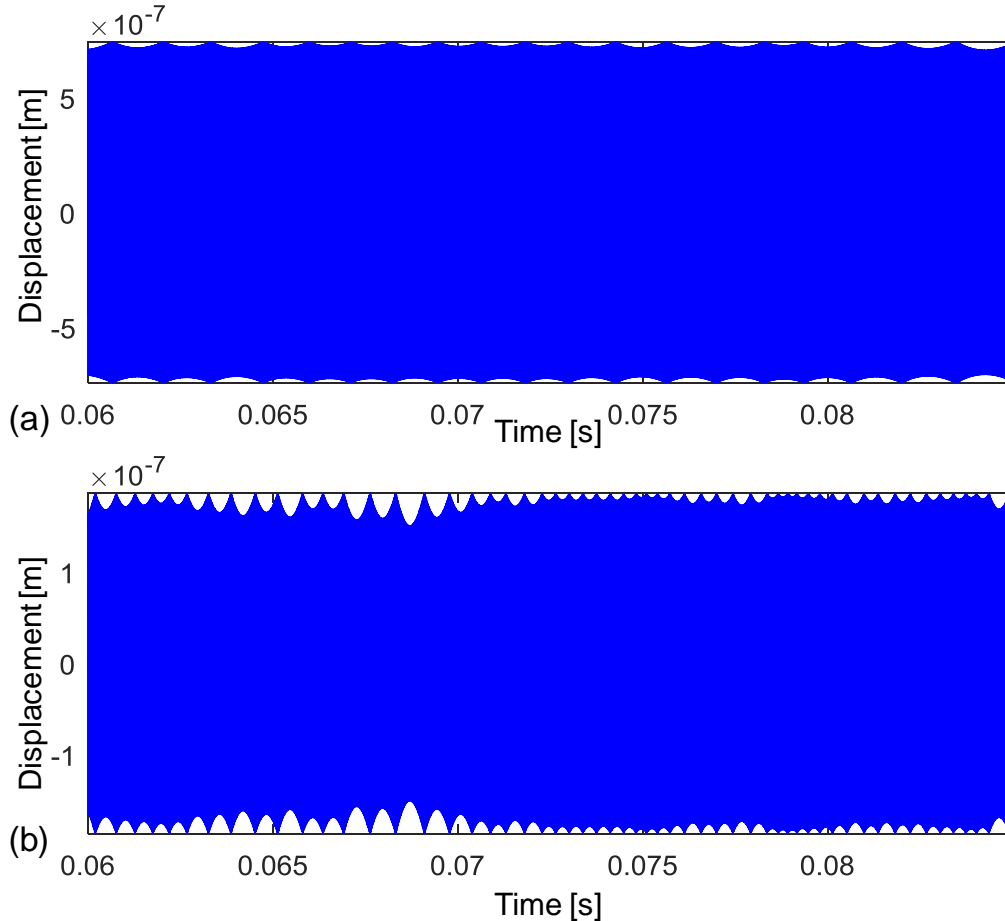
Figure 17: (a) Transient response of the resoswitch with Q of 5000; Restitution factor = 1; g_{switch}/x_{max} = 1/20. (b) Transient response of the resoswitch with Q of 5000; Restitution factor = 1; g_{switch}/x_{max} = 1/5.
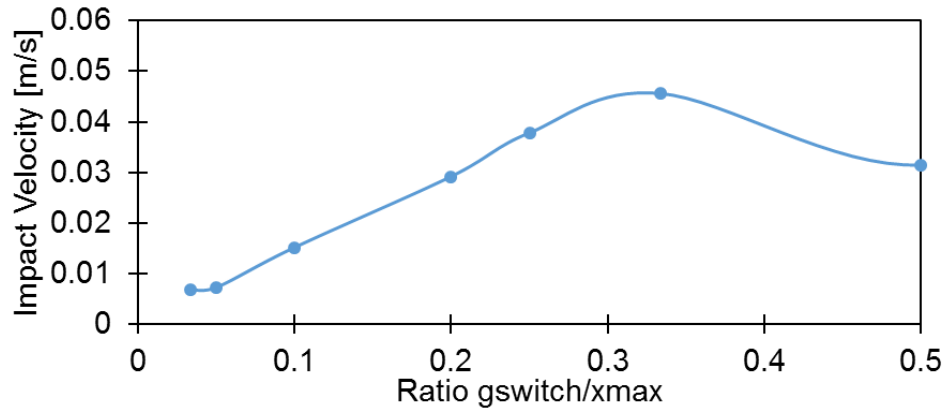
Figure 18 Impact velocity vs. the switch gap-spacing ratio. The resonator has larger velocity when it is closer to equilibrium position, but the further the contact electrode is, the more the resonator's velocity can grow. As a result, the dependency of impact velocity on the switch spacing is not monotonic.

relatively lower contact velocity and therefore might provide better reliability. Later chapters describe in details the fabrication and experimental data on resoswitch and its application as receivers and RF powered wireless clocks.

Chapter 3   RESOSWITCH PROCESS DESIGN

Pursuant to fabricating resoswitches with low contact resistance, the efforts of resoswitch design start with the electroplated gold process. Gold material has an electrical resistivity of 2.44×10^{-8} ohm*m, lower than most metals commonly available in microfabrication processes. More importantly, its inert nature prevents the switch contacts from oxidizing as charges pass through and heat up the contacts. As a result, gold is widely used as switch contact material [35] [36] in both micromechanical switches and macroscopic switches.

3.1   GOLD-ELECTROPLATED COMB-DRIVE RESOSWITCHES

Comb-driven resonator is the first candidate for resoswitch due to its well-studied actuation mechanism and its compatibility with a relatively simple one-mask process. As described in Chapter 2, the motional resistance R_x of the resonator depends inversely on the thickness of the structure, thus the resonators are from a one-mask electroplating gold process. Figure 19 depicts the process flow.

In the development of the gold comb-driven resoswitch process that Figure 19 summarizes, there are several main challenges that are essential to achieving small gaps between comb fingers and low stress structure: electroplating mold, seed layer and the electroplating recipe.

3.1.1   OXIDE MOLD

While the traditional electroplating process uses developed photoresist as the mold for the electroplating process, this process adopts Plasma Enhanced Chemical Vapor Deposition (PECVD) SiO_2 as mold material. To electroplate microstructures of 2µm, the mold structure needs to be 2.5µm to 3µm thick. The smallest features that photoresists of thickness of 3µm can resolve are larger than 1µm. However, etch profile of 3µm thick SiO_2 can achieve resolutions of 500nm. In this case, depositing SiO_2 on top of the metal seed layer limits the

CHAPTER 3 RESOSWITCH PROCESS DESIGN

thermal budget of the SiO₂ deposition. Therefore, PECVD oxide at low temperature is the material of choice for electroplating mold.

3.1.2 Seed Layer.

Gold electroplating operates commonly on gold seed layer [37] that is the most obvious choice of seed layer. However, the seed layer removal step in Figure 19(e) includes a short dip in wet etchant. Using gold as a seed layer requires etching in gold etching solution that also erodes the electroplated structures. Gold is resistant to the etchant of Cr (Cr-7) and Ni (Transene Ni etchant), which is confirmed by the following procedure. Evaporated gold film of 10nm has sheet resistance of 3.3 ohm/sq. After soaking in Cr-7 and Ni etchant for 5mins, the sheet resistance measures 3.2 ohm/sq and 3.4 ohm/sq respectively. There are no change in gold film observed. Therefore, several attempts to electroplate on seed layers of Cr and Ni that are also
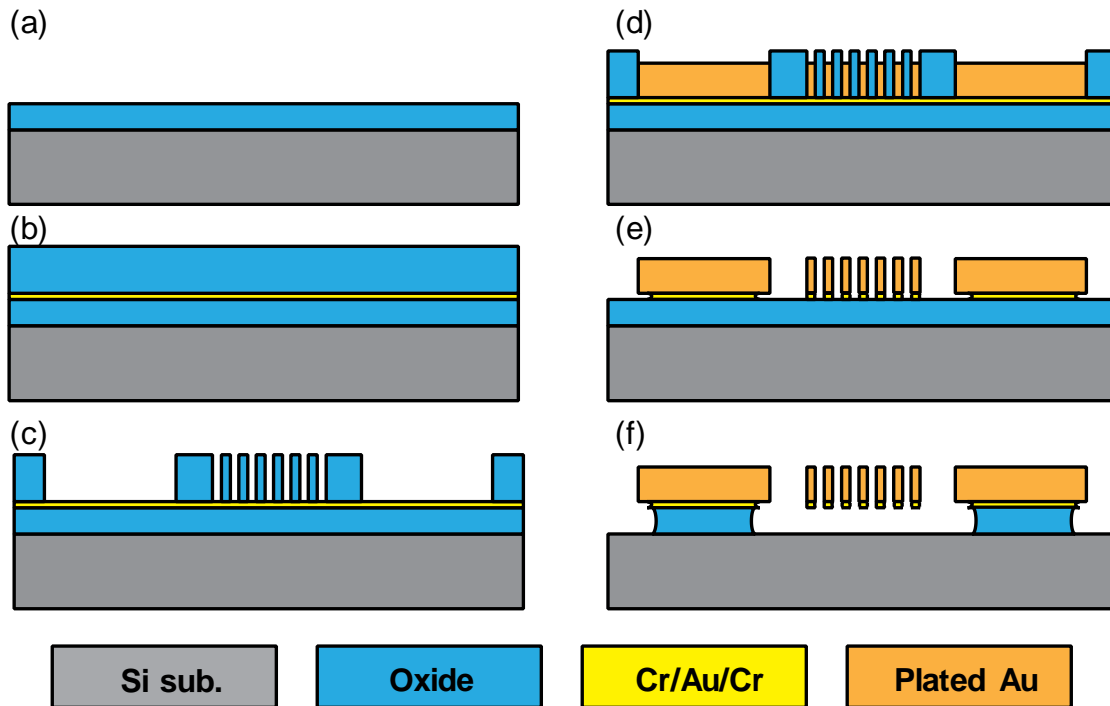
Figure 19: Process flow of electroplated gold resoswitch. (a): Deposit 2µm of sacrificial oxide on silicon substrate. (b): Evaporating Cr/Au/Cr seed layer subsequently, followed by 3µm of oxide mold for later electroplating. (c) Etch oxide mold stopping on seed layer Cr surface. (d): A quick dip in Cr etchant removes the top Cr from the seed layer and expose the underlying Au. Then electroplate on Au seed layer. (e): Remove oxide mold in HF and a timed wet etch removes the seed layer in the field and expose the sacrificial oxide. (f): Timed etch in HF releases the folded structures while oxide remains under large anchor pads.

resistant to Hydrofluoric acid (HF), the solution to release the device in Figure 19(f). Both Cr and Ni form native metal oxides that needs remove before electroplating.
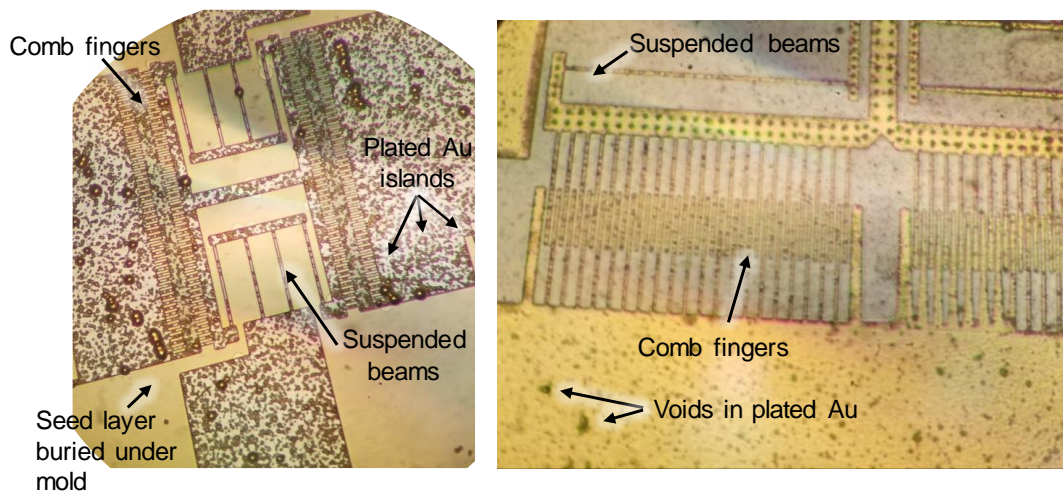
Figure 20: (Left) Electroplating on Ni seed layer. Au islands are visible, but no uniform layer formed. The plating solution erodes Ni, leaving holes in seed layer, increasing electrical resistance to plating sites and affecting plating quality. (Right) Electroplating on Cr seed layer. The Au layer has occasional voids in the film.
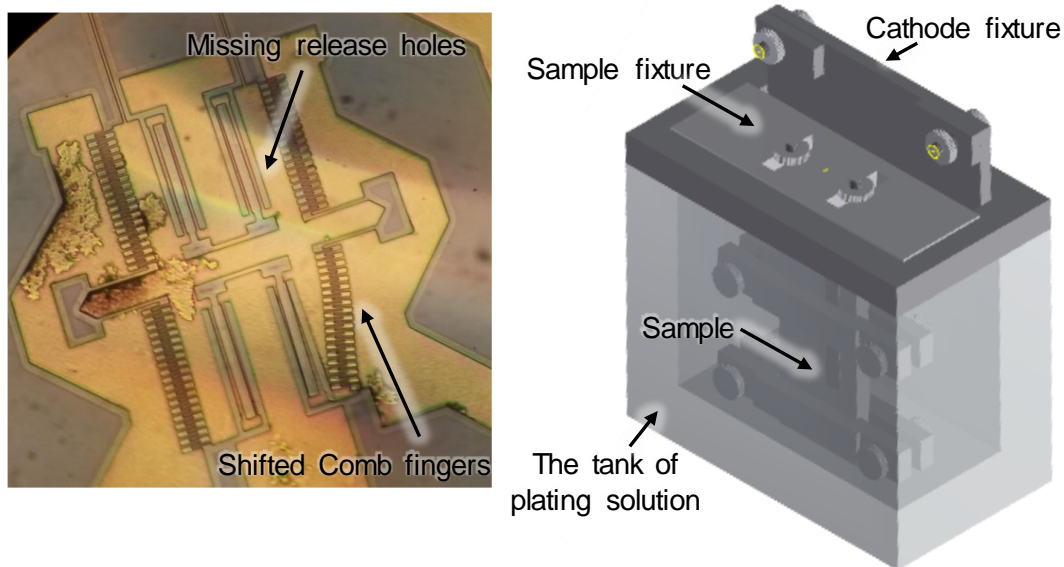
Figure 21: (Left) Successful electroplating on Au seed layer. However, the etching of Cr to expose Au seed layer right before electroplating needs proper timing. Overetch can cause the islands of molds, such as between comb fingers or release holes to shift around or drift away. (Right) The design schematic of the redesigned electroplating setup. The sample fixture and cathode fixture make sure the sample is parallel to cathode. At the same time, the sample fixture slides on the tank lid, adjusting the distance between the sample and the cathode.

CHAPTER 3 RESOSWITCH PROCESS DESIGN

In the case of Cr, after immersing in Hydrochloric acid (HCl) for 10secs to remove the surface native Cr oxide, the sample electroplates under various conditions. Figure 20 shows the microscopic images before and after electroplating. Some islands of gold appear on electroplated area, but at places where no gold is plated, Ni seed layer seems have eroded away by the electroplating solution. The plated gold is powder-like and does not form a continuous film.

For Ni seed layer, Figure 20 shows the microscope image after electroplating. Current density of about 2mA/cm^2 results in the best electroplating quality. The film is not uniform as there are patches of darker color in some areas. However, the adhesion of plated gold to the seed layer Ni is weak. Rinsing in water easily peel off the plated structure, leaving just the seed layer behind.

Unable to use other seed layers, gold ends up to be the most reliable electroplating seed layer of choice. Therefore, the seed layer needs to be very thin so that the removal process after electroplating does not significantly erode the electroplated structures. The etch rate of electroplated gold in gold etchant (Transene TFA) is about 2nm/sec. However, the electroplated gold is more porous and thus etches faster in the etchant, 8nm/sec. To minimize overetching while at the same time minimize resistance of the seed layer to achieve good electroplating quality, 14nm of the gold seed layer is evaporated on top of 5nm of Cr adhesion layer.

The seed layer in this process also serves as an etch stop for the subsequent etching of the PECVD oxide mold. Therefore, another 7nm of Cr covers the Au/Cr seed layer to protect the Au from the oxide etching.

3.1.2.1 OXIDE MOLD DEPOSITION

PECVD oxide covers the top Cr protection layer that easily oxidizes. Standard PECVD deposition happens at 350ºC in SiH$_4$/N$_2$O/Ar chemistry. However, seed layer bubbles where there is large metal area. Even in the small metal area, the oxidation of Cr during deposition weakens the adhesion of the oxide to seed layer. After etching the oxide to reach the underlying seed layer, during the short dip in Cr-7 etchant that exposes the Au underneath for electroplating, the oxide mold shifts around, compromising the structure as shown in Figure 21. To alleviate oxidation, PECVD deposition temperature reduces to 300ºC. Deposition of PECVD oxide at temperatures lower than 300ºC produces powder like film with more pinholes and worse etch profile shown in Figure 24.
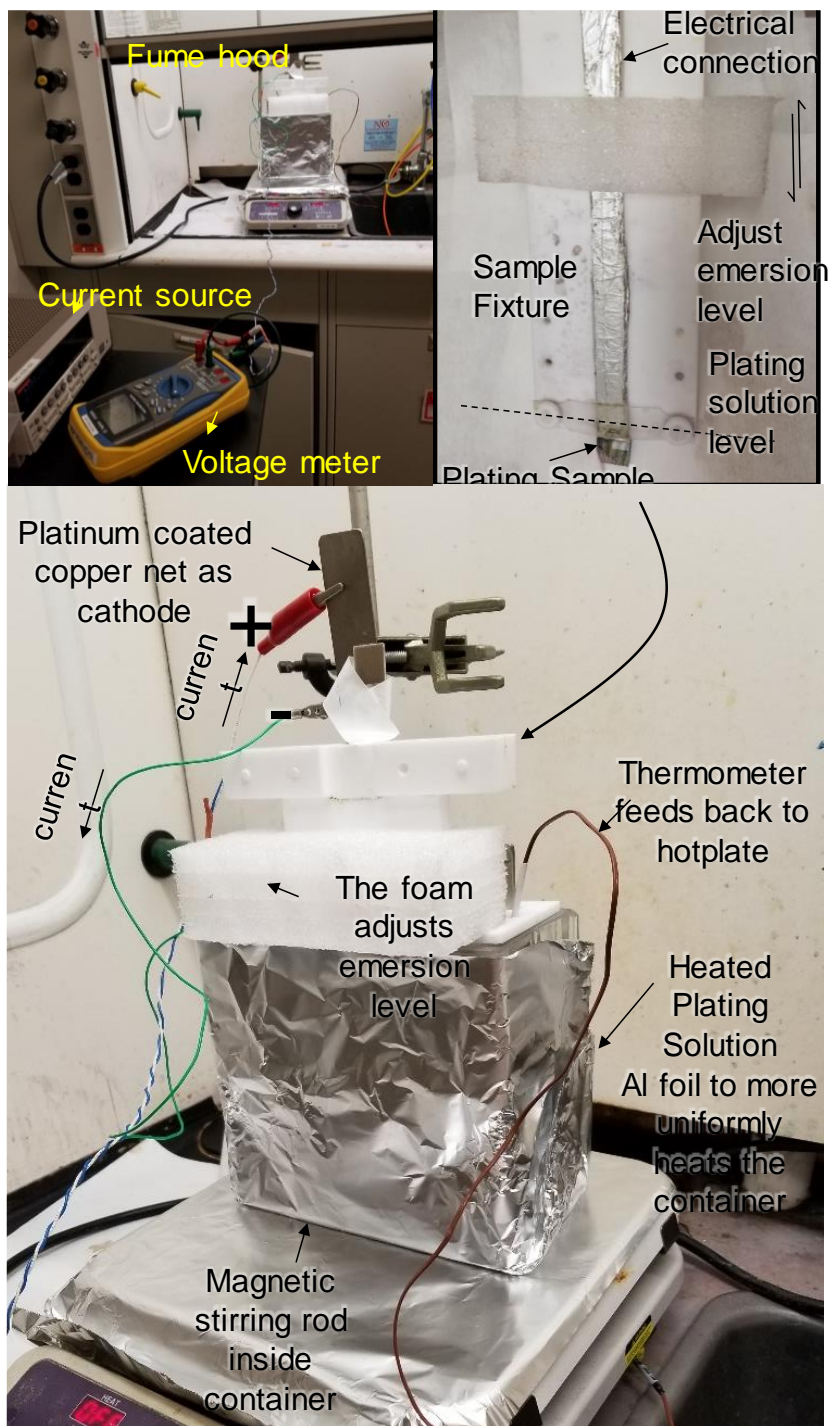
Figure 22: Old electroplating setup. Top left: The current source and the voltage meter connect to the plating setup in the fume hood. The experiment used both cyanide and sulfide plating solutions, so the setup is in the fume hood. Top right: The Teflon sample holder supported by a sliding foam. The fixture clamps the sample and electrically connects to the negative terminal of the current source. Bottom: Close-up of the plating setup. The figure shows the current direction and the hot plate configuration for keeping the solution at 60°C.

3.1.2.2 OXIDE MOLD ETCH

The 3µm of oxide mold is etched in a modified oxide spacer etch recipe using CF_4/CHF_3 chemistry. The low etch power in oxide spacer etch results in relatively good selectivity of about 4.5 to 1 (DUV PR: PECVD oxide) at the price of anisotropicity. The etch profile of the oxide mold has sloped sidewall and unfinished etch at corners as shown in Figure 24. To improve the etch profile, the process power is increased to 550W, but the selectivity drops to 4:1. To maintain the best lithography resolution, DUV photoresist of about 900nm acts as the etch mask as opposed to the 700nm to ensure complete etching.

3.1.2.3 ELECTROPLATING CONTACTS

In order to save cost, in this work, the sample sizes are 2-3cm square for electroplating tests. Clearing out electroplating contacts of 1cm wide for clipping shown in the electroplating setup in Figure 22. After etching oxide mold, the remaining PR strips in 60°C PRS3000 for 2 hours.

Figure 23: New plating setup. All fixtures are designed and custom made in Teflon. The sample fixture can also support 6" full wafer plating. The new setup better controls the electroplating parameters such as the spacing between cathode and anode; the depth of the sample in the plating solution; uniformity across samples, or even wafers etc.

Then a layer of 1µm G-line photoresist covers the 3µm oxide topography and Q-tip dipped in acetone swabbed open the contact areas. Next, soaking the samples in 5:1BHF for 10mins etch away oxide on the contact area. Finally, acetone strips the G-line protection photoresist.

3.1.2.4 SEED LAYER REMOVAL

Before electroplating, a 10secs dip in Cr-7 etchant after 30secs in HCl removes the top Cr layer. However, the oxide CF_4/CHF_3 etch makes the Cr layer hard to etch in Cr-7.

Repeating 10sec HCl and 10sec Cr-7 2-3 times is necessary to remove the Cr layer completely.

3.1.2.5 ELECTROPLATING RECIPE

The electroplating solution is Elevate 7990 sulfate-based Au solution whose chemistry is unstable. Therefore, once mixed, the shelf life is short. Over time, the solution develops brown gold colloid precipitates and the gold concentration drifts. The quality factor of the plated solution is around 300. The sulfide solution has a less stable chemistry than cyanide and therefore it has a short shelf life and is more susceptible to precipitation, which reduces the plating solution concentration in an uncontrollable fashion. After switching to a cyanide based electroplating solution Elevate 7934, the electroplating process stabilized. Figure 25 shows the released structures and at various current densities.

3.1.2.6 ELECTROPLATING SETUP
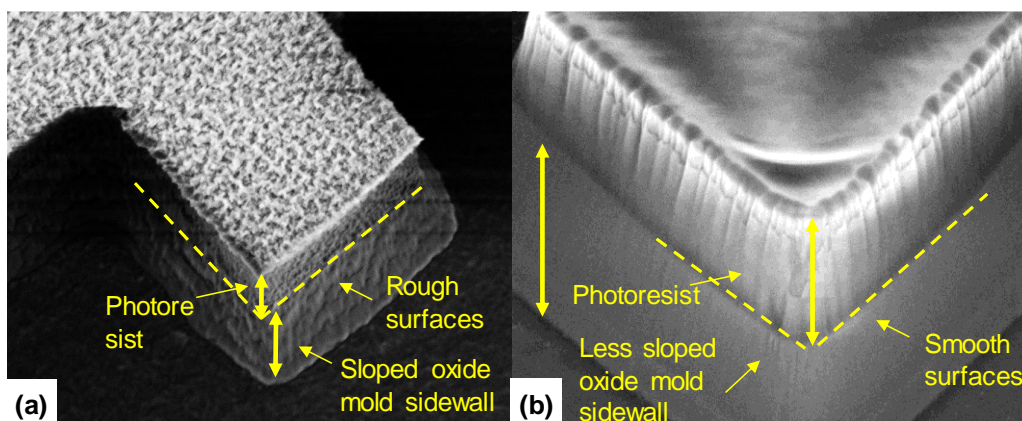
Figure 24: (a) 250°C PECVD oxide mold etching profile. The film is porous and the sidewall is very rough. (b) 300°C PECVD oxide mold etching profile, using the same etching recipe. The sidewall is smoother and less sloped.

CHAPTER 3 RESOSWITCH PROCESS DESIGN

Figure 23 shows the customized electroplating setup. The anode is a platinum-coated titanium web electrode. A Teflon bar held the anode against the back plate of the cover that guarantees that the anode is parallel with the sidewall of the tank. Another two Teflon bars screwed together at the ends sandwich the sample with the fixture plate that is as wide as the anode so that the sample is parallel with the anode to control the current density uniformity across the sample. The sample is free to slide along the fixture plate to adjust the depth of the sample into the solution, as well as laterally along the tank cover to tune the distance between the sample and the anode. The setup maximizes the degrees of freedom in the electroplating process. The entire setup sits on top of a hotplate. A temperature probe immersed in the solution controls the hotplate and keeps the solution at 60°C during electroplating. Alligator clips with a layer of inert coating connect the sample fixture and the cathode to the current source. Figure 23 Bottom figure shows the complete electroplate plating setup.

Figure 25: Electroplated structures under various current densities. (a):0.1mA/cm2; (b) 0.5mA/cm2; (c) 1mA/cm2; (d) 1.5mA/cm2

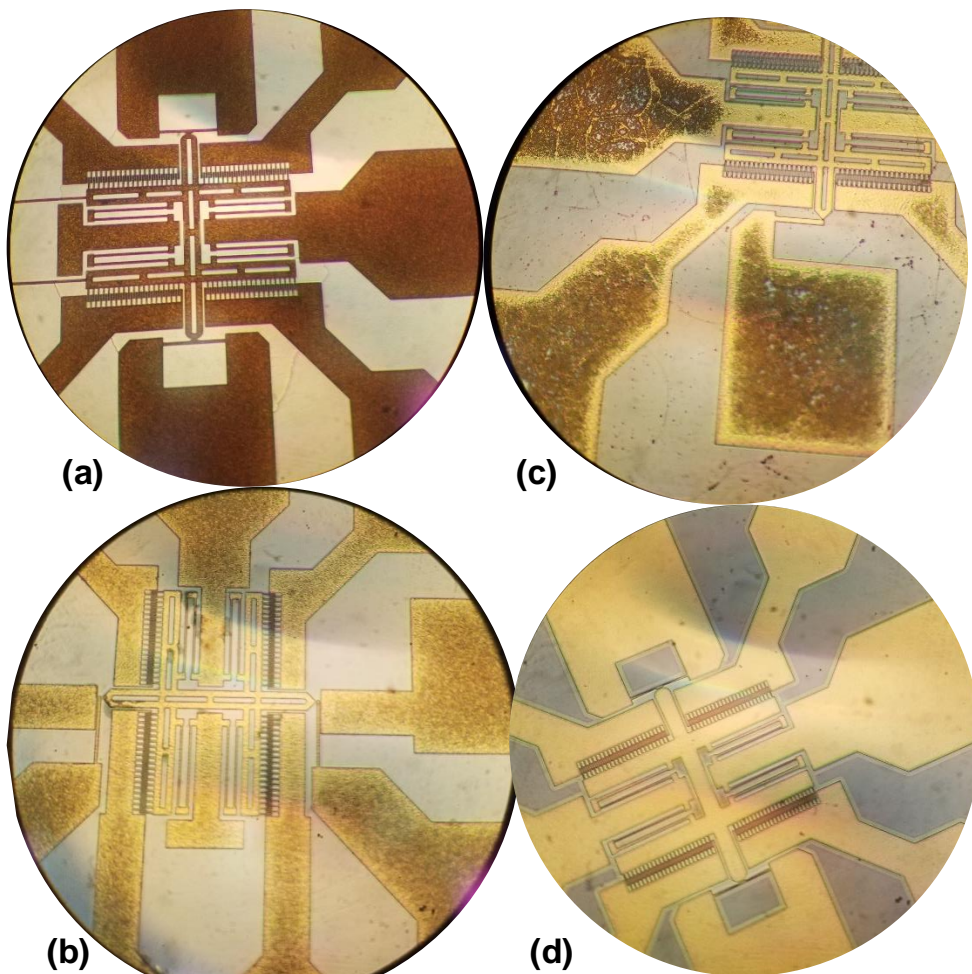## 3.1.3 POLYSILICON COMB-DRIVES

Electroplated gold structures achieved quality factor Q of more than 1000, which is on par with the best quality factors of electroplated gold in literature [38]. The later Chapter 4 and Chapter 5 demonstrate the switching results of the gold comb-driven devices. Gold has excellent contact resistance but limited reliability [39]. Q is also related to the sensitivity of the resoswitch and therefore, material such as polysilicon which has demonstration its capability to achieve Qs of 100,000 is of great interest [40] [41]. To maintain low contact resistance, the contact areas of the structure remains metal.

The idea is to have most of the resoswitch structure comprise polysilicon while the contact tips comprise metal. The initial implementation derives from the previous work [42] that selectively uses silicidation to keep metal on polysilicon structure. However, forming silicide creates stress and degrades the Q of the structure. Thus, the next step is to reduce the silicidation to only at the contact areas. Figure 26 depicts the process flow. Structural polysilicon is deposited and etched over the 2µm sacrificial oxide. The next step is lithography for lift-off. First, g-line photoresist is spun on the samples at 1krpm for 60secs to uniformly cover the 2µm topography. Then, contact aligner exposes a square area of 8µm by 8µm at the contact of the resoswitch. Due to the large topography, the resolution of the lithography is limited to large square areas. Next, 50nm of metal is sputtered on top of the photoresist and
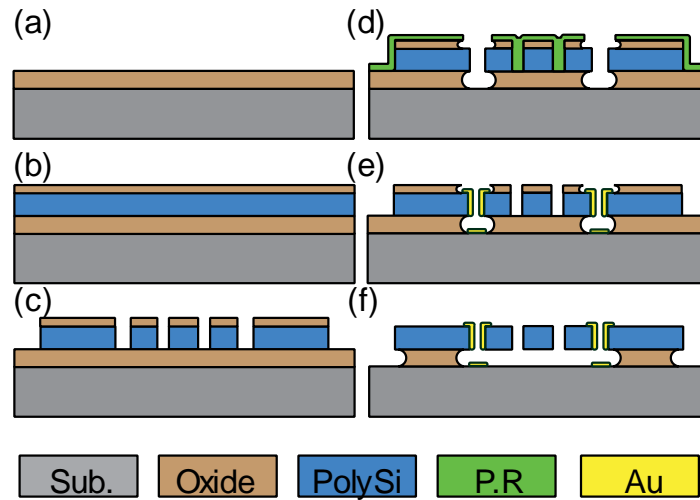
Figure 26: Metal contact resoswitch process flow. (a) Start from 2µm of sacrificial oxide. (b) Subsequently deposit polysilicon structure layer and the oxide hardmask to etch the polySi structure. (c) Etch the hardmask and then the polySi structure. (d) Photoresist covers most of the structures except for the contact area. (e) Evaporate Au and life off the photoresist leaving Au only on the contact area. (Later trails use sputtered Ru instead of evaporated Au to obtain better sidewall coverage) (f) Timed release in HF releases suspended structure.

CHAPTER 3 RESOSWITCH PROCESS DESIGN

lift-off process left metal only at the contact area. In order to ensure metal coverage on the sidewall of the contact, metal is sputtered on the slightly tilted sample. At last, the sample is heated to 950°C so that the metal on top of polysilicon forms metal silicide and the metal on oxide remains metal. Finally, soaking the sample in metal etchant removes the excess metal,
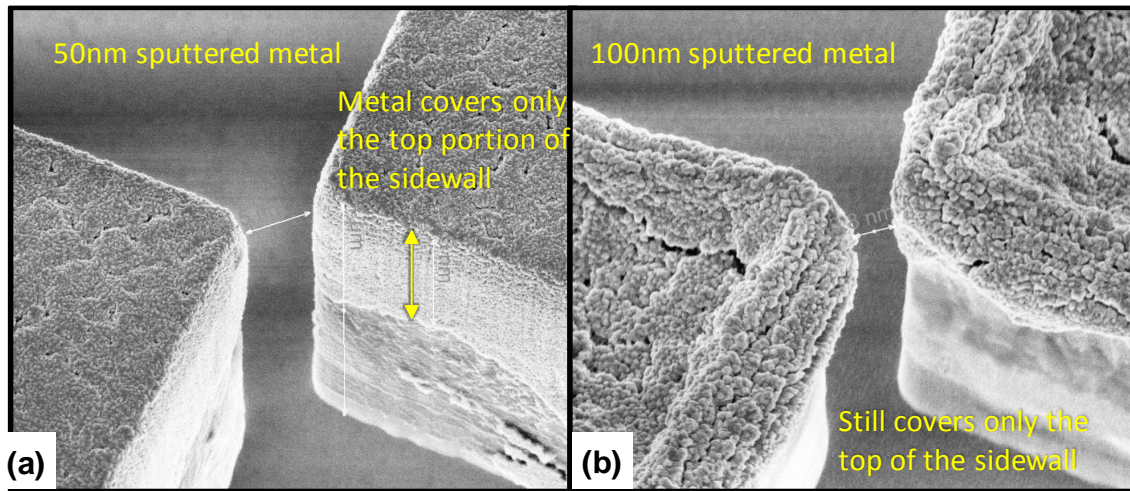
Figure 27: Sputtered metal on the resoswitch contact area. (a): 50nm sputtered metal. Only half of the sidewall thickness is covered by metal. (b): Increase the sputtered metal thickness to 100nm. The metal coverage of the sidewall is not improved. The excess metal just lumps at the contact top edges.
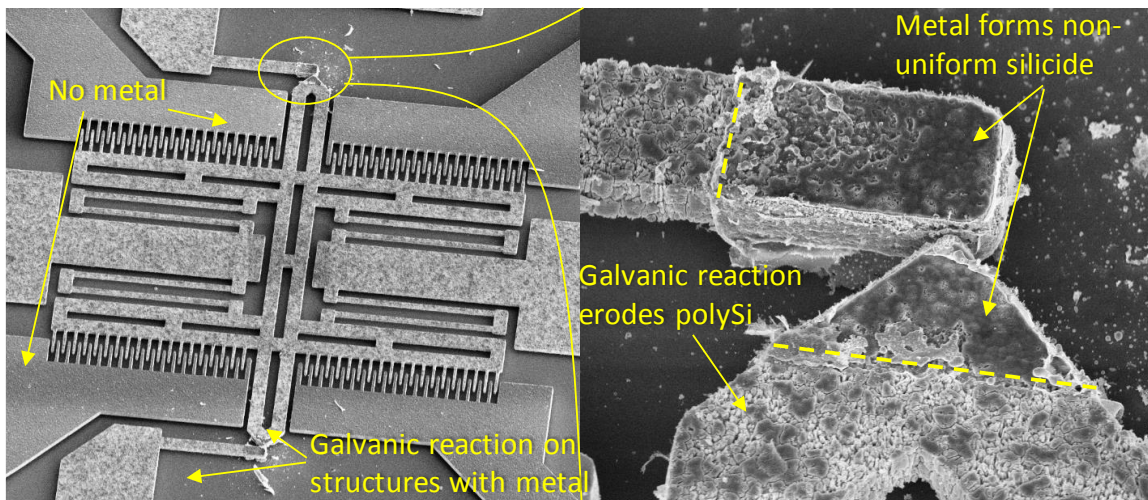
Figure 28: Released polySi silicide contact resoswitches. Left: Galvanic reaction between the metal and polySi erodes all structures with metal. The shuttle and the contact electrodes appear to be much rougher than the comb electrode that does not have any metal. Right: Zoomed in view of the contact point. The metal forms rough looking silicide. The HF release erodes the grain boundaries of the polySi outside the metal tips.

CHAPTER 3 RESOSWITCH PROCESS DESIGN

leaving only metal silicide on polysilicon structures. Silicidation only takes place at contacts and the stress from silicidation does not affect flexure beams.

However, the silicide resoswitches shown in Figure 28 only have a Q of over 1,000. The reason for the low Q is because of the galvanic reaction between metal and polysilicon during the metal removal step after silicidation. Galvanic reactions take place in an electrolyte between two conductors with different electrochemical potentials. In this case, metal etchant for Ru is a solution of (Cr-7) nitric acid and acetic acid and therefore is a strong electrolyte. Ru and polysilicon have different electrochemical potential [43]and thus electrons pass from Ru to polysilicon, oxidizing polysilicon especially at grain boundaries. The surface of
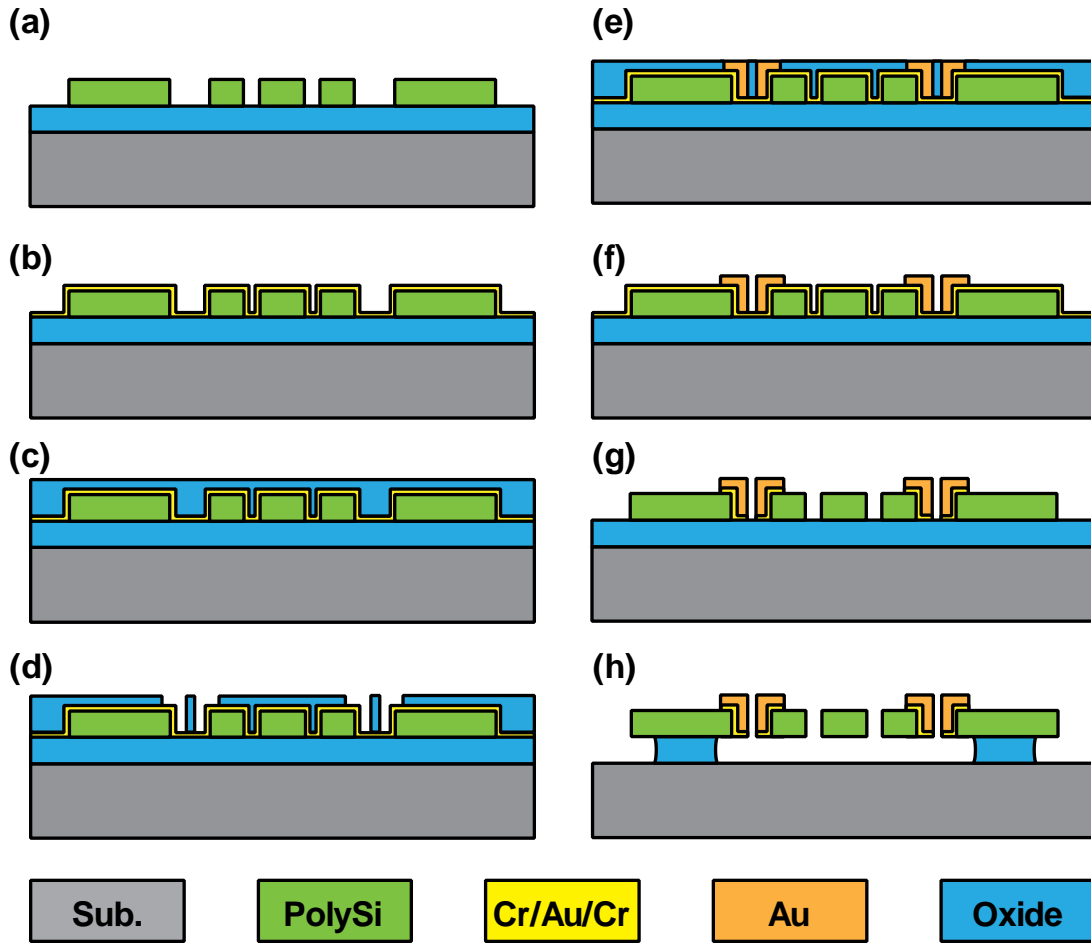
Figure 29: The process flow of the electroplated-contact resoswitch. (a) Deposit and etch 2µm polySi structure layer over 2µm sacrificial oxide. (b) Evaporate Cr/Au/Cr seed layer over the patterned structure. (c) Deposit oxide mold for electroplating and CMP to remove topography. (d) Etch contact plating-mold. The spacing between the two contacts is only 500nm. Flat surface with minimum topography helps achieve better lithography resolution. (e) Electroplate Au at the contact areas. (f) Remove oxide mold. (g) Etch seed layer in the field to expose sacrificial oxide. (h) Etch the sacrificial oxide and releases the structure.

CHAPTER 3 RESOSWITCH PROCESS DESIGN

polysilicon becomes very rough and porous as shown in Figure 28 [44], which leads to lower *Q*.

The resistivity of the metal silicide is also relatively high, at about 20µohm cm. Therefore, the contact resistance is several kΩs. To reduce the contact resistance further, the second version of the metal contact process uses electroplated gold for contact. Moreover, to minimize the expenses of making lithography masks, the mold for electroplating contact tips is composed of two different layers: one PR pattern and one oxide pattern.

i) Figure 29 shows the process flow of the first attempt. Due to the constraint of the process thermal budget, polysilicon structure is deposited and etched before evaporating the seed layer. Therefore, PECVD mold oxide that has to come on top of seed layer is deposited over 2µm of topography. The gaps between comb fingers range from 500nm to 1µm, which means aspect ratio of 4:1 to 2:1. Low temperature processes have worse conformality and form key holes at structures with high aspect ratios. On top of the large topography, lithography is difficult. Thus, the first attempt
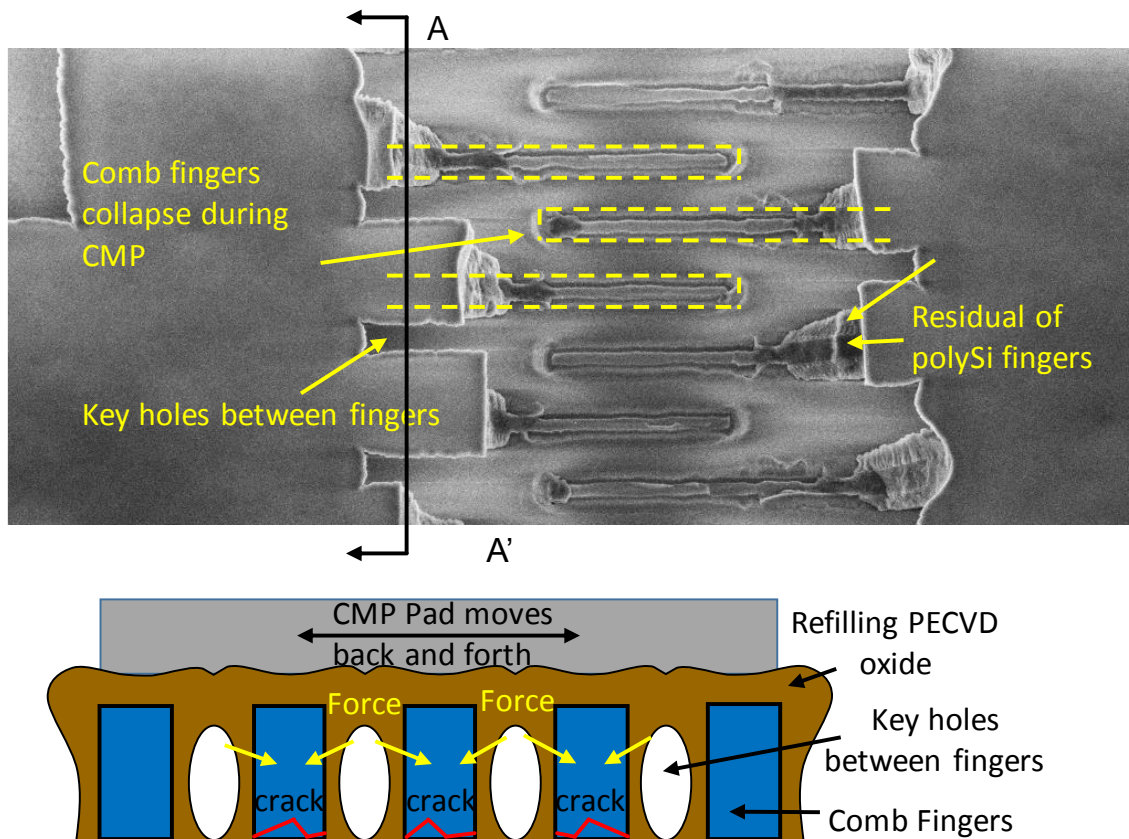
Figure 30: CMP of comb fingers filled with PECVD oxide cracks the fingers. The key holes between the fingers during the PECVD oxide refill leave the fingers unsupported. The force exerted on the fingers when the CMP pad polishes the wafer surface break the fingers.

is to planarize the oxide mold in a CMP process. However, the key holes between the comb fingers leave the fingers unsupported and fragile under the force of the CMP drag force. Figure 30 shows a SEM image of the fingers after CMP, where fingers are torn and broken. Some other oxide types such as flowable oxide (DOW Corning FOX 15) gave better conformality results, but no enough to protect the fingers from the CMP process.

ii) Therefore, the revised process shown in Figure 31 adds another oxide deposition followed by CMP planarization before seed layer deposition. The oxide filling achieved before the seed layer relaxed the thermal budget and allows for higher temperature oxide deposition such as LPCVD LTO at 450ºC or even HTO at 930ºC.
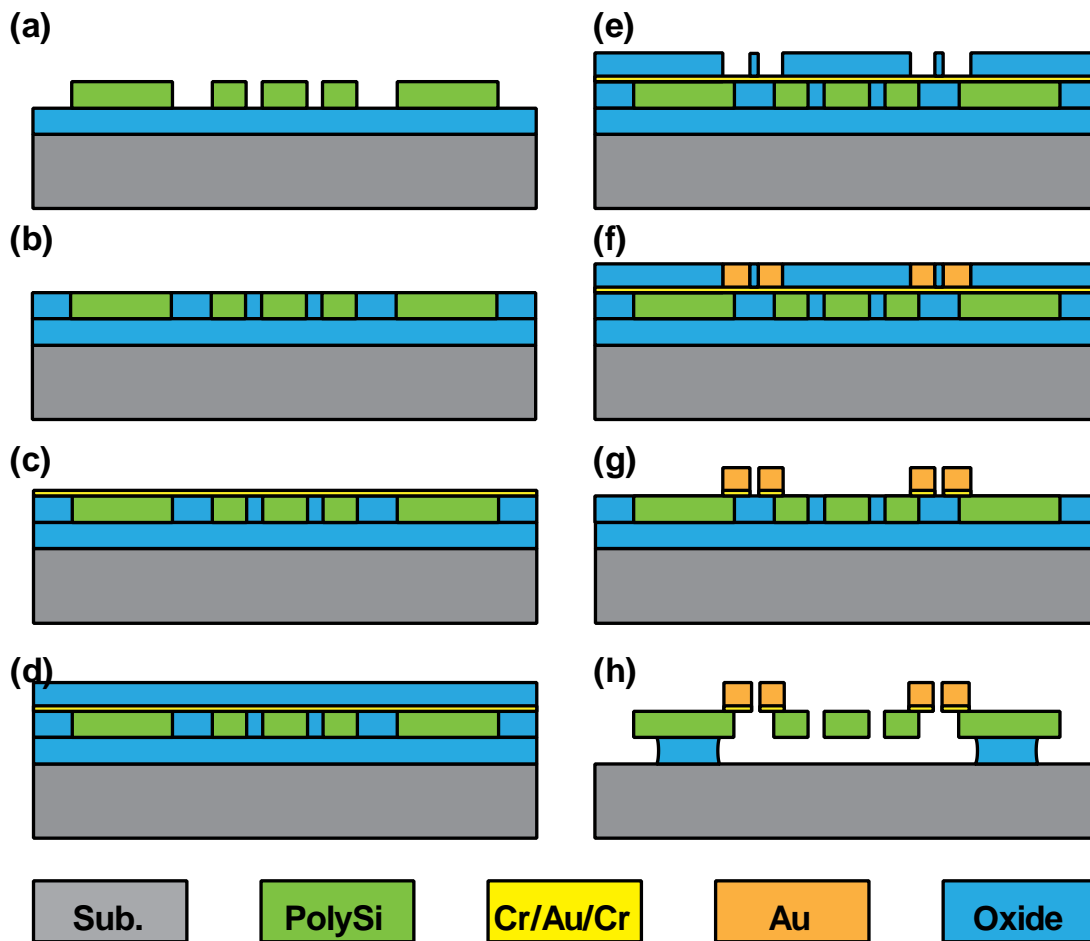
Figure 31: Revised electroplating contact resoswitch process. The difference between the revised process and the previous process in Figure 29 is the sequence of CMP. The seed layer is deposited after oxide refilling in step (b). Since the low temperature seed layer is deposited later, the refilling oxide can be high temperature LPCVD oxide that is more conformal and creates less key holes.

CHAPTER 3 RESOSWITCH PROCESS DESIGN

Figure 32 shows the result of LTO filling after CMP where key holes are still clearly present. Figure 32 shows the result of HTO filling where key holes disappear for features of aspect ratios smaller than 1:1. The key holes might still be present, but deeper into the trenches and the surface after CMP appears flat. In this process, the goal is only to have flat surface to ease the later process steps. Repeating filling and CMPing multiple times shrink the size of the keyholes on the surface, but excess CMP polish rounds off the corners of the polysilicon structures and changes device behavior. HTO deposition is extremely slow, therefore depositing 2µm of HTO several times by
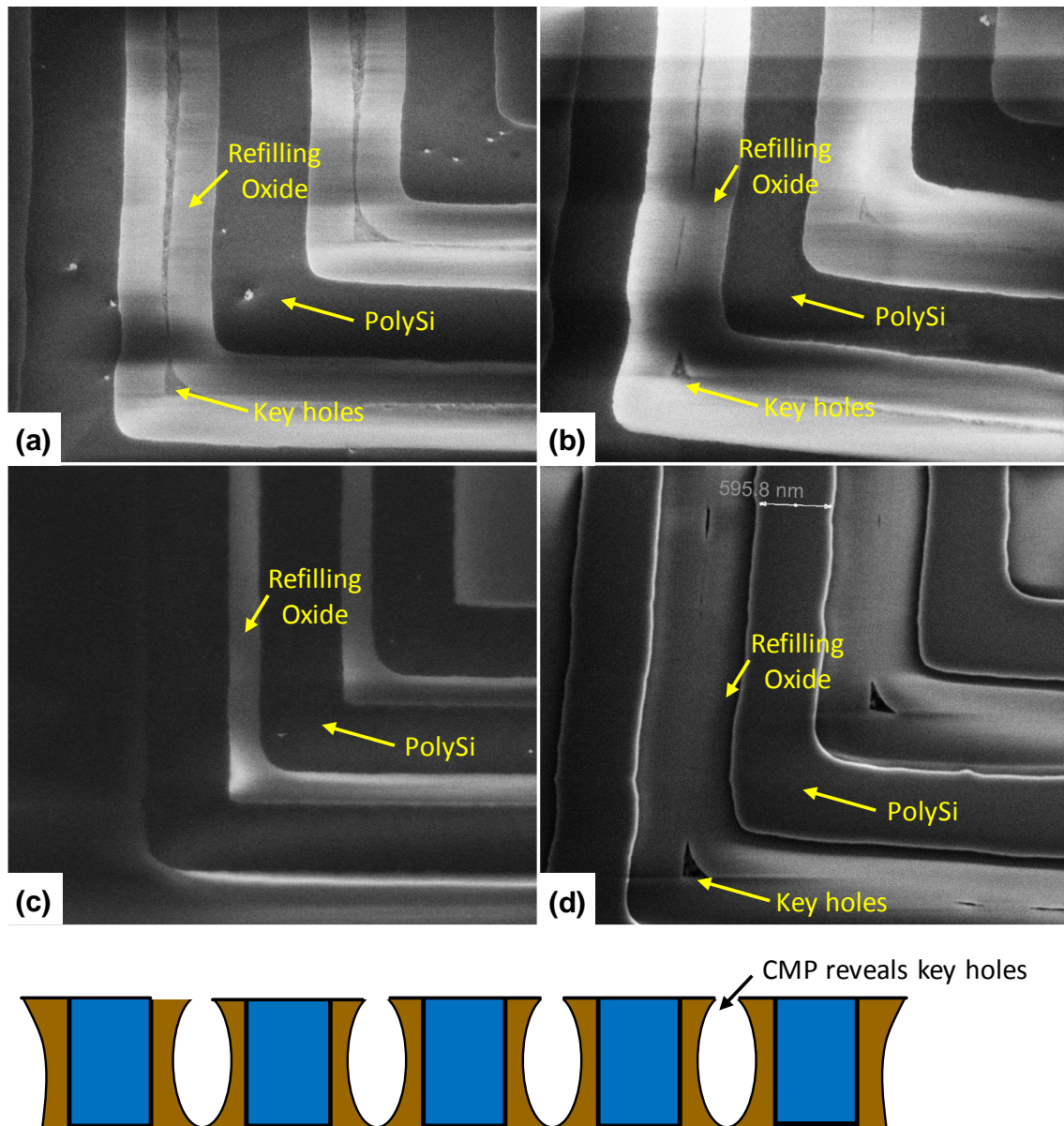
Figure 32: Different oxide refilling deposition recipe have different key hole effect. (a) LTO deposited at 450ºC. (b) Spin-on glass annealed at 950ºC. (c) HTO with lower pressure and thus slower deposition rate. (d) Standard HTO recipe at 915ºC.

itself takes several days and adds extra stress on the furnaces. Spin-on PSG followed by 1000°C reflow shown in Figure 32 has also better conformality than LTO refilling, but the quality of the oxide is poor. Small bubbles are visible everywhere in the field.

iii) Another option is to do a reverse filling. Instead of depositing oxide over defined polysilicon structure, use a negative structure mask to etch oxide then deposit polysilicon and cmp polysilicon to stop on oxide structures. Figure 32 presents the result after cmp. The holes on the surface are much smaller than refilling oxide.

iv) The process failed in the end due to poor adhesion of plated gold to seed layer on polysilicon. The electroplating process requires 2-3 times higher current density than plating on seed layer on oxide and the result is poor uniformity. The plated gold contact tips float away during the oxide-mold removal step.

As a result, sputtering replaced electroplating. Figure 33 describes the final process flow for polysilicon resoswitches with metal contacts. The metal contacts need to survive the oxide etch and have properties such as low contact resistance and inert to oxidation. Considering the ease of fabrication, the metal of choice is TiN/W. However, the majority of metals require a Chlorine or Fluorine based chemistry, which inevitably etches silicon at a much higher rate than etching metal. Therefore, the metal contact etch is divided into two steps: first, timed dry etch removes the top TiN but not all the W; then wet etch in H_2O_2 removes the rest of the W left. In this way, the initial dry etch preserves the resolution of the lithography pattern and wet etch in the end selectively removes the rest of the W. Figure 33 shows the released the structure with metal contact tips. To minimize galvanic reactions during metal etching and release, a buffer solution is added to the etchant to protect the silicon. Chapter 4 discusses in detail the frequency characteristic of the resonator with TiN/W tip that has a *Q* of 25,000, much higher than the previous attempts.
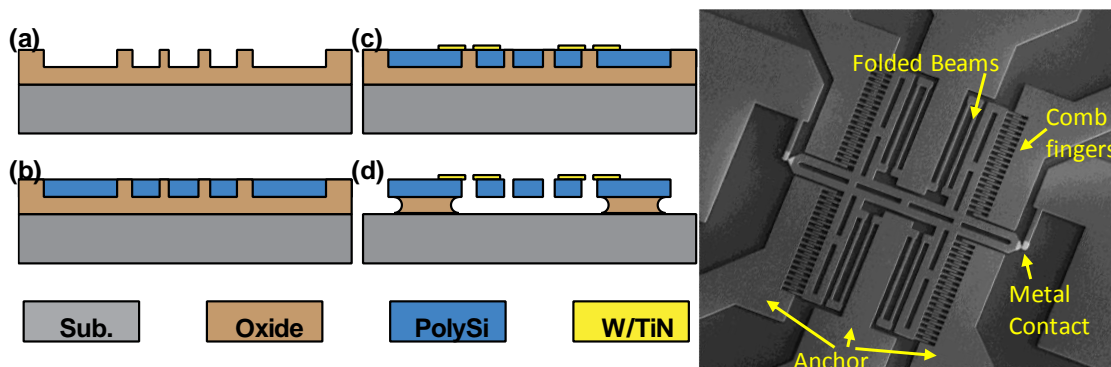

Figure 33: Sputtered metal W/TiN contact tip process. Sputtered W/TiN has good adhesion to polySi structure. The W/TiN is sputtered after CMP to provide flat surface for contact lithography. Etching W/TiN stopping on polySi involves a combination of plasma etch and wet etch of W.

Chapter 4 ALL-MECHANICAL RECEIVERS

4.1 ALL MECHANICAL FSK RECEIVER

A first-in-kind all-mechanical communication receiver front-end employing resonant micromechanical switch (i.e., resoswitch) technology has detected and demodulated frequency shift keyed (FSK) signals as low as −60dBm at a VLF frequency of 20kHz suitable for extremely long-range communications, all while consuming zero quiescent power when in standby. The key to attaining high quality signal reception and demodulation with zero quiescent power consumption derives from the use of heavily nonlinear amplification, provided by mechanical impact switching of the resoswitch. This approach would be inconceivable in a conventional receiver due to performance degradation caused by nonlinearity, but it becomes plausible here by virtue of the RF channel-selection provided by the resonant behavior of the mechanical circuit.

4.1.1 VLF COMMUNICATION

Very Low Frequency (VLF) and Low Frequency (LF) receivers operating from 3-30 and 30-300 kHz, respectively, with wavelengths on the order of kilometers, present a compelling opportunity for very long-range communications, such as depicted in Figure 34. In particular, while high frequency radio waves propagate omnidirectionally along line of sight paths, so suffer from free space path losses proportional to the square of the distance between transmitter and receiver; VLF and LF signals propagate by surface wave through an effective waveguide formed by the ionosphere and the earth that confines their energy to follow the curvature of the earth, and hence,

Figure 34: VLF and LF communication is possible over thousands of miles, practically crossing continents.

CHAPTER 4 ALL-MECHANICAL RECEIVERS

suffer less loss [45]. Time transfer over long distances presently use such frequencies, where their propagation by ground wave eliminates multipath issues, ultimately helping to maintain timing precision. Smaller, zero quiescent power versions of such receivers would expand the application set to sensors and other autonomous devices that could be commanded or interrogated from hundreds of miles away.

Unfortunately, operation at such low frequency generally entails the use of large electronic components. In addition, conventional linear approaches to receiver design fall well short of zero quiescent power. A nonlinear approach that could dispense with the power needed to maintain linearity would fare much better. Recognizing this, the approach taken here first harnesses the much smaller acoustic wavelengths of mechanics to allow substantially smaller size than electronic counterparts; and second, dares to employ a very nonlinear mechanical amplifier that becomes key to zero standby power. Use of this approach yields a first-in-kind all-mechanical communication receiver front-end, shown in Figure 35, employing a resonant micromechanical switch (i.e., resoswitch) detects and demodulates frequency shift keyed (FSK) signals as low as −60dBm at a
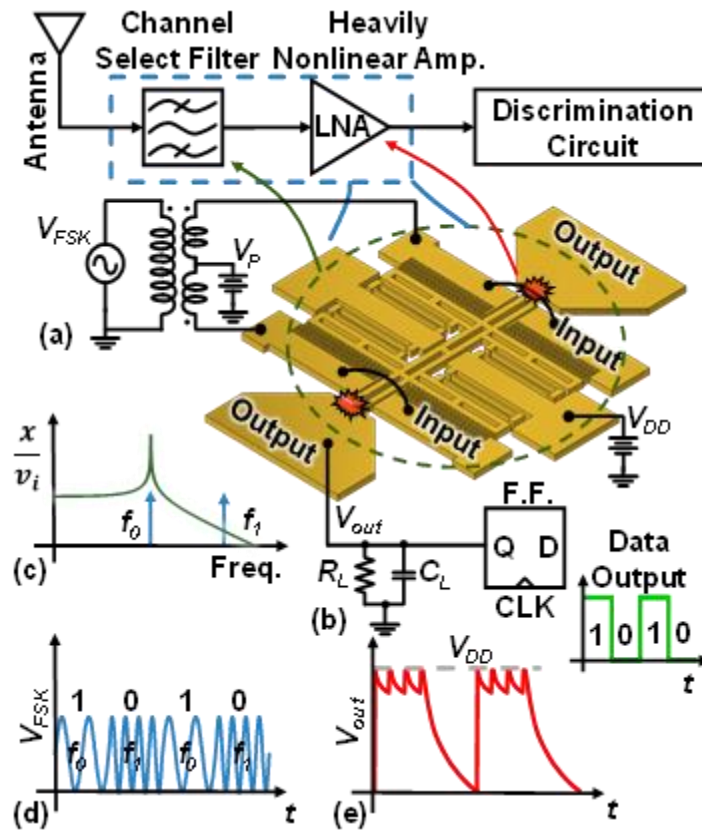

Figure 35: Summary description of the mechanical receiver. (a) A resoswitch serves as a combined channel-select filter with response in (c) and nonlinear amplifier feeding load (b) while consuming zero quiescent power. A (d) FSK input signal generates the output in (e), which in turn produces the bit stream (green) at the flip-flop output.

VLF frequency of 20kHz suitable for extremely long-range communications, all while consuming zero quiescent power when in standby.

4.1.2 RECEIVER STRUCTURE AND OPERATION

Figure 35 summarizes the overall receiver structure and operation, where practically all of the front-end functionality relies on a single micromechanical resonant switch (a.k.a. resoswitch) shown more clearly in Figure 36. As shown, the low frequency resoswitch used here comprises a folded-beam-supported comb-driven resonator with a pair of output electrode impacting points at both sides of the shuttle. Four pairs of 60µm-long folded beams suspend the resonator shuttle from central anchor points. To suppress squegging [42], this resoswitch differs from previous ones in its use of fully differential input comb electrodes and impact points, both of which help to overcome impact-induced energy loss. If the differential ac input signal shown is off-resonance, the resoswitch does not move enough to overcome the air gap of d_0 separating the shuttle impact points from the output electrodes, so is electrically open. When the input signal is on or near resonance and has sufficient amplitude, the shuttle vibrates with a large enough amplitude to periodically impact the output electrodes, effectively closing the shuttle-to-output switch at the in-channel signal frequency.

4.1.3 RESOSWITCH FILTER-LNA

The described resonant switching behavior allows the resoswitch to function effectively as a "filter-LNA", such as shown in Figure 35(a). This of course is a series of functions needed in any receiver front-end, but in this case realized via a single device with a heavily nonlinear impact-based amplifier that outright enables zero quiescent power operation.
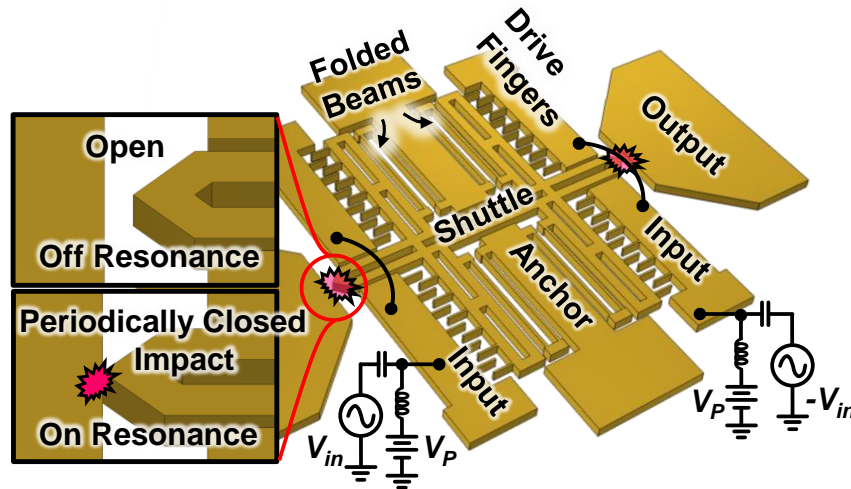

Figure 36: Schematic zooming in on the impact point for off- and on-resonance inputs.

CHAPTER 4 ALL-MECHANICAL RECEIVERS

To see how, consider that the simplest receiver front-end consists of merely an amplifier immediately following the sensor, e.g., an antenna. If the amplifier is a transistor amplifier, then the finite threshold voltage and subthreshold slope of its transistor switching device precludes on/off switched operation, since the microvolt level inputs typically received are not large enough to induce switching over sub-millisecond integration times. Rather, the transistor must be biased at a high gain operating point, where significant dc current flows; hence, significant power consumption ensues, as shown in Figure 37.

On the other hand, a conventional aperiodic MEMS switch's on/off switching slope is nearly infinite. Unfortunately, its threshold voltage is even larger than that of a transistor, with values ranging from 6V for NEMS logic switches [46] to 85V for RF MEMS switches [36].

The resoswitch used here solves both problems, with not only an effectively infinite on/off slope similar to the aperiodic switch, but also an ability to switch with very low power inputs enabled by Q multiplication of its displacement at resonance. The impulsive contact force of resonance impacting operation also improves contact resistance and reliability, making possible measured cycle counts greater than 170 trillion [17], which is several orders higher than aperiodic counterparts. The constraint to resonant or periodic inputs is actually not a constraint at all for an RF front-end application, and is in fact a benefit when one considers the well-known pitfalls of nonlinear signal processing, especially for receivers.

Indeed, conventional receivers attempt to avoid nonlinearity as much as possible, since nonlinearity generates spurious signals from interfering signals that can mask the desired signal, as shown in Figure 38. The power consumption of a receiver in fact derives in large part from a need to keep the front-end linear, where higher linearity requires more power. However, raising power consumption is not the best way to combat nonlinearity. Rather, a much better approach is to eliminate interferers before they experience nonlinearity and generate spurs, as explained in [47]
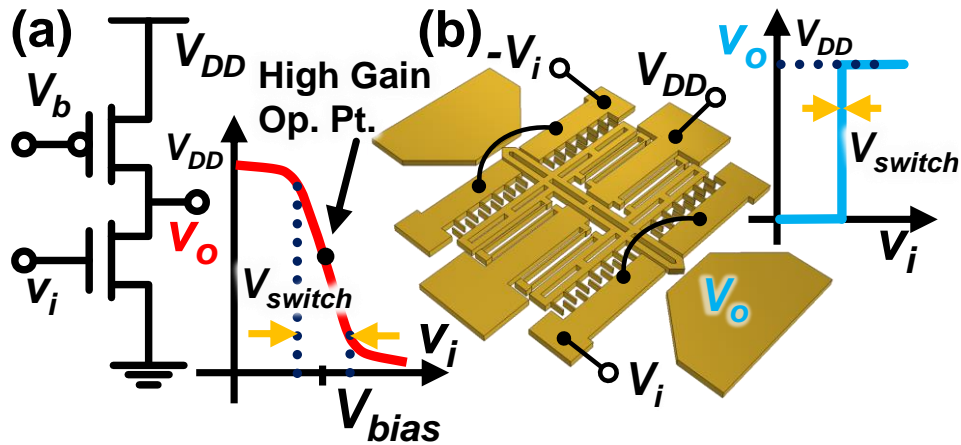

Figure 37: Voltage transfer characteristics (VTC's) of (a) a transistor amplifier, and (b) the resoswitch.

and shown in Figure 38. No interferers, no spurs. Herein lies the beauty of the resoswitch: Its frequency response essentially functions as a built-in channel-selector that filters out all interferers, thereby eliminating nonlinear spurs and enabling its own heavily nonlinear, zero-quiescent power, impact-switching amplifier!

4.1.4 PRACTICAL RECEIVER OPERATION

As shown in Figure 35(a), the receiver takes as input a differential ac signal $\pm(1/2)V_{FSK}$ combined with a dc bias voltage V_P applied to resoswitch comb electrodes on opposite sides. A dc voltage source V_{DD} tied to the shuttle as shown in Figure 35 (a) serves as the supply to be switched to the output upon impact with the switch electrodes.

When the frequency of V_{FSK} is within the frequency passband of the resoswitch, the shuttle vibrates laterally with an amplitude approximately Q times larger than would ensue with an out-of-band input. If V_{FSK} induces a shuttle displacement larger than the switch gap d_0, the shuttle periodically connects the output to V_{DD} and delivers power to output load R_L and C_L. Figure 39 shows measured input and switch output waveforms for R_L=160kΩ and C_L=100pF. In the receiver schematic of Figure 35(a), a flip-flop following the RC circuit then latches the output to provide a more stable sequence of 1's and 0's to the next stage.

The minimum input power that drives the shuttle to displace d_0 governs the ultimate sensitivity of the receiver, which takes the form

$$S = \frac{d_o^2 k_m \omega_o}{Q} \tag{4.1}$$
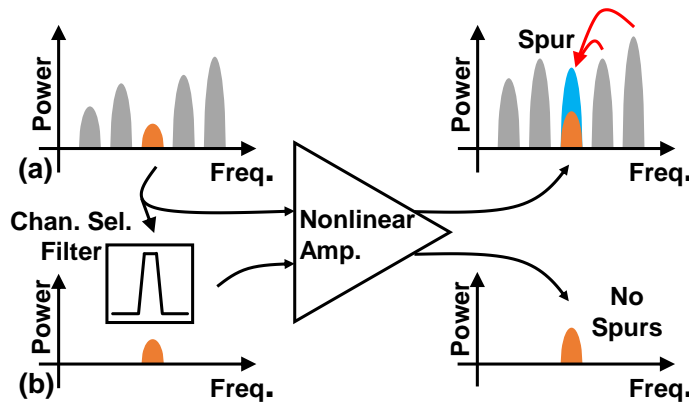
Figure 38: (a) With interferers present, nonlinearity generates spurious signals from those interferers that can mask the desired signal. (b) Removal of all interferers via a channel-select filter removes the source of the spurs, allowing subsequent nonlinearity with little consequence.

CHAPTER 4 ALL-MECHANICAL RECEIVERS

where k_m is the dynamic stiffness of the resoswitch at the shuttle location [48]. Clearly, the smaller the switch gap spacing and higher the Q, the better the sensitivity.

4.1.5 FABRICATION

Figure 40 describes the process flow used to fabricate the resoswitch. The process begins with deposition of 2µm sacrificial LPCVD oxide atop a starting silicon substrate. A seed layer comprised of 7nm Cr/20nm Au/20nm Cr is then evaporated. The bottom layer of Cr serves as an adhesion layer, while the top Cr protects Au during subsequent etching. Next, 3µm of PECVD oxide is deposited as mold material for electroplating, followed by photolithography and etching
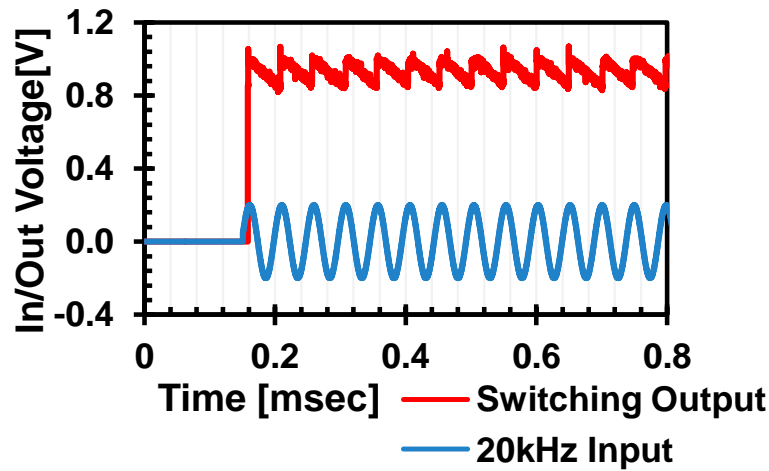
Figure 39: Measured time domain plot of the resoswitch output in response to a 20-kHz on-resonance input that induces impacting, connecting V_{DD} to the output and allowing it to deliver power.
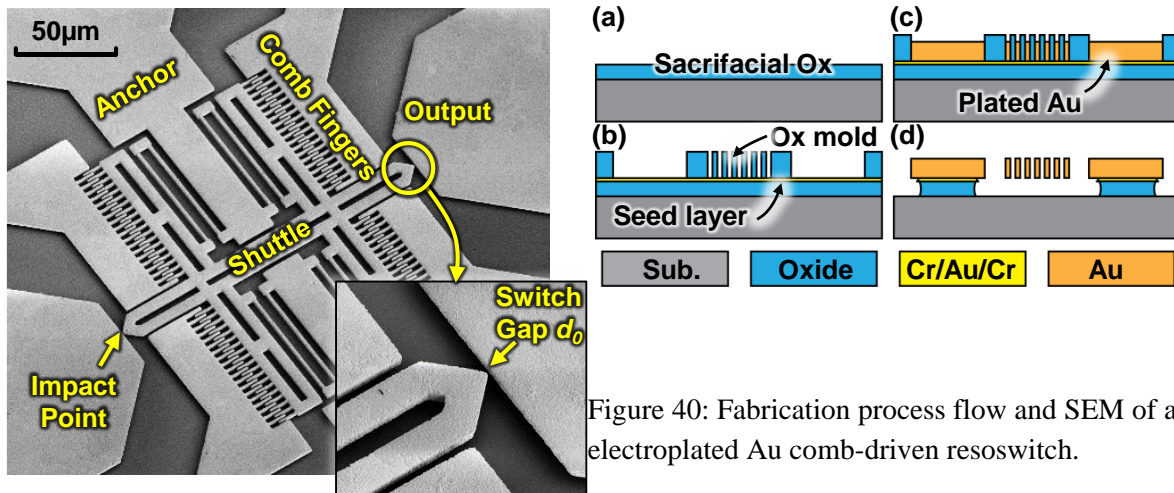
Figure 40: Fabrication process flow and SEM of a electroplated Au comb-driven resoswitch.

CHAPTER 4 ALL-MECHANICAL RECEIVERS

to define the mold in (b). Use of this oxide mold allows higher resolution i.e., smaller gaps, compared to conventional photoresist molds, which helps sensitivity per (3). This process achieved 800nm gaps between comb fingers, to compare with the 1.5µm of a previous PR-based mold process [21].

After a short dip in Cr etchant Cr-7 to remove the top protection Cr layer, electroplating in a sodium gold sulfite solution forms resoswitch structures over exposed regions of Au seed layer. Next, a short dip in hydrofluoric acid (HF) followed by Cr-7 and Au TFA etchants removes the oxide mold and the metal seed layers. Finally, a timed etch in HF releases the structure while preserving sacrificial oxide under the large area anchors.

Figure *40* presents the SEM of a released Au resoswitch with a zoom-in on the switch impact point.

4.1.6 EXPERIMENTAL RESULTS

A Lakeshore FWPX vacuum probe station provided the 1mTorr pressure and low-capacitance probes needed to evaluate receiver performance. A Tektronix AFG3200 signal generator provided modulated inputs, while the *RC* and flip-flop demodulation stages were realized on a pc board.

4.1.6.1 FSK SIGNAL DEMODULATION

Figure 41 plots the signal waveforms at different points in the receive chain. As shown, the input of Figure 35(a) comprises an FSK modulated random series of data bits "0" and "1", where bit "0" denotes an off resonance frequency at 50kHz and "1" denotes a resonance input at 20kHz. This

Figure 41: Waveforms at various points of Figure 35 showing successful recovery of a FSK modulated input waveform, confirmed by matching input and output bit streams.

CHAPTER 4 ALL-MECHANICAL RECEIVERS

signal passes through a balun to generate differential inputs that combine with a dc bias V_P of 16V then proceed to resoswitch comb electrodes on opposite sides. A "1" input with sufficient amplitude drives the resoswitch to resonance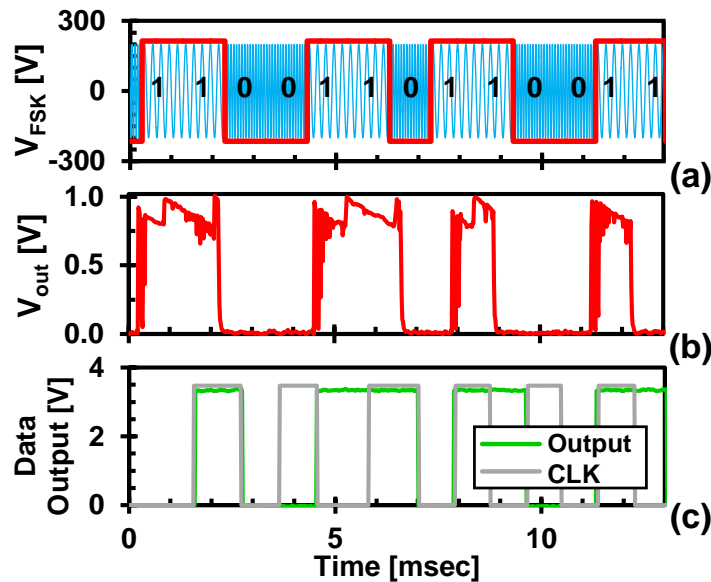 impacting, which then drives the output to $V_{DD} = 1V$. Input powers as low as -60dBm were sufficient to incite impacting at the output node, which then delivered -11dBm to the backend circuit. This equates to more than 49dB of power gain, all generated via a mechanical switching mechanism.

On the other hand, an off-resonance "0" input barely moves the resoswitch shuttle. There is no impact, so the output sinks to ground via bleed resistor R_L. As advertised, the receiver front-end consumes no power when receiving out-of-channel inputs.

Since a true FSK receiver detects both 1's and 0's, the present receiver that explicitly detects only 1's is actually operating in an on/off key (OOK) fashion. Addition of a second resoswitch that specifically detects 0's, so that both 1's and 0's are detected and processed, is all that is needed to make a true FSK receiver.

The *RC* circuit ultimately governs the bit rate f_b of the present receiver, where proper operation ensues when

$$\frac{1}{2\pi f_o} < R_L C_L < \frac{1}{2\pi f_b} \tag{4.2}$$

When R_L and C_L take on values of 160kΩ and 100pF, respectively, Figure 35(b) indicates that the output easily keeps up with a 1kbit/s input bit rate. Note, however, how the output vacillates somewhat at the beginning of each "0" to "1" transition, perhaps indicating squegging-related instability even with the new resoswitch design. Elimination of this phenomenon awaits further investigation.

In the meantime, the receiver of Figure 35(a) simply suppresses output instability by latching to a flip-flop that then presents the stable output shown in Figure 35(c). In this scheme, the first valid "1" is used as a pilot to start the synchronizing clock needed for latching.

4.1.6.2 FREQUENCY MASK

Figure 42 plots the minimum input power required to instigate reliable impacting, and thus, produce an output, at various input frequencies. The transition from in-channel to out-of-channel is impressively abrupt and quite suitable for high-density packing of adjacent channels. Due to an impedance mismatch between the device input and the 50Ω signal generator, the largest available off-resonance signal power for testing was -14dBm. As shown, out-of-channel inputs with this power did not induce output switching, so were rejected. Theory further predicts that 0dBm signals, if they were available, would also be rejected.

CHAPTER 4 ALL-MECHANICAL RECEIVERS

It should be noted that LF receivers commonly post input impedances on the order of 40k Ω [49], which match well to magnetic loop near-field antennas. This value is within the range of comb-driven resonator devices with sufficient bias voltage and small finger-to-finger gap spacing [50]

4.1.7 CONCLUSION

The demonstrated all-mechanical OOK receiver front-end that detects and demodulates a 20kHz FSK signal at −60dBm, while consuming zero quiescent power, poses some very interesting application possibilities, especially when one recognizes the importance of low power consumption for future sensors to be used in the internet of things. The zero quiescent power consumption of the demonstrated receiver is especially interesting for applications that must "listen" continuously. Perhaps, even more compelling is the actual demonstration via this work of a receiver that embraces hard impacting nonlinearity to reduce power consumption, while alleviating detriments via channel-selection. The sensitivity and frequency range of the present work are conservative, but versions capable of -100dBm sensitivity and operation past VHF are conceivable and the subject of ongoing research.

4.2 ALL MECHANICAL RECEIVER – AM RECEIVER

A micromechanical resonant switch-based envelope detector employing a soft-impact cantilever output electrode to affect a linear input amplitude-to-output level gain has successfully received, filtered, amplified, and demodulated an input AM signal over a 63-kHz carrier, effectively demonstrating a zero-quiescent power AM receiver to complement a previous such FSK receiver [51]. The RF front-end achieves a power gain of 30dB and demodulates without needing a power hungry local oscillator. Key to operation as an AM receiver is the linear analog amplification (as opposed to binary amplification of [51]) enabled by the flexible soft-impact output electrode. The
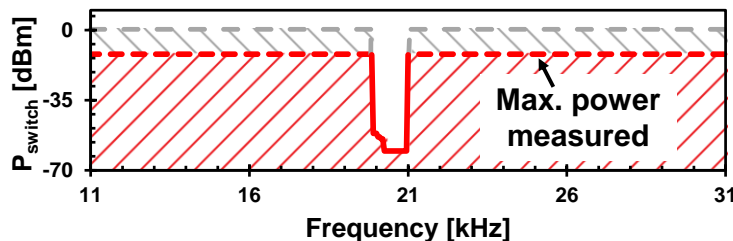

Figure 42: Frequency mask plot showing the powers needed to instigate impacting, and thus, produce an output, at various input frequencies. Although -14dBm was the maximum input power available for this measurement, rejection of out-of-channel powers higher than 0dBm are also conceivable.

higher Q of 1200 of the polysilicon device with Ru-silicide contact further increases the receiver sensitivity to −68dBm, which is 8dB better than that of [51]. The ability of this device to AM demodulate while consuming zero power during standby periods makes it ideal for use in ultra-low power long-distance receiver applications, such as the clocks that wirelessly receive atomic clock time over thousands of miles via AM over a 60-kHz carrier [16].

4.2.1 AM COMMUNICATION MOTIVATION

Low frequency (LF) wireless communication from 30-300 kHz has the unique ability to transfer information over thousands of miles [16]. Radio clocks that acquire atomic time from centralized locations (e.g., from NIST in the U.S. via AM at 60 kHz using the WWVB standard [16]) are perhaps the most recognizable consumer applications in this frequency range, but there are other less known, but important, positioning and communication applications. Thanks to the long-range nature of LF signals, a single base station can broadcast over the entire U.S.

If LF receivers could occupy single chips and consume zero power while actively listening for incoming information, then this frequency band might also be useful for updating of consumer products, e.g., firmware updates that do not require interconnect connection. This would make for a compelling application for the all-mechanical zero-quiescent power OOK receiver front-end of [51] that utilized micromechanical resonant switches (resoswitches) to demodulate FSK signals.

Smaller size and zero-quiescent power consumption would also be beneficial for the aforementioned time transfer applications. For these, however, the WWVB standard calls for AM modulation, rather than OOK, or even FSK. Like their aperiodic mechanical switch brethren used for RF switching [52] and more recently for digital logic [53], the resoswitches used in [51] have abrupt on/off transitions—something very useful for their prescribed applications, but not so useful for AM demodulation, which requires a more gradual transition from "off" to "on", preferably a linear gain profile, as illustrated in Figure 43.
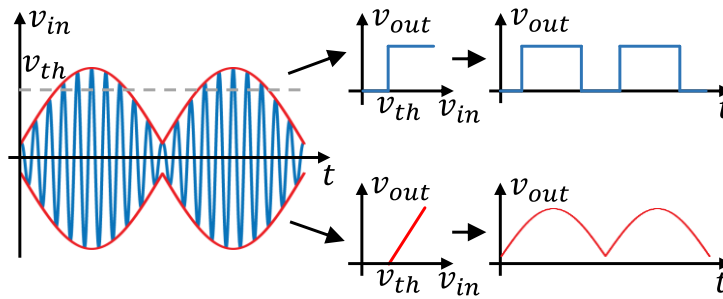
Figure 43: (Top): Abrupt on/off transition removes AM information. (Bottom): Gradual gain characteristic preserves the AM signal envelop, allowing AM demodulation.

CHAPTER 4 ALL-MECHANICAL RECEIVERS

Pursuant to enabling AM detection and demodulation at LF, this work presents a resoswitch design that employs a soft impact electrode to provide a linear gain profile. This, in addition to its inherent resonance-enabled frequency selectivity, allows the device to select a desired 63-kHz AM carrier, provide power gain, and envelop-detect (demodulate) the signal, all while consuming zero quiescent power.

4.2.2 AM RECEIVER STRUCTURE AND OPERATION

Resonant impacting also enables demodulation, the type of which, i.e., OOK, FSK, or AM, depends upon the hardness of the contact.

4.2.2.1 HARD VERSUS SOFT CONTACT

Figure 45 (a) and (b) respectively illustrate the differences between the hard contact of previous work [51] realized using an output switch electrode firmly clamped to the substrate; and the soft contact of this work, realized by a cantilever structure that bends when experiencing an impact. In each case, the impact electrode sits x_0 away from the tip of the shuttle at rest.

The hard and soft contact cases illustrated in Figure 45 differ in the slopes of their input-amplitude versus output voltage curves, where the former's is quite large, to the point of realizing a practically
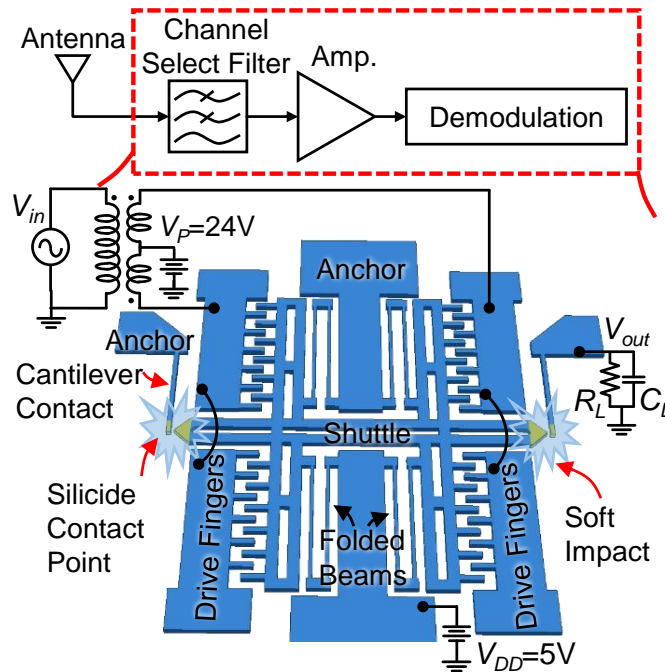
Figure 44: Schematic summary illustrating the AM receiver functionality of the soft-contact resoswitch device. Here, following the antenna, the resoswitch with silicided soft-electrode contact filters out interferers and envelop-detects the input AM modulated signal in one device.

CHAPTER 4 ALL-MECHANICAL RECEIVERS

instantaneous on/off transition; and the latter's much smaller, allowing for a slower transition that enables AM demodulation.

The reason for the difference between the two lies in the contact force, which takes the form

$$F_c = \frac{m_1(v_1' - v_1)}{t_c} \tag{4.3}$$

where m_1 is the shuttle mass, t_c is the contact time, and v_1 and v_1' are the pre- and post-impact velocities, respectively, of the shuttle. In the hard-contact scenario of Figure 44(a), the electrode remains stationary during impact and the shuttle recoils after impact at

$$v_1' = -rv_1 \tag{4.4}$$

where r $(0 < r < 1)$ is a coefficient that accounts for the energy loss due to impact, governed mostly by properties of the contact material, e.g., hardness, roughness, etc.

On the other hand, when the contact electrode is a compliant cantilever, as in Figure 44(b), the impact does not reverse the direction of the shuttle's velocity, and

$$v_1' = sv_1 \tag{4.5}$$

where s $(0 < s < 1)$ is determined by contact dynamics governed largely by the mechanical impedance of the cantilever, especially if its stiffness k_2 is much smaller than the contact stiffness due to material hardness. The output voltage derives from a resistive divider

$$v_{out} = \frac{R_L}{R_{on} + R_L} V_{DD} \tag{4.6}$$
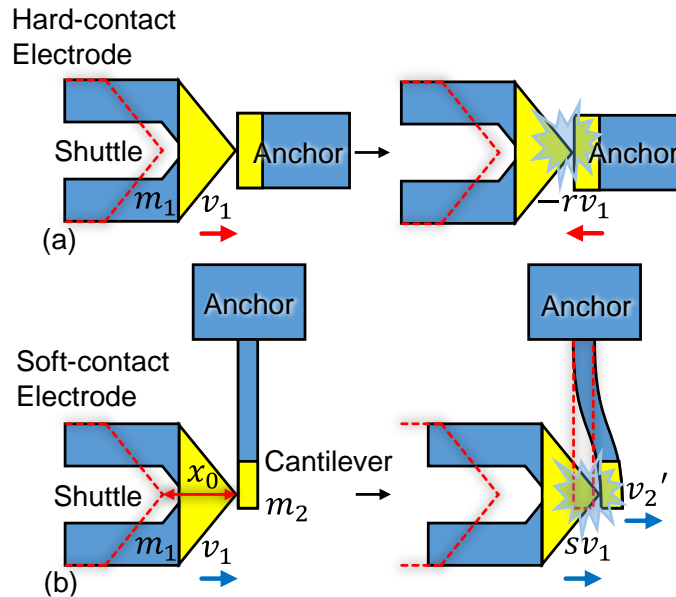
Figure 45: Illustrations describing the contact dynamics of soft and hard contact electrodes. The hard-contact electrode (a) reverses the shuttle direction, while the soft-contact electrode (b) merely yields to the shuttle.

CHAPTER 4 ALL-MECHANICAL RECEIVERS

where

$$R_{on} \approx R_o - \varphi F_c \qquad (4.7)$$

where R_o is a low contact force initial resistance, and φ models the dependence of contact resistance R_{on} on contact force [54]. Combination of (1) to (5) then yields

$$v_{out} \approx \begin{cases} \dfrac{m_1 \varphi V_{DD}}{t_c R_L}(1+r)v_1 \ (hard\ contact) \\ \dfrac{m_1 \varphi V_{DD}}{t_c R_L}(1-s)v_1 \ (soft\ contact) \end{cases} \qquad (4.8)$$

Since the pre-impact closing velocity v_1 increases with input amplitude, (6) confirms that the input-amplitude to output voltage transfer function has a much smaller slope for a soft contact than a hard contact, allowing the former to affect AM demodulation.
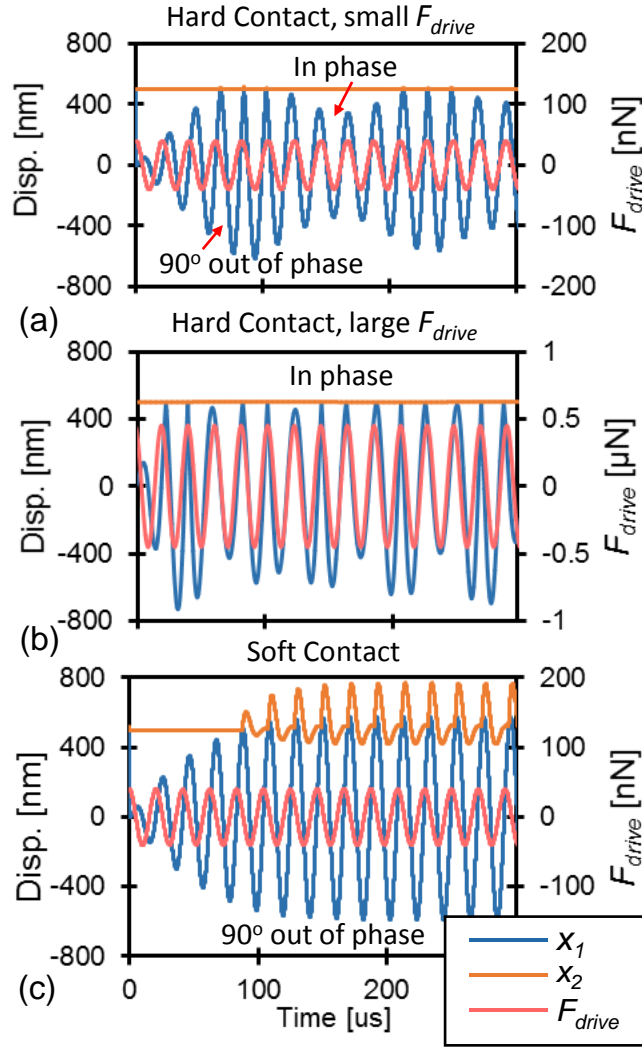
Figure 46: Simulation of transient dynamics of (a) hard-contact with small input force; (b) hard-contact with large input force; and (c) soft-contact.

4.2.2.2 SOFT-CONTACT ENABLED SQUEGGING SUPPRESSION

Another benefit of soft-contact electrodes lies in the suppression of squegging [55], in which impact-derived disturbances to the natural resonance induce fluctuations in resonator displacement amplitude and phase. For more insight, Figure 46 plots simulated displacement over time for several hard-contact and soft-contact scenarios. In each plot, x_1 and x_2 represent displacements of the resonator and the contact electrode, respectively, as labelled in Figure 46.

In Figure 46(a), a small F_{drive} at frequency f_1 drives the shuttle into resonance. Before impact, x_1 is 90° phase-shifted from F_{drive}. When x_1 exceeds x_0, the shuttle makes contact with the (hard) electrode. Each contact induces an abrupt change in the phase of x_1 that renders the resonator out of sync with F_{drive}. This reduces drive efficiency, causing the amplitude of x_1 to decrease, resulting in missed shuttle impacts, as shown. No longer impacting, the phase-shift corrects, the resonator "catches up" to again lag 90° from the drive force, raising the drive efficiency and allowing the displacement amplitude to again increase.

The dynamics depend highly on energy loss mechanisms at impact, which are difficult to model and predict. The resonator often exhibits chaotic behavior [56], where the output voltage is quite unstable. Since there are still impacts, the output capacitive load still charges, but now much more slowly than if the shuttle impacted on every cycle. As a result, the receiver still works, just slower than ideal, i.e., with degraded bit rate.

For the case of a hard contact, restoring a high bit rate calls for more input energy to overcome the described dephasing energy losses, as shown in Figure 46(b), where a much larger input force amplitude compels the shuttle to displace in phase with the drive force, thereby raising the drive efficiency and allowing impact on each cycle. By raising the needed input energy for a high data rate, squegging essentially compromises the sensitivity of a receiver employing a hard-contact resoswitch.

A soft-contact electrode, on the other hand, allows the shuttle velocity to dissipate slowly instead of directly bouncing back and hence reduces the change in phase on each contact, thereby suppressing squegging, as shown in Figure 46(c). Since removal of squegging reduces the input energy needed to impact on every cycle, use of a soft contact electrode also improves the sensitivity at maximum bit rate, as shown in Figure 47, which plots gain characteristics for hard and soft contacts.

CHAPTER 4 ALL-MECHANICAL RECEIVERS

4.2.3 FABRICATION

Figure 48 presents the two-mask fabrication process that achieved soft-contact resoswitches. The process starts with deposition of 2µm LPCVD oxide on a Si substrate, followed by 2µm LPCVD polysilicon, which is subsequently patterned to define the resoswitch structure. 150nm of Ru is then sputtered and patterned by lift-off to leave metal only over 10µm by 10µm areas at the contact points. The sample is slightly tilted at about 15° during sputtering to ensure metal coverage on the sidewalls of the contact areas. A rapid-thermal-anneal (RTA) at 950°C for 3 minutes then forms Ru_xSi_y wherever metal touches silicon, while metal over oxide remains intact. A wet dip in Ru etchant removes the unsilicided metal. The silicidation step preferentially leaves silicide over the contact surfaces, but not on the rest of the structure, allowing for higher Q than if the entire structure were silicided. Finally, a timed etch in 49% HF releases the suspended structure while retaining oxide under anchor areas. Figure 48(a) presents the SEM of a released structure with a zoom-in on the silicide contact.
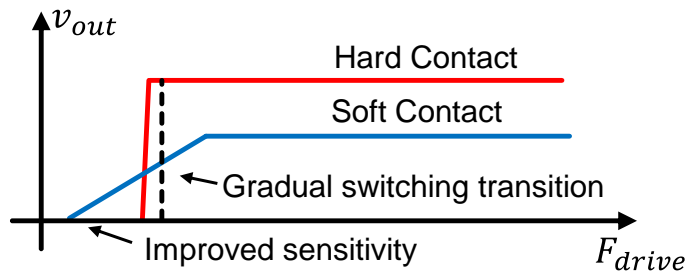

Figure 47: Gain characteristics of hard and soft-contact. Hard contact has instantaneous on/off switching behavior while soft-contact has gradual gain. Soft-contact achieves a lower ultimate voltage and smaller onset switching input due to suppressed squegging.
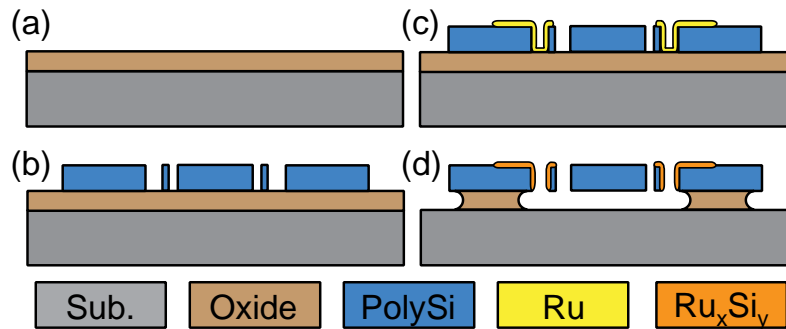

Figure 48: Resoswitch fabrication process.

4.2.4 EXPERIMENTAL RESULTS

Fabricated devices were measured via probing in a Lakeshore FWPX vacuum probe station under 1mTorr pressure. A Tektronix AFG3200 signal generator provided the AM modulated input, while an oscilloscope monitored the receiver output.

Figure 49(b) presents the frequency response of the polysilicon resoswitch with silicide contact measured in vacuum using the circuit in Figure 44(a) with $R_f = 100\text{k}\Omega$. As shown, the measured Q is only 1200, which is 4 times higher than a previous all-metal resoswitch [51], but lower than the tens of thousands normally expected from a polysilicon resonator. One possible cause for this is galvanic reaction between metal and polysilicon during the HF release step that erodes the polysilicon material, attacking grain boundaries and compromising its structural integrity. Although an improved process is desirable, this process again at least improves over previous ones [51].

Figure 50 plots output voltage (or stored charge across C_L) versus input voltage amplitude for three different cantilever stiffness values, with effective gains taken from the slopes. The softer cantilever has the highest gain of 9.8 as well as the highest sensitivity around 60mV, which converts to −68dBm when accounting for the mismatch between the 50Ω signal source and the resoswitch's 11MΩ motional impedance. That the softer cantilever provides the highest gain is consistent with FEA's prediction that contact time decreases with decreasing cantilever stiffness.

Once emplaced into the circuit of Figure 44 with V_P=25V and V_{DD}=5V, the resoswitch becomes a receiver. Since V_P merely charges the input electrode-to-resoswitch capacitive gap, no current flows, so no power is consumed. Upon reception of an out-of-channel input, the resoswitch shuttle does not move, there is no impact, no current drawn from V_{DD}, so still, the receiver consumes no
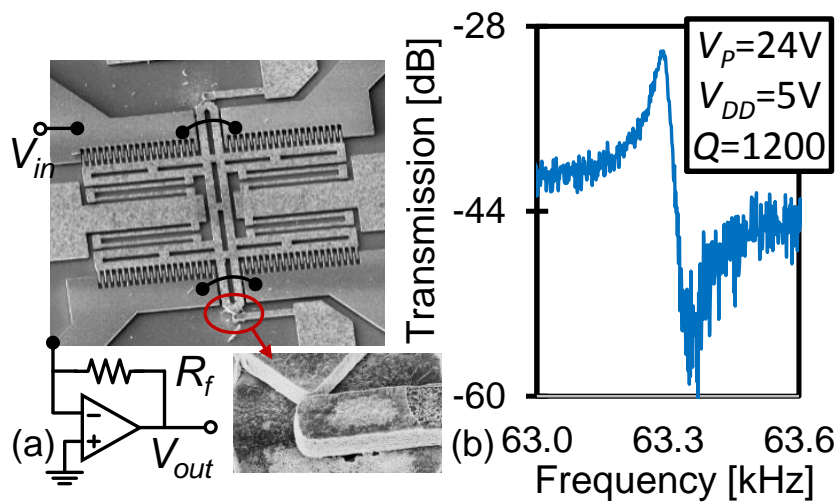
Figure 49: (a) SEM of fabricated poly-silicon resoswitch with Ru-silicided switch tip. (b) Measured transmission spectrum of the resoswitch.

CHAPTER 4 ALL-MECHANICAL RECEIVERS

power, even though it is on and listening. In other words, it consumes zero quiescent power. Only when a valid input in the desired channel is detected does impacting occur, drawing current from V_{DD}, and thereby finally consuming power to follow the envelope of the input waveform, as described earlier.

Figure 51 presents the output waveform response in (b) to a 63-kHz carrier AM input signal shown in (a), clearly demonstrating this device's ability to first select the desired carrier while rejecting out-of-channel interferers, then envelope detect to yield the desired de-modulated waveform.

4.2.5 CONCLUSION

By successfully demodulating 63-kHz AM signal powers as low as −68dBm while consuming zero quiescent power, the demonstrated soft-impact resoswitch receiver aligns to the current WWVB wireless time transfer standard and might soon find use in other ultra-low power wireless synchronizing and updating applications. It further encourages use in higher data-rate
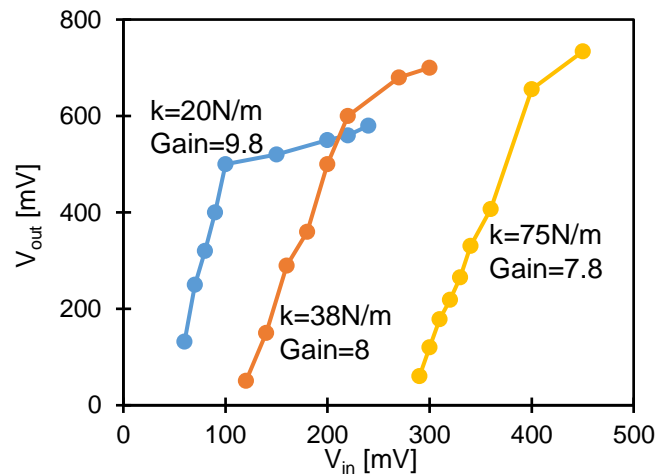
Figure 50: Voltage transfer characteristics delineating the gain of the resoswitch versus soft-impact electrode stiffness.
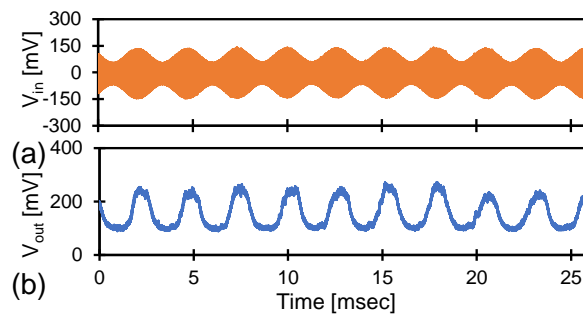
Figure 51:(a) Input AM waveform applied to a soft-impact resoswitch and (b) measured demodulated output.

CHAPTER 4 ALL-MECHANICAL RECEIVERS

constellations, such as the more complex QAM (Quadrature AM). The power savings of this technology is particularly compelling for sensor networks whose sensor nodes must listen for incoming commands at all times, especially those for which sensor placements prohibit battery replacement.

Chapter 5 WIRELESS MECHANICAL CLOCK GENERATOR

5.1 RF- POWERED MECHANICAL CLOCK

A micromechanical circuit has been demonstrated that harnesses resonant mechanical impact switching to convert received RF energy (at −58dBm) into a local 1-kHz clock output while consuming less than 17.5nW of local battery power, which is 57 times lower than the 1μW of a typical real-time clock (RTC). The principal enabler here is a micromechanical resonant switch ("resoswitch") that first accepts incoming ASK or FSK clock-modulated RF energy at a carrier frequency, filters it to remove unwanted interferers, provides power gain via resonant impact switching, and finally envelop detects impact impulses to demodulate and recover the clock waveform from the carrier. Since the resulting time domain waveform derives from the presumably very stable clock signal that originally modulated the RF carrier, the resulting local clock can share its accuracy. By dispensing with the need for a positive feedback sustaining amplifier, such a 1-kHz RF-powered mechanical clock generator driving an *on-chip* inverter gate capacitance of 5fF can potentially operate with only 5pW of battery power, which is 200,000 times lower than the typical RTC! Using an *off-chip* inverter with 17.5pF of effective capacitance, the current laboratory demonstration at 1-kHz consumes a still tiny 17.5nW.

5.1.1 LOW POWER RTC

The widespread expectation that autonomous sensor networks will fuel massively accessible information technology, such as the Internet of Things (IoT) [57], comes with the daunting realization that huge numbers of sensor nodes will be required, perhaps approaching one trillion. Needless to say, besides cost, energy will likely pose a major constraint in such a vision. If sleep/wake strategies can adequately limit a given node's sensor and wireless power consumption, the power bottleneck then comes down to the real-time clock (RTC) that synchronizes sleep/wake cycles. With typical RTC battery consumption on the order of 1μW, a low-cost printed battery with perhaps 1J of energy would last only 11.5 days. On the other hand, if a clock could bleed only 10nW from this battery, it would last 3 years.

CHAPTER 5 WIRELESS MECHANICAL CLOCK GENERATOR

Pursuant to attaining such a clock, this work explores a wireless approach that dispenses with the conventional closed-loop positive feedback approach to realizing an RTC (along with its associated power consumption) and removes the need for a sustaining amplifier altogether. Figure 52 illustrates how such a clocking scheme might work. Here, applications that employ RTC's— which include virtually every electronic device, from phones, to televisions, to appliances—now no longer house positive feedback oscillator RTC's. Rather, RF receiver circuits replace the clocks, while base stations supply the timing waveform remotely. If the carrier frequency used is sufficiently low, transmitted RF clock signals can penetrate buildings and other structures, even into some tunnels. Existing infrastructure, such as AM or FM radio towers, could broadcast clock signals in addition to their usual content. If frequencies are low enough, e.g., WWVB signals already transmitted by NIST in Colorado, then cross-country transmission is even possible.

Of course, receivers for WWVB signals already exist, and unfortunately, they consume 300μW of power when on and listening. This is much more than the 1μW of the typical RTC and is obviously why the proposed Figure 52 clock distribution scheme for everyday electronics is not presently desirable.

To fix this problem, this work explores the use of a MEMS-based RF receiver to eliminate quiescent power consumption and greatly reduce the power needed to recover a clock waveform from a suitable RF input. The clock generator specifically employs a micromechanical resoswitch as a filter-LNA combination [51], pictured and summarized in Figure 53, to first absorb incoming FSK signal energy at its resonance frequency (*cf*. Figure 53 (c)), block other RF components not at resonance, then convert the FSK waveform to a lower frequency clock waveform (*cf*. Figure 53(e)). A final low power inverter then converts the output to a square wave to remove amplitude noise components. Unlike a conventional transistor receiver, this mechanical version consumes no
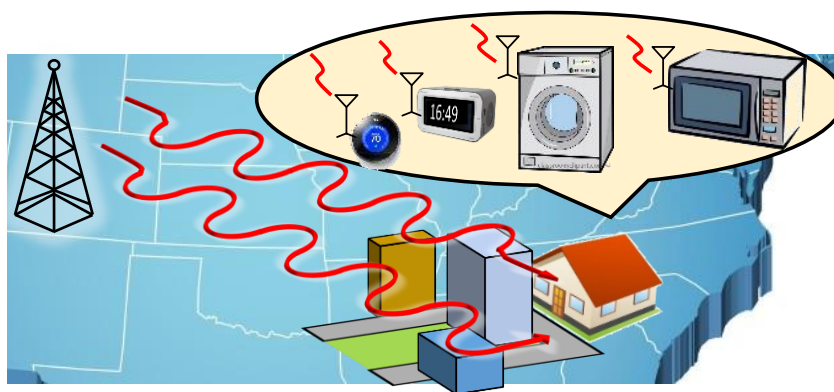
Figure 52: Illustration of a wireless clock vision, where instead of carrying power hungry local clocks based on positive feedback circuits, electronics and appliances receive clock signals remotely via ultra-low power mechanical receivers. As long as their frequencies are low enough, transmitted RF clock carriers can penetrate obstacles and travel over large distances, even cross-country.

CHAPTER 5 WIRELESS MECHANICAL CLOCK GENERATOR

dc power while "listening" for a valid RF clock signal. When it receives the RF clock signal, it then generates the needed clock waveform with considerably less power than otherwise consumed by a positive-feedback RTC sustaining amplifier. The current demonstration using an off-chip inverter with 10pF gate capacitance and 7.5pF internal chip capacitance consumes near zero power (only inverter leakage current) at rest; and only 17.5nW when dynamically switching, which is 57 times lower than a typical RTC.
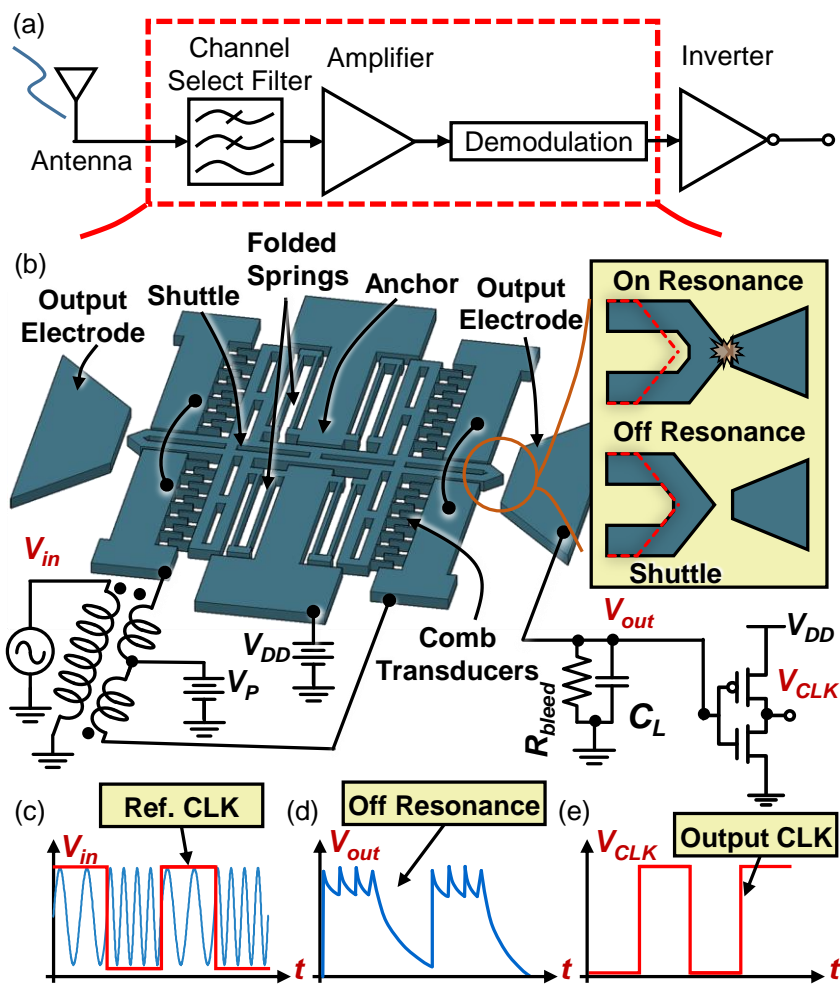
Figure 53: Illustrative summary of the RF-powered clock generator that utilizes a (b) micromechanical resoswitch to realize the receiver functionality of (a). The antenna receives the (c) clock-modulated RF BFSK signal, which the following MEMS resoswitch filters, amplifies, and demodulates to produce a (d) local clock signal. The final inverter shapes the clock waveform to remove amplitude noise components to produce the (e) final output.

CHAPTER 5 WIRELESS MECHANICAL CLOCK GENERATOR

5.1.2 DESIGN AND OPERATION

Again, Figure 53 summarizes the RF-powered clock generator, which comprises an all-mechanical receiver front-end that detects, amplifies, and demodulates clock-modulated RF input power; followed by an optional inverter that converts an otherwise triangle-wave output to a more perfect square wave clock output. The key to low power consumption lies in the use of a micromechanical resoswitch [58] (shown in Figure 53 (b)) that demodulates and amplifies incoming RF energy via nonlinear mechanical impact switching while avoiding the deleterious effects commonly associated with nonlinear operation via high Q channel-selection. Specifically, front-end channel-selection removes unwanted interferers before they can generate spurious signals via interaction with system nonlinearities.

5.1.2.1 RESOSWITCH RECEIVER FRONT-END

The micromechanical resoswitch of Figure 53 (b) comprises a shuttle suspended by four folded-beam springs that ultimately anchor to the substrate at the central locations shown. The shuttle holds two capacitive-comb transducers on each side capable of differentially driving the structure into motion; and two protrusions with pointed tips, also one on each side, capable of impacting with output electrodes when the shuttle displacement exceeds the tip-to-electrode gap spacing. When impacting occurs, the conductive structure periodically closes a switch between the power supply V_{DD} and the output node, delivering power from V_{DD} to C_L and charging it in the process. When impacting stops, the bleed resistor R_{bleed} discharges C_L to 0V.

In the actual envisioned circuit, an antenna picks up the input signal and feeds it to a balun that then generates differential voltages on the drive electrodes, which are also biased at a DC voltage V_P to generate voltage drops of (V_P-V_{DD}) from comb-electrode to shuttle comb finger that amplify the force of any applied AC signal [23]. (Note that no DC current flows between the electrodes and shuttle, so there is no DC power consumption.) If the AC input signal is off the structure's resonance frequency f_o, the shuttle barely moves. If on the other hand it is at resonance, the ensuing shuttle vibration amplitude rises by Q times, yielding for the displacement amplitude

$$x_m = Q \frac{F_{drive}}{k_m} \tag{5.1}$$

where Q is the quality factor of the resonator; k_m is the total stiffness of its suspending beams; and F_{drive} is the drive force exerted on the shuttle generated by the input signal applied to the comb finger transducers. This force takes the form

$$F_{drive} = V_P \left(2 \frac{\partial C}{\partial x} \right) v_{in} \tag{5.2}$$

where v_{in} is the magnitude of the differential input signal voltages at the drive electrodes; and $\partial C/\partial x$ is the change in comb-finger overlap capacitance per displacement for each (identical) capacitive-comb transducer. Once the displacement x_m exceeds the gap between the shuttle and the

output impact electrodes d_o, the shuttle collides with these electrodes in a periodic fashion and connects one output to V_{DD}. Equating x_m with d_o yields the minimum resonance voltage amplitude needed to effect impacting, which takes the form

$$v_{min} = \frac{d_0 k_m}{Q V_P \left(2\frac{\partial C}{\partial x}\right)} \tag{5.3}$$

Converting input voltage to average input power using

$$P_{in} = \frac{v_{in}^2}{2R_x} \tag{5.4}$$

where R_x is the motional resistance of the resonator, given by

$$R_x = \frac{k_m}{2\pi f_0 Q V_P^2 \left(2\frac{\partial C}{\partial x}\right)^2} \tag{5.5}$$

yields for (power) sensitivity S

$$S = \frac{2\pi f_0 k_m d_0^2}{Q} \tag{5.6}$$

Note that since the displacement x_m for an on-resonance input force is Q times larger than for an off-resonance one, the shuttle only makes contact when detecting small RF signals within the resoswitch passband, i.e., at its resonance frequency. Hence, C_L charges only upon reception of an on-resonance RF input, but otherwise discharges to 0V. So effectively, the resoswitch first channel-select filters the input signal, rejecting practically all out-of-band power; amplifies any in-band signal via impact switching to V_{DD}, sending power from V_{DD} to the output; and charges/discharges capacitor C_L according to RF input temporal frequency changes and the bleed rate of R_{bleed}, all of which amounts to FM demodulation. In effect, we have a filter-LNA-demodulator function in one device.

5.1.2.2 CLOCK GENERATOR

Given the above description of resoswitch operation, one input scheme (perhaps transmitted by a base station) that generates the desired square-wave clock output is a simple clock-modulated BFSK signal (Figure 53 (c)) that simply hops back-and-forth between an on-resonance mark frequency f_{mark} (representing a '1') and an off-resonance space frequency f_{space} (representing a '0') with a period corresponding to the desired clock rate f_{CLK}. Here, each time span at f_{mark} induces impacts and charges C_L to V_{DD}; while each at f_{space} stops impacts, allowing C_L to discharge to 0V via bleed resistor R_{bleed}; all resulting in a square wave with amplitude V_{DD} and period governed by the originally modulating source clock. This means the accuracy of the demodulated (local) clock should be practically the same as that of the source clock, which could be extremely good.

CHAPTER 5 WIRELESS MECHANICAL CLOCK GENERATOR

5.1.3 CLOCK STABILITY

Although the received clock signal can be quite accurate, its stability is subject to numerous events. In particular, if the output signal is taken at the V_{out} node indicated in Figure 53 (b), then for a given value of bleed resistance R_{bleed} the output waveform might resemble the sawtooth shown in Figure 53 (d), with fast rise times and slow fall times. Here, consistency of the rising edge of each sawtooth governs to some extent the stability of the local clock.

Presumably, the consistency of the rising edge depends heavily on impact and charging dynamics. For example, if as shown in Figure 54 (a) numerous RF input cycles are required to achieve first impact, then any variance in the drive efficiency that changes the number of cycles to impact would contribute to rise time changes, hence instability. For example, if the drive force amplitude changed for any reason, the number of oscillations needed to instigate impacting could also change, as shown by comparison of Figure 54 (a) and (b). In addition, any variance in electrical contact resistance upon impact will change the charging rate of C_L, hence change the rise time and again generate instability.
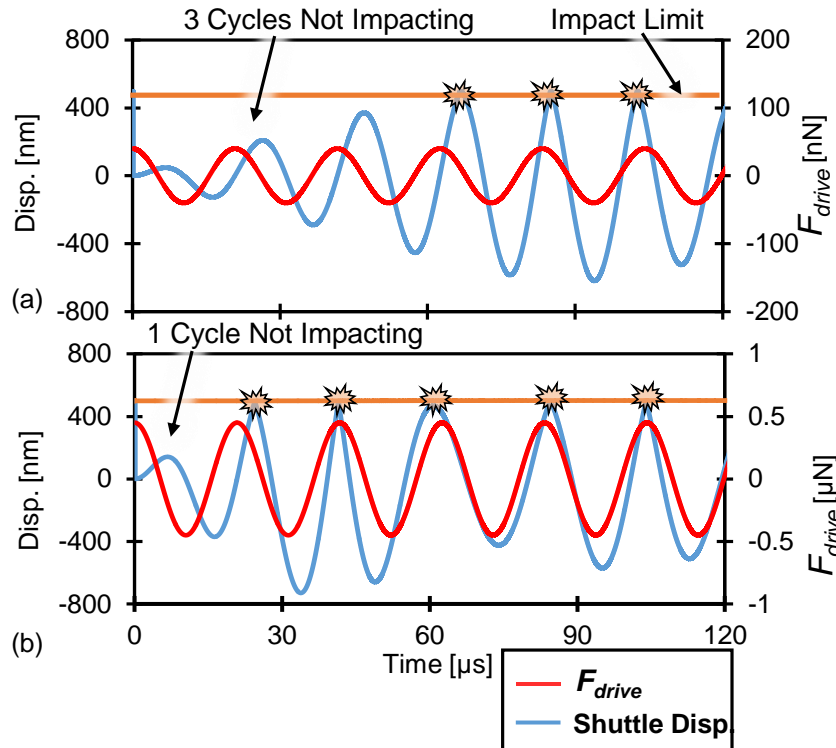

Figure 54: Simulated shuttle displacement (blue) as a function of time in response to (red) (a) a small input force and (b) a larger input force. Here, a larger force allows for fewer input cycles before first impact, i.e., before the displacement meets the gap distance (orange line).

CHAPTER 5 WIRELESS MECHANICAL CLOCK GENERATOR

Perhaps a more important source of instability is squegging, described for resoswitches in [59] and illustrated in Figure 55 where dephasing during collisions reduce the efficiency of the input drive force at resonance, resulting in undue energy loss at certain instances that then lead to missed impacts over small periods. If, as shown later in Figure 59, C_L discharges significantly during the non-impacting periods, the dip in voltage could generate an unexpected fall and rise instance, which could log as an off-frequency cycle that contributes to frequency instability.

More study into the sources of instability and on methods for controlling them will likely be the subject of ongoing research. Meanwhile, one quick way to improve stability is to speed up the rise time in order to reduce amplitude variation around the zero-crossing point of each cycle. The amplification provided by the inverter of Figure 53 following V_{out} and delivering the square-wave V_{CLK} does just this.

5.1.4 POWER CONSUMPTION

The battery (i.e., V_{DD}) power consumption of the clock generator is a strong function of the load capacitance C_L and takes the form

$$P = C_L V_{DD}^2 f_{CLK} \tag{5.7}$$

From equation 5.7, power consumption decreases with reductions in any of C_L, V_{DD}, and/or f_{CLK}. Using equation 5.7 while assuming a typical on-chip inverter gate capacitance of 5fF, the circuit of Figure 53 with $V_{DD} = 1$V and a clock frequency $f_{CLK} = 1$kHz consumes only 5pW. This would last 6,342 years on only 1J of energy!

If on the other hand an off-chip inverter were used with 10pF of gate capacitance and 7.5pF internal chip capacitance during dynamic switching, the power consumption at the same V_{DD} and frequency
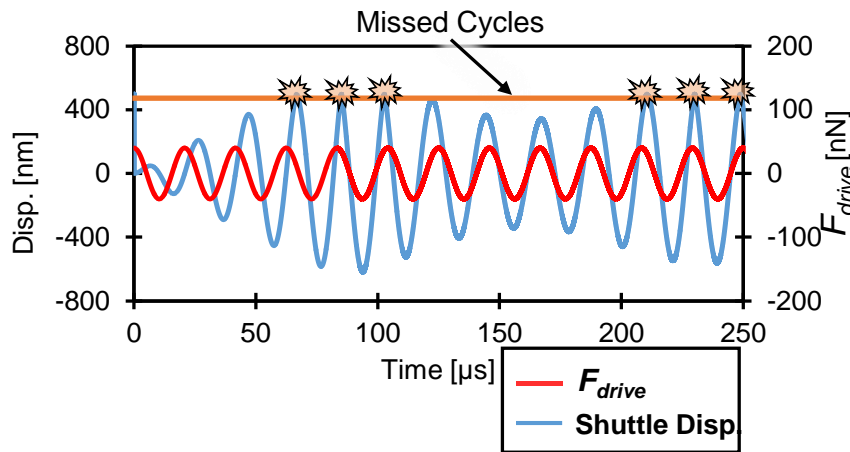
Figure 55: Simulated shuttle displacement (blue) in response to the input force (red) of Figure 54(a) but over a longer time period that reveals squegging.

would be 17.5nW. This would still last a reasonable 1.8 years on 1J. If the clock frequency were reduced to 1 Hz (for a 1 second period), then only 17.5pW would be needed, and the clock would again last quite long on 1J—1,812 years, to be exact.

5.1.5 EXPERIMENTAL RESULTS

Resoswitch clock receiver/generators were fabricated via the one-mask electroplated-gold surface micromachining process first reported in [51] and summarized in Figure 56 and Figure 57 (a) presents the SEM of a released 20-kHz version. For testing, a Lakeshore FWPX probe station provided a 1 mTorr vacuum environment under which resoswitches were characterized, then
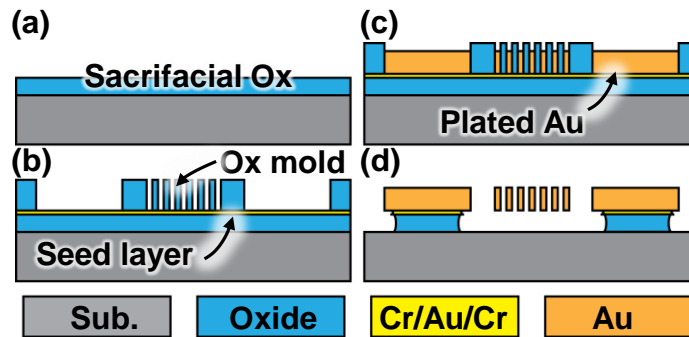
Figure 56: One-mask electroplated gold surface-micromachining fabrication process
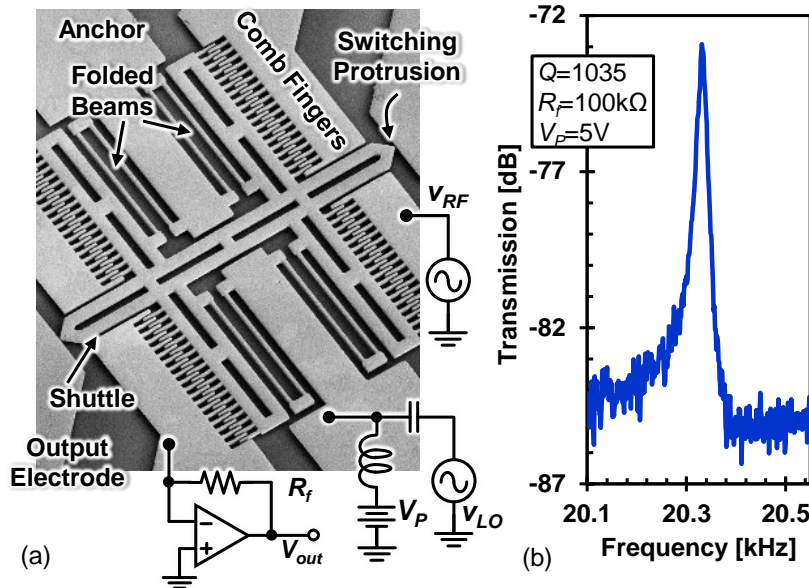
Figure 57: (a) SEM of a released resoswitch with labels and the schematic of the mixing measurement setup. (b) Transmission spectrum of the gold resoswitch measured via mixing and showing a Q of 1,035.

CHAPTER 5 WIRELESS MECHANICAL CLOCK GENERATOR

operated as RF clock receivers. Figure 57 (b) presents the frequency characteristic for a typical gold resoswitch measured using a mixing method [60] to eliminate interference from unwanted parasitic. The measured Q of 1,035 is not nearly as high as the 50,000 normally exhibited by similar devices in polysilicon, but is on par with typical numbers posted by gold structural material.

5.1.5.1 RF CLOCK RECEIVER DEMONSTRATION

To demonstrate RF-powered clock operation, a fabricated resoswitch within the vacuum environment was first hooked into the circuit of Figure 53, and then excited by an HP 33120A
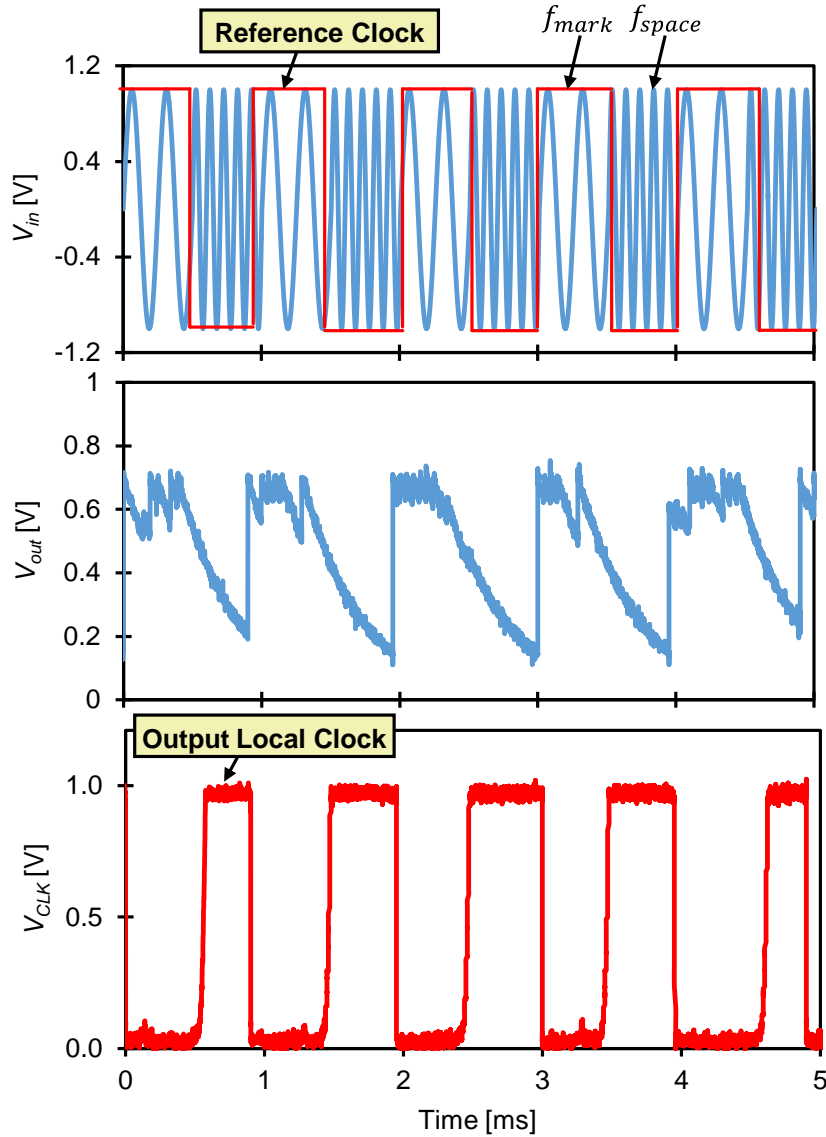
Figure 58: Measured waveforms at various points in the resoswitch clock-receiver circuit of Figure 53 (a) Input FSK waveform; (b) V_{out} at the output electrode of the resoswitch; (c) V_{CLK} at the end of the inverter.

CHAPTER 5 WIRELESS MECHANICAL CLOCK GENERATOR

Waveform Generator providing a clock-modulated BFSK signal with appropriate mark and space frequencies.

Figure 58 presents measured waveforms at various points labeled in the Figure 53 circuit when excited by a clock-modulated BFSK RF signal. As shown, the −58dBm BFSK input signal of (a) with alternating mark and space frequencies of 20kHz and 50kHz, respectively, drives the resoswitch to impacting during the half period when the input is at 20kHz, under which the output voltage shown in (b) rises to V_{DD}. For the following half period of 50kHz, impacts stop and the output voltage discharges to zero.

The waveform of (b) could already serve as a clock signal, and if acceptable, would allow clock generation without need for an output inverter. For more demanding applications, addition of a single inverter provides a cleaner square-wave with less amplitude noise. Figure 58 (c) presents the measured final output clock waveform delivered by a simple off-chip TI SN74AHC inverter, which consumes 7.5nW of battery power, for a total (with C_L charging) of 17.5nW.

Ultimately, the local clock output in Figure 53(c) mimics the modulating source clock waveform of Figure 58 (a), confirming RF-powered local clock generation exactly as prescribed.
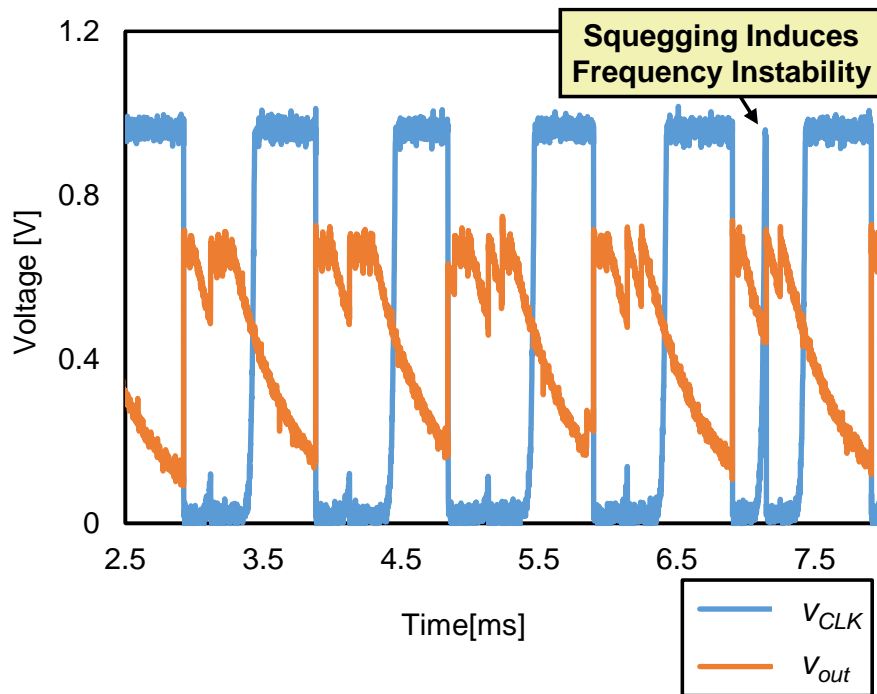
Figure 59: Measured RF-powered clock generator output waveform, showing an instance where squegging generates an undue clock transition, effectively destabilizing the clock frequency.

CHAPTER 5 WIRELESS MECHANICAL CLOCK GENERATOR

5.1.5.2 ALLAN DEVIATION MEASUREMENTS

To gauge the stability of the received and down-converted local clock, Figure 60 presents the preliminary measured Allan deviation for the local clock when excited by an RF BPSK signal modulated by an HP33120A Waveform Generator against that of the reference clock used to modulate the input RF carrier. Clearly, the stability of the local clock signal is poorer than that of the reference clock. This is not unexpected given the stability discussion in the previous section.

To explore the hypothesis of Section 5.1.3 that squegging can contribute to instability, Figure 59 presents an oscilloscope snapshot of a few representative clock cycles at the V_{out} and V_{CLK} nodes of Figure 53. Here, squegging [7] leads to missed impacts every now and then, which then inserts unexpected fall and rise transitions, hence alters the frequency over this instance and compromises clock stability.

To further confirm this squegging-based source of instability, Figure 61(a) and (b) present plots of the local RF-powered clock Allan deviation for varying values of input drive voltage v_{in} and DC-bias V_P. Given that larger drive voltage reduces squegging [59], the improvement in Allan deviation with increasing drive voltage seen in Figure 61(a) does further attest to a squegging-
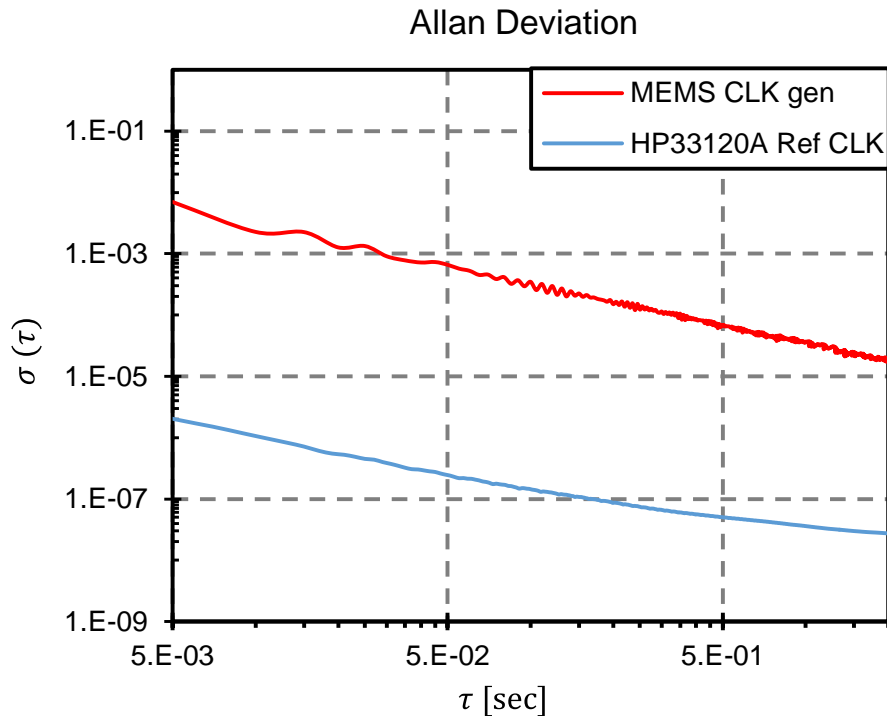
Figure 60: Measured Allan deviation of the RF-powered clock generator alongside that of the reference clock used to modulate the input RF carrier of the HP33120A signal generator.

CHAPTER 5 WIRELESS MECHANICAL CLOCK GENERATOR

based mechanism for instability. The Allan deviation dependence on DC-bias, on the other hand, is less conclusive, although there does seem to be a sweet spot at 8V where Allan deviation is best.

(a)

(b)
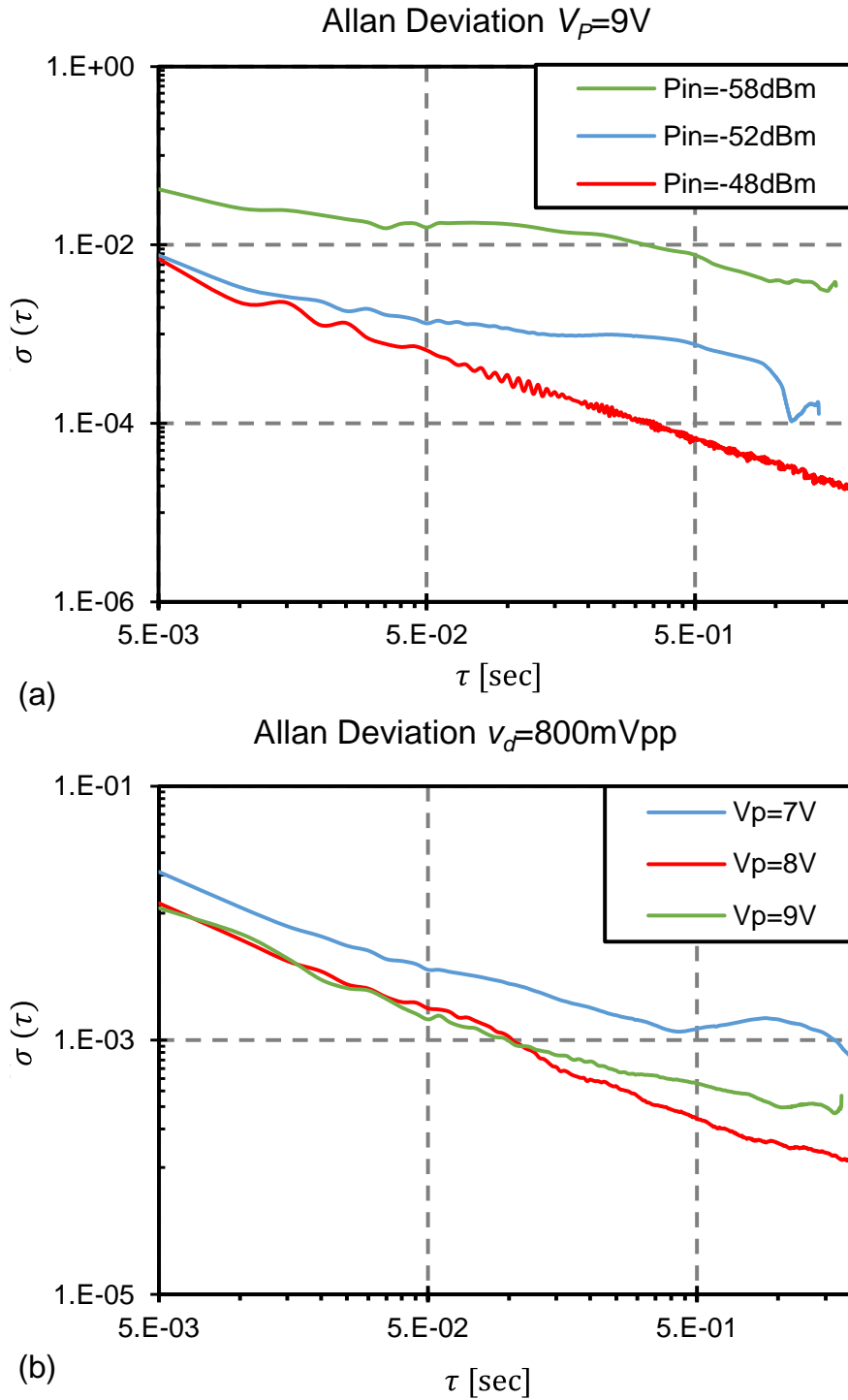
Figure 61: (a) Measured clock generator Allan deviation at various input voltage amplitudes vin while maintaining constant DC-bias V_P at 9V. (b) Measured Allan Deviation of the clock generator at different DC-bias values VP while maintaining a constant drive voltage amplitude v_{in}.

That squegging might be the principal reason for clock instability is actually encouraging, since recent research has identified methods by which squegging can be reduced. These include the use of a symmetric drive (which the Figure 53 device already uses), reduction of the output impact gap [61], and the use of soft or compliant impact electrodes [59]. Work to incorporate these fixes into future resoswitch clock designs is underway that should lead to significant improvements in stability.

5.1.6 CONCLUSIONS

The 17.5nW of battery power used by the demonstrated RF-powered mechanical clock is already 57 times smaller than the typical 1µW RTC. If an on-chip inverter (with much less capacitance) were available, the total dynamic power consumption could potentially drop to only 5pW—15,000 times smaller. Since this power value would allow a 1J printed battery to last more than 6,000 years, battery self-discharge would more likely determine ultimate lifetime.

Although the demonstrated clock shares the accuracy of the modulating source clock, there are sources of instability that compromise the short-term performance of the local generated clock. Among the list of possible destabilizing phenomena, squegging seems to dominate in the demonstrated prototype. That squegging is the main culprit is somewhat encouraging, since it means there is opportunity for improvement, especially given the approaches to reducing resoswitch squegging already in the literature.

5.2 CW INPUT MECHANICAL CLOCK

A mechanical circuit has been demonstrated that harnesses squegging to convert -50dBm of input continuous-wave (CW) energy into a local 1-kHz clock output while consuming three orders less local battery power than a typical real-time clock (RTC). Unlike a previous clock receiver that relied on a modulated RF input, this clock generator converts a CW input—no modulation needed—to a clock output via squegging of an impacting micromechanical resonant switch ("resoswitch"). Here, impact-induced disruption compels the device's resonating element to lose oscillation amplitude (hence stop impacting), then recover to impact again, only to again lose amplitude, in a periodic and repeatable fashion. The resulting time domain waveform, with periodic peaks and valleys, then provides a stable frequency that serves as a local on-board clock for low data rate applications. By dispensing with the need for a positive feedback sustaining amplifier, this CW-powered mechanical clock generator operates with only 0.8nW of battery power when outputting a triangle-wave into 0.8pF, which is 1250× lower than the 1µW of a typical RTC.

CHAPTER 5 WIRELESS MECHANICAL CLOCK GENERATOR

The vast majority of electronics utilize RTCs to keep time for numerous purposes, from time stamping, to computational synchronization, to event synchronization, e.g., simultaneous waking of sensors in a network. Since RTCs generally operate continuously to keep time, it is paramount that they be power efficient, especially when used in battery-operated devices. The typical RTC consumes 1μW of power, which is sufficiently low for devices equipped with coin cell batteries. It is not low enough, however, for the large-scale sensor networks of the future, envisioned by many to employ massive numbers of sensor nodes, each of which must cost very little, so might rely on cheap printed batteries storing only 1J of energy. If such a sensor network uses a sleep/wake
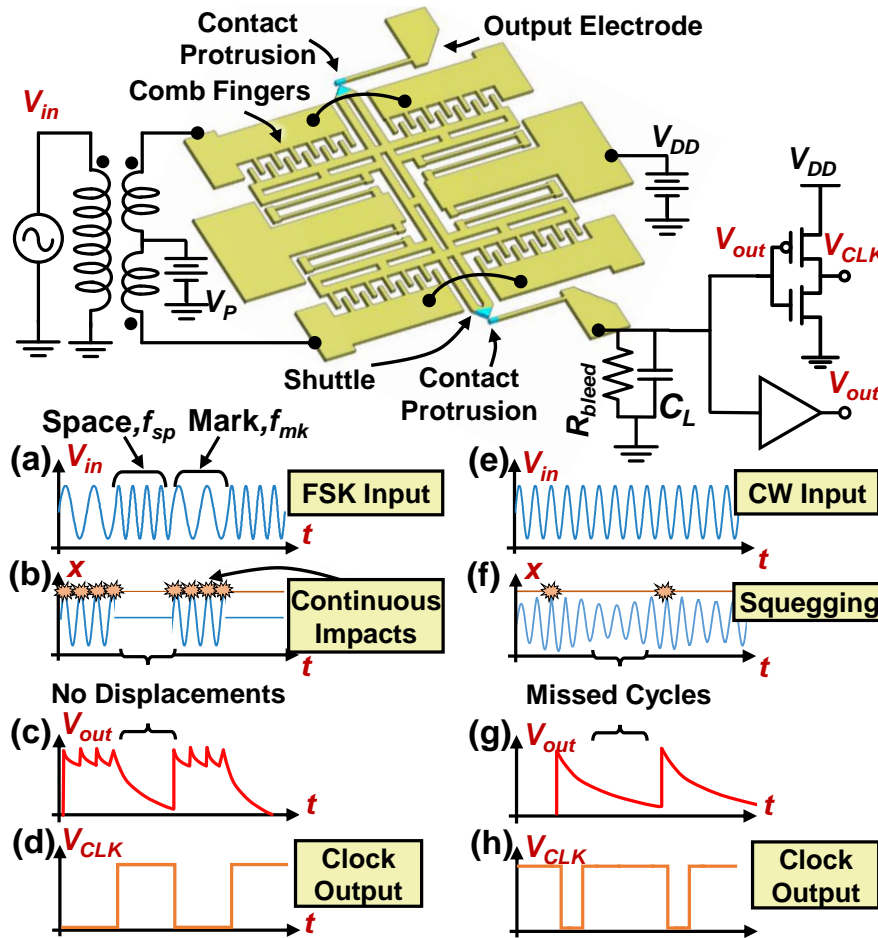
Figure 62: Illustrations summarizing operation of FSK- and CW-powered MEMS clock generators in a typical operating circuit. (a)-(d) summarize FSK-powered operation, where (a) an input FSK signal drives the resoswitch to (b) impact on the mark frequency and not on the space frequency. Rectification by C_L and R_{bleed} then produces the (c) trapezoidal waveform, which an optional inverter converts to (d) a square clock output. (e)-(h) summarize a CW clock generator, where (a) a CW input at resonance drives the resoswitch to (b) squegging, which with rectification produces (c) a rising edge triangle waveform suitable for clock use.

scheme to minimize power, then often the RTCs set the bottleneck on sensor node lifetime. For 1J of energy to last 1 year in a sensor node, its RTC must consume less than 32nW.

To solve this problem, previous work introduced an RF-powered micromechanical clock generator [62] that dispenses with the conventional transistor-based positive feedback oscillator approach to successfully reduce power consumption down to 34nW. As shown in Figure 62, this previous micromechanical clock generator manifests as an all-mechanical receiver [51] that detects and demodulates RF input energy via a resoswitch device [62]. The resoswitch comprises a polysilicon movable shuttle suspended by stress-relieving folded-beams, flanked by capacitive-comb transducers, and employing sharp metal protrusions to impact the indicated output electrodes. Once driven to resonance at a sufficiently large amplitude, the shuttle protrusion impacts the output electrode, closing a switch contact and delivering charge from the supply V_{DD} to the output load capacitor C_L, charging it to V_{DD}. The resoswitch in the previous FSK clock generator operates in an OOK fashion, where a mark input frequency f_{mk} excites resonance impacts to generate voltage spikes at f_{mk} that are rectified by R_{bleed} and C_L to yield a clock "high". Meanwhile, an off-resonance space frequency f_{sp} induces no motion, so no impacts, allowing C_L to discharge via R_{bleed}, generating a clock "low". And all with extremely low power consumption.

One drawback of the previous clock generator is the need for a clock-modulated RF waveform. For example, one target application scenario where all RTCs receive clock activation energy wirelessly would be easier to implement if the energy powering the clocks need not be modulated, i.e., if it could be delivered as a simple continuous-wave (CW) tone. Pursuant to enabling this, the mechanical clock demonstrated here explores the use of squegging to convert -50dBm of input CW energy into a local 1-kHz clock output while consuming only 0.8nW of battery power when outputting a triangle-wave into 0.8pF, which is 1250× lower than the 1µW of a typical RTC.

5.2.1 CW CLOCK GENERATOR

Except for use of a W/TiN contact protrusion metal instead of Au (for reasons to be described), the structure of the CW clock generator mimics that of the previous FSK one. Its operation, on the other hand, is quite different. Instead of functioning as a receiver that faithfully demodulates a received clock signal, the CW clock generator effectively 1) harvests the energy from a remote unmodulated CW input signal; then 2) uses the energy to instigate and facilitate generation of a stable clock signal from a local power source.

The ability to generate a stable clock output derives not from reception of a specific modulated signal, but rather from "squegging" resonance impact dynamics [26]. To explain, Figure 62 illustrates the overall operation of the CW clock generator. As with the FSK-input version summarized in (a)-(d), the CW-input version receives energy via v_{in}, but this time as (e) an unmodulated continuous waveform (that could be wireless) within the response bandwidth of the

shuttle. This input induces a force at resonance, which in turn instigates resonance vibration of the shuttle, with an amplitude that grows until the shuttle impacts the output electrode(s). Upon each impact, current flows from the battery supply V_{DD} to the output load capacitor C_L, quickly charging it to V_{DD}.

At this point, if the shuttle continues to impact the output electrode, C_L remains charged to V_{DD}, which means there is no periodic clock signal. A clock signal, of course, requires that C_L charge and discharge periodically. R_{bleed} in Figure 62 is poised to discharge C_L at a designed "bleed" rate, but only if impacting stops. The present clock generator realizes cessation of impacting by designing the resoswitch to squeg at a specific clock frequency.

Figure 62(f) illustrates the squegging phenomenon where impact-induced disruption compels the device's resonating element to lose oscillation amplitude (hence stop impacting), then recover to impact again, only to again lose amplitude, in a periodic and repeatable fashion. The resulting time domain waveform, with periodic peaks and valleys, then provides a stable frequency that can then serve as a local on-board clock for low data rate applications.

5.2.2 SQUEGGING BY DESIGN

The resonance force response simulations in Figure 63(b) and (c) more fully explain the mechanism behind squegging by comparison with the non-impacting (so non-squegged) case in
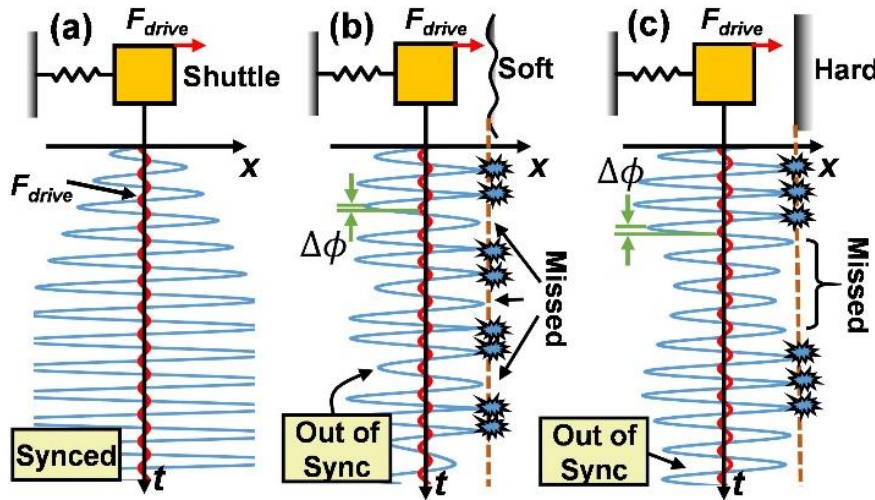
Figure 63: Simulated transient waveforms showing (a) no impacts, (b) small phase shifts $\Delta\varphi$ for soft impacts, and (c) large $\Delta\varphi$ for harder impacts. Here, phase shifts pull the resoswitch out of sync with the drive force, reducing its efficiency and thereby causing squegging where no impacts occur over the next few cycles until the structure re-synchronizes with the input force and recovers to impact once again.

CHAPTER 5 WIRELESS MECHANICAL CLOCK GENERATOR

(a). With no impacts, the amplitude of the resonant structure grows until limited by (gentle) loss, at which point it reaches steady-state vibration, where its displacement phase lags that of the input excitation force by 90º. In contrast, when a nearby electrode limits the displacement amplitude, energy absorption upon contact imposes a phase delay $\Delta\varphi$ on shuttle bounce-back, which then lowers the efficiency of the input drive, resulting in a smaller subsequent amplitude in the next cycle [42]. The amount of phase shift, and thus number of missed cycles, depends strongly on the hardness of the contact: For the case of a soft contact, as in (b), $\Delta\varphi$ is small, so very few cycles miss, and very little squegging ensues. A hard contact, on the hand, depicted in (c), imposes much larger dephasing that results in many missed cycles, giving R_{bleed} enough time to discharge C_L. Again, the resoswitch of the present CW clock generator differs from that of the previous FSK one in its use of a harder W/TiN contact interface, which enhances squegging. Ultimately, the system recovers to a state where the displacement is again 90º phase-shifted from the input force, raising the drive force efficiency to grow the displacement amplitude to again impact, after which the cycle repeats. The stability of the cycle determines the ultimate stability of the clock.

As described in [42], there are numerous knobs by which squegging and its periodicity can be controlled, including gap distance, drive symmetry, Q, contact hardness (as governed by contact interface materials), and drive strength. Inevitably, each of these knobs governs the squegging period by influencing contact dynamics.

To address contact dynamics, consider that before making contact with the electrode, the resonator experiences only the drive force F_{drive}. Upon impact, the impacting electrode applies a counteracting contact force F_c on the resonator to prevent it from penetrating into the electrode. The relevant equations are:

$$F_c = k_x(x_1 - x_0) \tag{5.8}$$
$$m_1\ddot{x}_1 + b\dot{x}_1 + kx_1 = F_{drive} \ (x_1 < x_0) \tag{5.9}$$
$$m_1\ddot{x}_1 + b\dot{x}_1 + kx_1 = F_{drive} - F_c \ (x_1 \geq x_0) \tag{5.10}$$

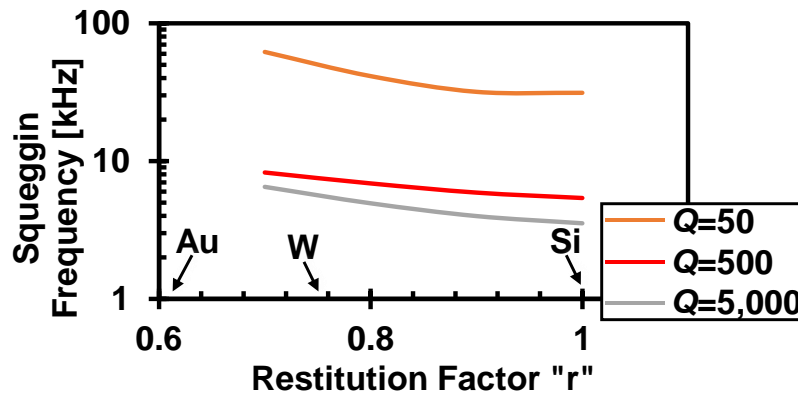Figure 64: Plots showing how electrode hardness ("r"factor) and system Q influence squegging frequency.

where x_1, m_1, k and b are the displacement, equivalent mass, stiffness and damping factor of the resonator, respectively. x_0 is the initial spacing between the resonator and the output electrode, i.e., the displacement threshold to be overcome before the resonator shuttle makes initial contact.

The contact force is a product of the penetration depth and the contact stiffness k_c, the latter of which increases with penetration depth. For the specific design here, the hard surface of the W/TiN contact material dictates very shallow penetration, which means k_c is approximately constant over the period of contact. However, since the value of k_c depends on many other factors, such as the contact velocity v_1, the surface roughness, and the mechanical stiffness of the electrode [63], it often takes the form of a fitting factor to satisfy the penetration tolerance [30].

Pursuant to facilitating study of how impacts influence the squegging frequency, one can introduce a post impact shuttle velocity v_1', defined as [64] [65] $v_1' = r v_1$ where r is a coefficient of restitution [65] that captures impact conditions and that increases with increasing hardness. A positive r means the impact does not invert the direction of the resonator's velocity, which means the resonator suffers a smaller phase setback $\Delta\varphi$ than impacting with a negative r factor. After each impact at time t_n, the initial conditions of differential equations change to:

$$x_1(t_n) = x_0 \tag{5.11}$$
$$v_1(t_n^-) = r v_1(t_n^+) \tag{5.12}$$

where t_n^- and t_n^+ are the times before and after the nth impact at t_n, respectively. The effect of these initial conditions fade out as $e^{-\left(\frac{\omega}{2Q}t\right)}$, which means the displacement phase lag recovers with a time constant $\tau \sim 2Q/\omega$. Thus, the higher the Q, the longer it takes to recover, the more missed impacts, the longer the discharging period, and the lower the output squegging frequency. Figure 64 simulates squegging frequency as a function of r for different Qs.

5.2.3 MATERIAL DESIGN AND FABRICATION

Given its time-keeping function, the frequency of the CW clock generator should be low, which suggests its resonator element have high Q and its contact interface be hard. To insure high resonant Q, the resoswitch for CW clock generation uses polysilicon structural material to set elastic properties, while employing hard W/TiN metal (for long missed impact periods) only in areas where impacting contacts occur.

 Figure 65 presents the fabrication process flow. The process starts with a 4µm LPCVD of sacrificial oxide followed by lithographic patterning using a negative structure mask and a timed etch to remove 2 µm of the oxide, leaving a mold (*cf.* Figure 65(a)) to shape a subsequent *in situ* phosphorous-doped polysilicon deposition to the desired structural geometry. Next, CMP planarizes the surface leaving the polysilicon flush with the oxide mold (*cf.* Figure 65(b)). This facilitates subsequent formation of metal impact contacts, for which 150nm of W followed by

CHAPTER 5 WIRELESS MECHANICAL CLOCK GENERATOR

20nm of TiN are sputtered and etched to the contact protrusion geometries, which cover only areas near the contact points. The majority of the resonator structure, especially its folded-beam supports, remain metal free, so retain their very high Q.

The metal etch recipe comprises two steps: first, an SF_6 plasma etch to cut through the TiN protective layer above W; then, a wet etch in H_2O_2 solution using the TiN as a mask to remove the remaining W. The wet etch leaves the polysilicon beneath intact, preserving its Q. Finally, a timed wet etch in 49% HF with galvanic corrosion-suppressing anti-oxidant releases the structure while leaving the anchor areas attached to the substrate (*cf.* Figure 65(d)). Note that it is actually the portions of W/TiN protruding beyond the polysilicon edges that actually make switch contact. Figure 66(a) shows a scanning-electron micrograph (SEM) of the released structure.
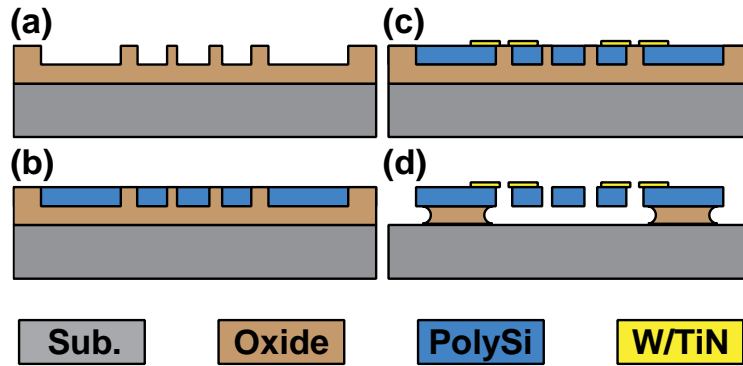

Figure 65: Figure 4: Fabrication process flow for the polysilicon resoswitch with W/TiN contact tips.
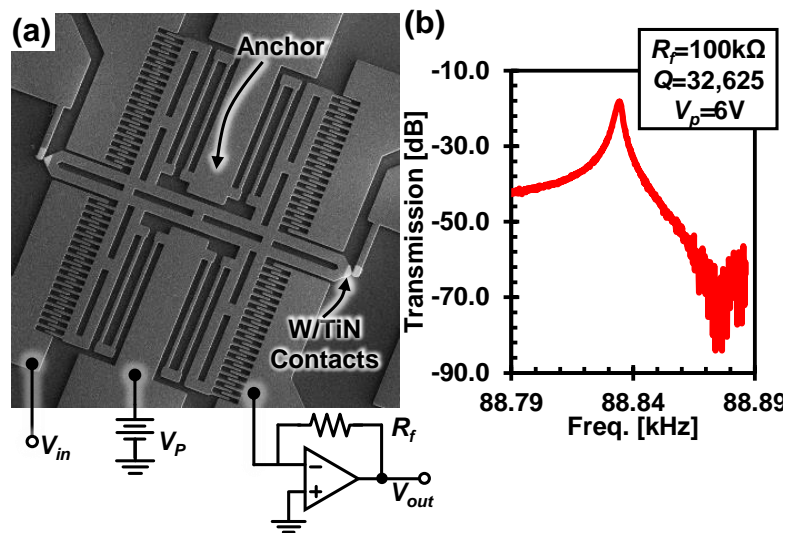
Figure 66: (a): SEM of a fabricated CW-powered clock generator resoswitch with W/TiN contacts. (b): 100µTorr-measured non-impacting frequency spectrum for the device.

5.2.4 EXPERIMENTAL RESULTS

The fabricated resoswitches were wirebonded onto a printed circuit board (PCB) and emplaced into a custom-built bell jar to provide a 100μTorr vacuum test environment and allow SMA connection to external test instrumentation that include voltage sources and an oscilloscope. Figure 66(b) presents the measured frequency response of a non-impacting resoswitch, showing a vacuum-Q of 32,625, which is 23× higher than the previous resoswitch of [63], enabled largely by the use of anti-oxidant during HF release.

Figure 67 presents measured waveforms at various points labeled in the Figure 62 circuit. As shown, the -50dBm CW input signal of (a) drives the resoswitch to impacting, but with squegged behavior, where impacts do not occur on all cycles, as indicated by the varying amplitudes in Figure 62(b) and (c). Thus, impact-based charging of the output capacitor C_L occurs only at the beginning of a squegging cycle, after which C_L discharges through bleed resistor R_{bleed}, inevitably

Figure 67: Measured waveforms for the CW-powered MEMS clock depicted in Fig.1. (a) Input CW waveform v_{in} at the resoswitch resonance frequency. (b) Squegged raw output waveform v_{out} across load capacitor C_L. (c) V_{CLK} at the output of the optional inverter.

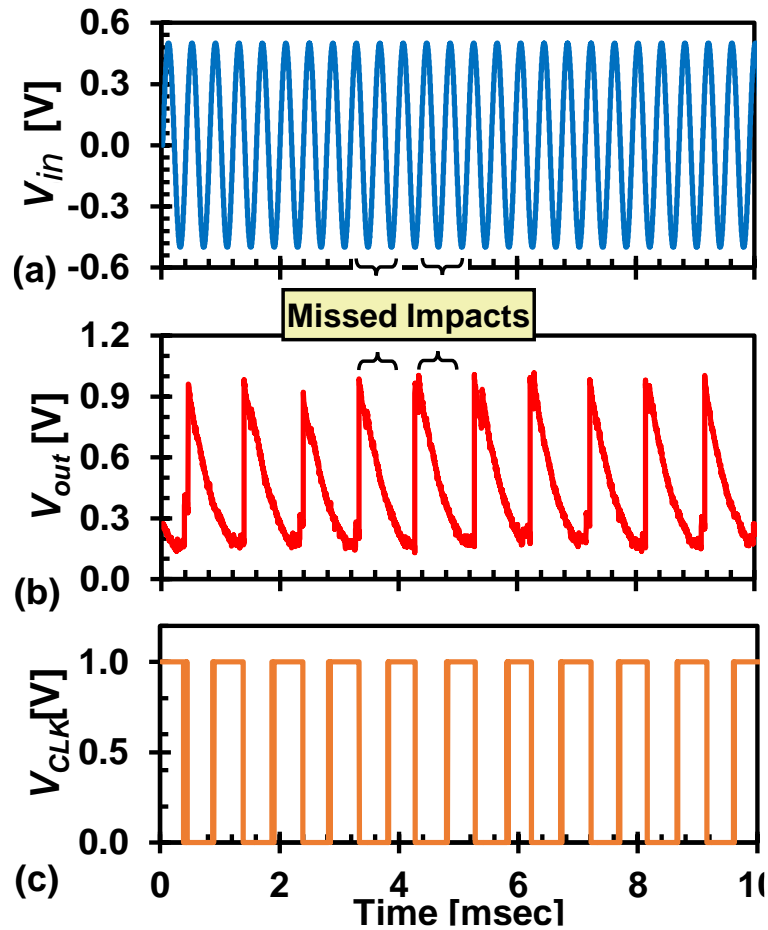generating the triangle waveform shown with a frequency of 1kHz determined by resoswitch design.

To characterize the stability of the clock, Figure 68 presents the measured Allan deviation for the triangle waveform of Figure 68(b) that reaches 10^{-3}. This is stable enough for low-end commercial applications, such as timers for washing machines and low data rate wireless sensors. Addition of a single inverter provides a cleaner square-wave signal (*cf.* (c)), but is actually not needed for rising edge-triggered systems.

In Figure 62, the output node of the resoswitch connects via wirebonds to two separate following stages: a buffer (Texas Instruments THS4271) that feeds the oscilloscope; and an inverter that produces the square wave clock output. The total capacitive load presented to the resoswitch output thus combines 0.8pF of buffer input capacitance, 10pF of inverter input capacitance, and 7.5pF of internal chip capacitance, for a total of 18.3pF. With V_{DD} of 1V and clock frequency f_{CLK} of 1kHz, the total power consumption is 18.3nW. Without the inverter, when outputting a triangle wave into only the 0.8pF input capacitance of the buffer, the clock only consumes 0.8nW, which is 1250 times lower than the 1μW of a typical RTC!

5.2.5 CONCLUSION

With its ability to use energy from a simple CW wave, with no modulation required, the demonstrated mechanical CW clock generator potentially enables scenarios where even the simplest inexpensive products, e.g., toys, paper, can benefit from an embedded clock that might be key to smart operation as long as CW energy is available. Considering that radio signals are everywhere, even in remote areas (e.g., WWVB, AM), the prospects of this technology making available clocks that can permeate simple products is not as outlandish as one might think at first glance. Still, there is much work to be done to improve the stability and accuracy of this clock,
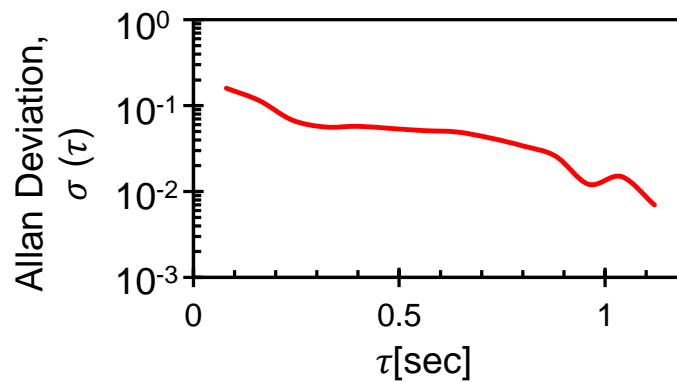
Figure 68: Measured Allan deviation for the resoswitch clock generator powered by a −50dBm CW resonance input.

especially against changing environmental conditions. Improved modeling and understanding of squegging has already uncovered promising solutions to these problems that make for some interesting research ahead.

Chapter 6 HIGH FREQUENCY RECEIVERS

The all-mechanical receiver at VLF frequency that timing transfer is already using, but it is limited to the VLF infrastructure in NIST. Existing large-scale infrastructure at LF such as AM stations covers a wide area and has the potential to sustain trillion sensor networks. AM signals are above 50MHz, therefore the all-mechanical receivers require resoswitch devices with resonance frequencies of 50MHz. Comb-driven structures are too compliant to effectively reach 50MHz while micromechanical beams of sizes within microfabrication limits fall around 50MHz range. This chapter describes the challenges in design, fabrication and measurement of beam resoswitches.

6.1 ELECTROMECHANICAL BEAM RESOSWITCH PROCESS DESIGN

The main process challenge for beam style resoswitch is the switching gap. Due the lack of complaint folding support, the beam devices are usually much stiffer; therefore they have higher resonance frequency. However, as a resoswitch, high stiffness structures move less and takes larger input to make contact. To compensate for higher stiffness, the switch gap has to scale accordingly. The lithography defined switch gaps in comb-driven devices are limited to the order of hundreds of nanometers. The beam devices have around 10X the stiffness, so the switch gaps need to shrink to tens of nanometers. Sacrificial gaps are tens of nanometer wide but complicate the process especially when the contact material needs to be metal. To maintain high quality factors, the polysilicon resonator has to be deposited on top of the metal contact for a vertically actuated free-free beam. Thus, the contact metal has to be one of the refractive metal that are compatible with high temperature polysilicon process. In this work, W first served as the main contact material. Figure 69 shows the process flow of a free-free beam whose contacts are W.

Free-free beams' mode shape dictates that the displacement at the switching tip is 1.6 times larger than the center where the capacitive transduction drives the resonator. Therefore, if the gap spacing is uniform across the resonator, the switching only occurs at the tips of the beam. Sensitivity of

the resoswitch depends inversely on the switch gap as demonstrated in Chapter 2. To decrease the gap spacing, thinner oxide sacrificial is necessary.

The following sections describes several experiments on thin sacrificial oxides.

6.1.1 Attempts to Achieve Thin Sacrificial Gap

Due to the limited thermal budget, Low Temperature Oxide (LTO) is the first candidate for oxide deposition over W. The deposition went smoothly, but uniformity decreases dramatically when deposition time reduces to a few minutes. The LPCVD process takes time to stabilize and condition
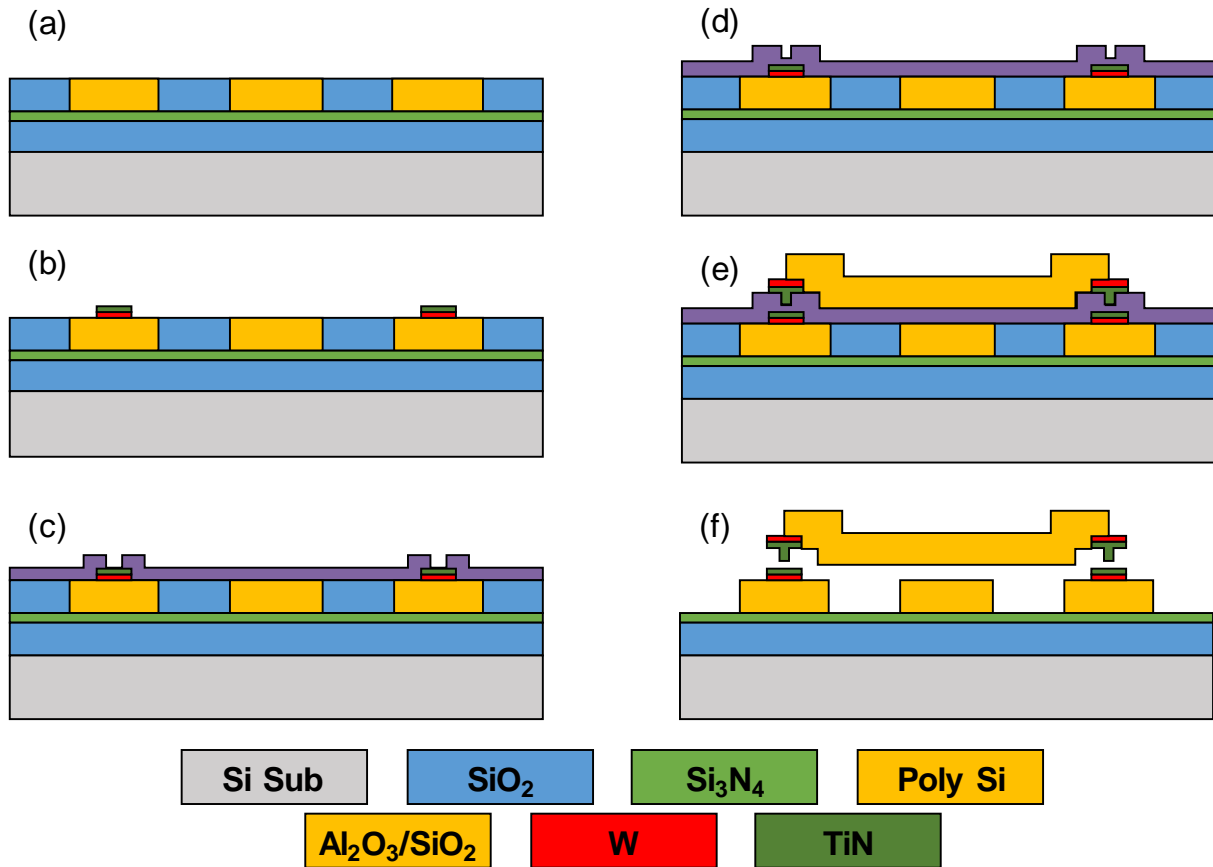
Figure 69: The process flow of a polySi free-free beam with metal contacts. (a): Starting from 2μm of isolation oxide followed by 300nm of silicon rich nitride, the polySi interconnect is deposited and etched on top of nitride. To remove the topography, LPCVD oxide is deposited and cmped flush with the interconnect surface. (b): At the contact point, W/TiN are sputtered and etched to form contact patches on the interconnect electrodes. (c): ALD first half of Al2O3 sacrificial thickness and etch dimples on the contact patches. (d): Deposit the second half of the Al2O3 sacrificial over the dimples. (e): Deposit and etch another W/TiN layer into top contact patches. Then etch the anchors of the beams. After this, continue to deposit and etch the polySi structures stopping on the sacrificial Al2O3 and on the contact patches. (f): Release the beam structure.

CHAPTER 6 HIGH FREQUENCY RECEIVERS

the surface of the wafer in the beginning of the process [66] [67], too short a process is not a reliable enough to produce a good quality uniform sacrificial film, which results in device shorting after release.

A higher quality oxide High Temperature Oxide (HTO) has slower deposition rate and generally has better uniform. However, the standard deposition temperature is 930°C. The melting point of W is well above 1100°C, but exposure to process gases such as SiH_4 and N_2O at above 900°C can create substantial stress that causes W delamination from the bottom electrode underneath [68]. Figure 70 shows the bubbles of W after HTO deposition at 930°C.

To minimize W delamination, HTO process was tested at various lower temperature. The gas flow and process pressure were also parameters to tune for a balanced deposition rate and uniformity across the wafer. Temperature plays an important role in film quality and uniformity. Limited thermal budget reduces the quality of the oxide film which manifests as low etch selectivity and non-uniformity. Figure 71 shows the result of etching metal 2 stopping on oxide layer in the field. Table 1 lists the measurement selectivity over metal etch of the HTO film comparing to the numbers reported in literature. The oxide surface became very rough, which implies that some areas could have too thin an oxide layer that subsequent polysilicon structure would be shorted to the electrode underneath the oxide. The final devices have very low yield due to shorting. Figure 71 shows the SEM of the released beam devices using HTO as sacrificial.
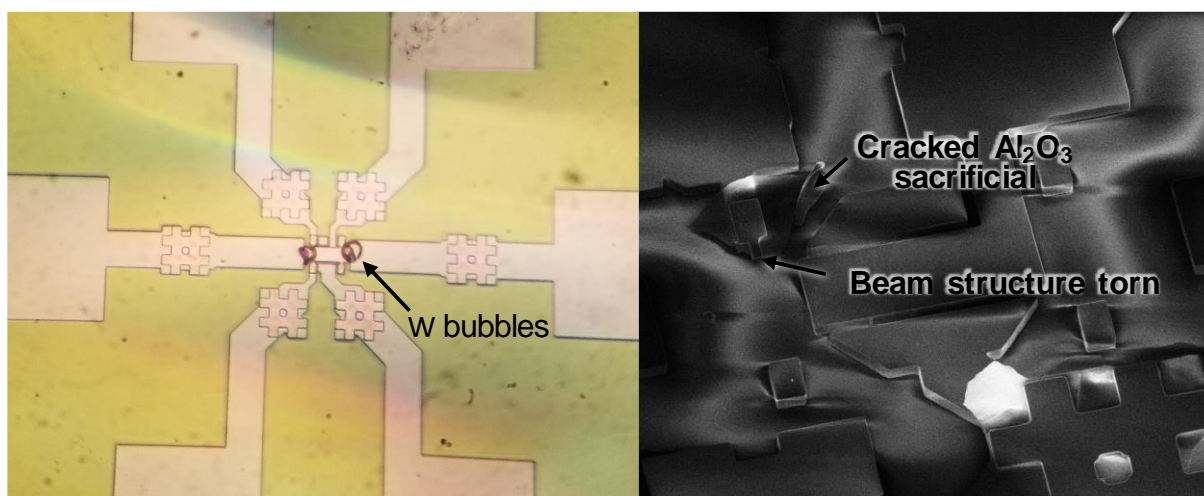

Figure 70: (Left): A microscopic image of the W bubbles formed after polySi structure deposition. W bubbles form at the metal contact patch area. (Right): High temperature annealing of polySi changes the behavior of Al2O3. The SEM shows that Al2O3 sacrificial does not dissolve after 30mins in 49% HF, but rather cracks into pieces and tear off the beam structure above it.

CHAPTER 6 HIGH FREQUENCY RECEIVERS

Another method for depositing conformal, uniform and thin sacrificial material is ALD. The most common ALD material is Al_2O_3, which should have high thermal tolerance and dissolve in HF, the releasing solution. Additionally, Al_2O_3 is much more resistant to chemical and physical etching, which makes steps (b) and (e) in this process more controllable. Figure 71 shows the comparison of the etch result in step (e) of HTO sacrificial process and Al_2O_3 sacrificial process. The HTO shows visible roughness due to chemical and physical erosion in RIE process to etch metal 2 layer.

The Al_2O_3 process went smoothly until the structural polysilicon deposition step. There are two common ways to obtain doped polysilicon. One is deposit in-situ doped polysilicon. During deposition, PH_3 mixes with SiH_4 to introduce P dopants as polysilicon is deposited on the wafer. The second method is to deposit undoped polysilicon and then grow PSG on polysilicon followed by annealing in $POCl_3$ rich environment at high temperature. To achieve low resistance and minimize stress, both methods require high temperature anneal. For in-situ doped polysilicon, the deposition itself occurs at $615^{o}C$, but the resulting films contains a large stress gradient and has high sheet resistance. After annealing the polysilicon to $700^{o}C$, $800\ ^{o}C$ and $850\ ^{o}C$, the stress gradient reduces, as shown in Figure 71. The sheet resistance also drops dramatically. However, W bubbles start to appear in areas where there are large continuous patches of W after annealing at $850^{o}C$. The $POCl_3$ method also requires high temperature for dopants from PSG to diffuse into polysilicon. In summary, polysilicon structures require process temperature of above $850\ ^{o}C$.
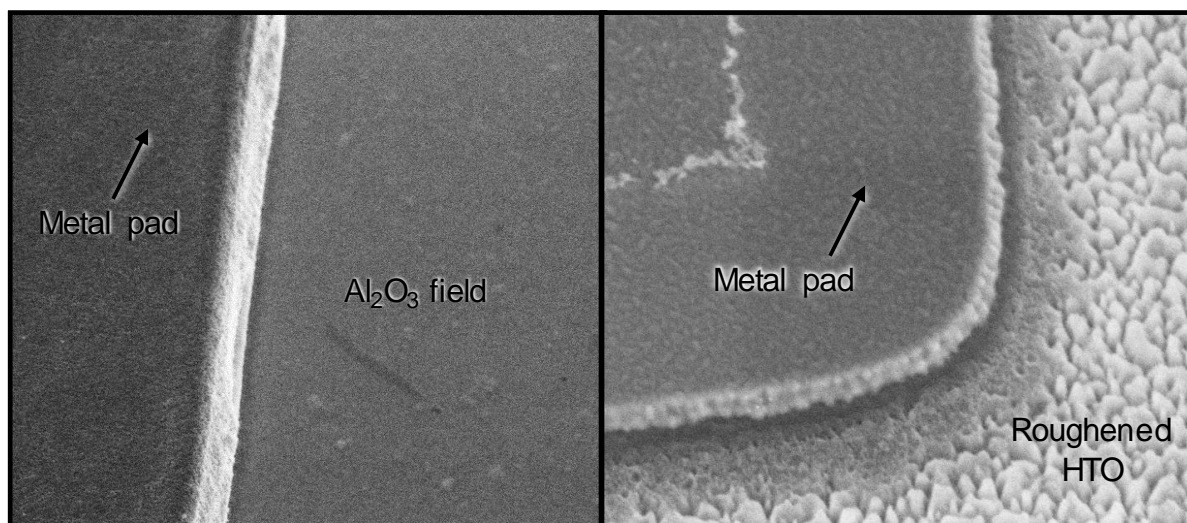

Figure 71: (Left): Metal etch stops on Al_2O_3 in the field. The over etch does not cause any visual damage to Al_2O_3. (Right): The same metal etch recipe stops on HTO in the field. The etch causes cracks and roughens the field oxide. The cracks and rough surface might lead to shorting of the beam structure to interconnect.

Al_2O_3 supposed to withstand temperature of more than 900 $^{\circ}$C [69]. However, after annealing to 850°C, the Al_2O_3 no longer dissolves in HF. Rather, it cracked into pieces. Various solutions were tested to remove the annealed Al_2O_3, including piranha, RCA solution, Al etchant, but none was successful. Figure 71 shows the cracked Al_2O_3 after release.

For lower temperature than 850 $^{\circ}$C, the sacrificial Al_2O_3 is easily etched away in HF, but the stress gradient in polysilicon is not completely relieved, which causes shorting. Laser blasts introduce energy locally to heat up the resonator, thus relax the stress gradient, and help activate dopants. Although laser shots can sometimes be destructive, controlled laser shots before release help resolve the resonator shorting issue. Figure 71 shows the measured frequency response of the resonator.

6.1.2 SWITCH DIMPLES

Dimples at switch contacts reduce contact area and reduce contact stiction [70] [71]. In this process, introducing dimples also help further reduce the switch gap spacing, improving sensitivity. Dimples require splitting the deposition of the sacrificial oxide layer into two steps, as shown in Figure 71. The first step deposits half of the total thickness, and then a dimple mask is used to etch a couple of dimple holes at the tips of the beams. Figure 71 shows the SEM of the etched dimples. At last, the second deposition step fills the dimple holes with only the second half of the sacrificial while the rest of the beams have the full sacrificial thickness.
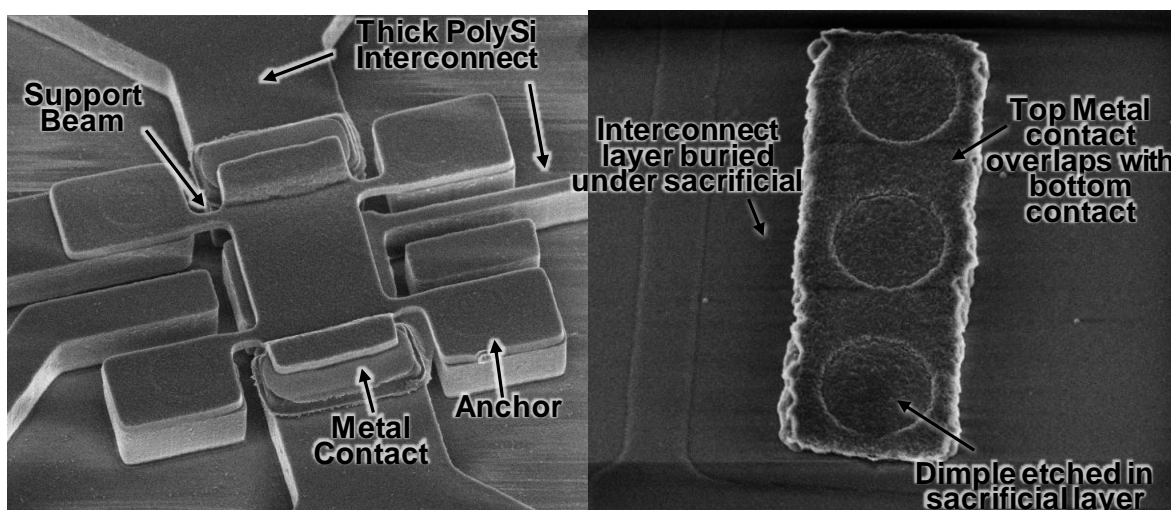

Figure 72: (Left): The SEM of a released free-free polySi beam with metal contacts. (Right): A zoomed in view of the top metal contacts before the deposition of the polySi structure.

CHAPTER 6 HIGH FREQUENCY RECEIVERS

Al$_2$O$_3$ ALD deposition is self-exclusive that allows the film to be thin but conformal. The nucleation of the first layer of Al$_2$O$_3$ is very critical, which is highly dependent on the surface that Al$_2$O$_3$ is deposited onto [72]. In this process, Al$_2$O$_3$ is deposited onto areas of W, polysilicon and oxide. Several trial depositions result in inconclusive answers, as some attempts were successful while other failed, despite following the same sample preparation routine. To improve the reliability of the ALD process, W has TiN on top that is a known ALD friendly material [73].

However, the addition of the TiN layer complicates the etching process. TiN is more inert and thus harder to etch away. The dry etch of the TiN uses Cl based chemistry and higher power than what is needed to etch W, which means worse selectivity over oxide. If continue to use high power recipe to etch W after etching TiN, oxide might not withstand the overetch and expose the polysilicon electrode underneath. The metal etch recipe usually eats away silicon at a way faster rate than metal. The TiN coating is thin enough for wet etching but the etching solution for TiN is RCA2 which an excellent photoresist remover. In the end, the easiest solution available is to do a timed dry etch that removes the TiN and then finishes off the W using wet etch in H$_2$O$_2$. The DUV photoresist is delaminates in H$_2$O$_2$ and affects the wet etch uniformity, so the photoresist needs to be stripped before the wet etch in H$_2$O$_2$. Figure 69 shows the process flow with TiN/W stack.

6.2 FREE-FREE BEAM RESOSWITCH DESIGN

The design of the free-free resoswitch follows the classic capacitive transducer theories and design procedures [74]. The mode shape of the free-free beam of interest shown in Figure 73 takes the form:

$$Z_{mode}(y) = cosh\phi y + cos\phi y - \xi(sinh\phi y + sin\phi y) \tag{6.1}$$

where $\xi = \frac{cosh\phi L_r - cos\phi L_r}{sinh\phi L_r - sin\phi L_r}$ and $\phi^4 = \frac{12\rho A}{EW_r h^3}$. W_r, h and A are the width, the thickness and the cross section area of the beam respectively. ρ is the density and E is Young's Modulus.

As resoswitch, the sensitivity is of specific interest, which is the minimum required input voltage v_{in} to produce displacement g_{switch}.

The corresponding displacement across the beam due to the actuation voltage v_i and the bias voltage V_P is expressed as [75]:

$$x(y) = V_P v_i \epsilon W_r \int_{L_1}^{L_2} \frac{1}{k_r(y')g^2} \left(\frac{Z_{mode}(y)}{Z_{mode}(y')}\right) dy' = \frac{V_P v_i Q \epsilon W_r}{g^2} 2.9964 \tag{6.2}$$

where $k_r(y)$ is the stiffness of the beam referred to location y. g is the actuation gap between the beam resonator and the drive electrode.

CHAPTER 6 HIGH FREQUENCY RECEIVERS

The stiffness as a function of the location on the beam is indirectly derived from resonance frequency:

$$k_r(y) = \omega_0^2 m_r(y) \tag{6.3}$$

$m_r(y)$ is the equivalent mass of the beam:

$$m_r(y) = \rho W_r h \int_0^{L_r} \frac{Z_{mode}(y')^2 (dy')}{Z_{mode}(y)^2} \tag{6.4}$$

The switching condition is when the displacement of the beam reaches the switch gap g_{switch}. The mode shape of the free-free beam dictates that the location on the beam that has the maximum displacement is at $y=0$:

$$x(y = 0) = g_{switch} \tag{6.5}$$

The solution of v_i that satisfies the switching condition is the sensitivity of the resoswitch in voltage. The above relations also indicate that thinner beams have better sensitivity, so do smaller switch gaps. Table 1 shows the design parameters for the free-free beam resoswitch. With $g_{switch} = 10nm$, $v_i = 360\mu V$. The sensitivity power is the power injected into the device while driving by $v_i = 360\mu V$:

$$Sensitivity = \frac{v_i^2}{2R_x} \tag{6.6}$$

$$R_x^{-1} = \int\int_{L_1}^{L_2} \frac{\frac{\omega_0 Q V_P^2 (\epsilon W_r)^2}{g^4 k_r(y')} Z_{mode}(y)}{Z_{mode}(y')} dy' dy \tag{6.7}$$
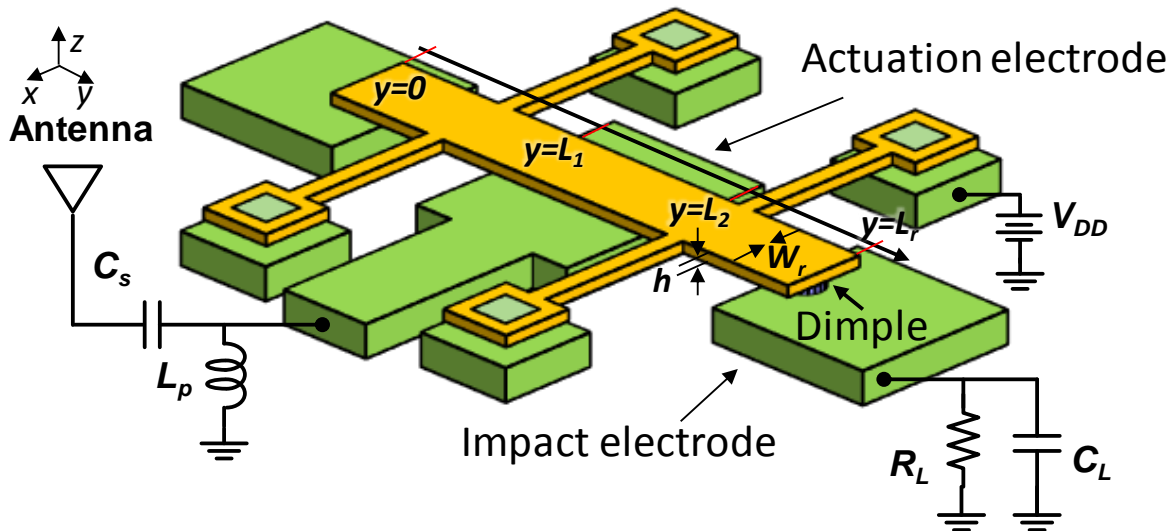

Figure 73: The schematic of the free-free beam resoswitch. The beam has larger displacement at the tips than in the center. The actuation electrode drives the beam into resonance and the tips make switching impacts with the impact electrodes, charging the electrode to V_{DD}.

For $V_P = 3.5V, R_x = 647$ Ω and the resoswitch has a sensitivity of -70dBm.

6.3 PRELIMINARY EXPERIMENTAL RESULTS AND FUTURE WORK

The process challenges described in section 6.1 settles on the contradiction of thermal budget. The as-deposit in-situ doped polySi is too stressed and highly resistive, but the sacrificial Al_2O_3 cannot withstand the annealing process normally required to alleviate stress and active dopants. One other temporary solution for annealing is local annealing, either by passing current through the structure or by laser pulses. Figure 74 shows the frequency response of a released free-free beam after laser pulse annealing. The resonator has only a Q of about 1000. Laser trimming reduces the stress so that the beam is no longer shorted to the electrode, but high power laser pulse also damages the structure. The laser pulse recipe needs more work to optimize and might result in a higher Q factor.

Another high-Q material is SiGe [76]. Doped poly SiGe not only has tens of thousands of Q factor, but also more importantly, has very low deposition temperature that is compatible with metal processes [77].

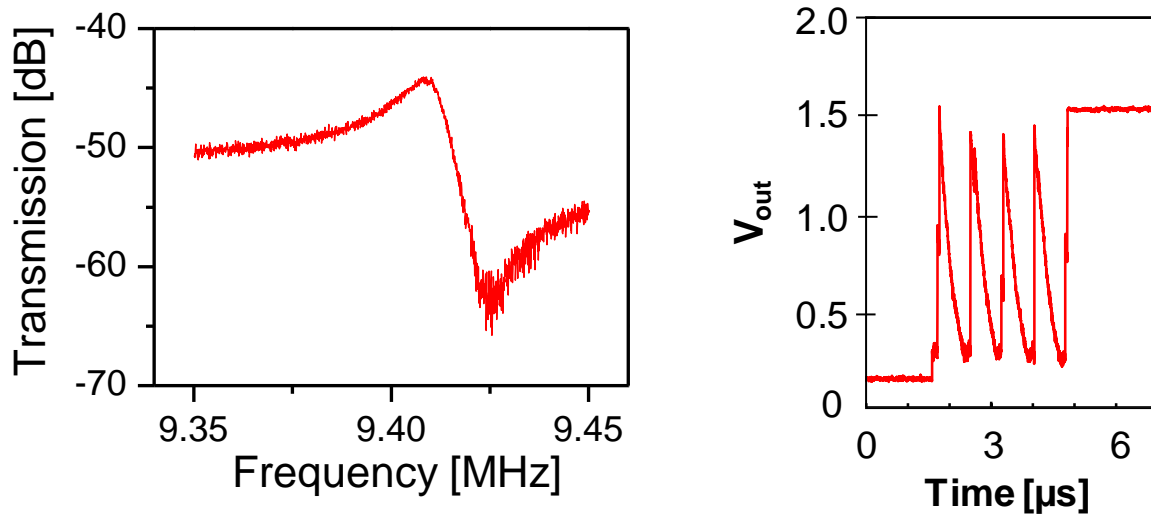Figure 74: (Left): The frequency response of the free-free beam resonator. (The main design is at 53MHz as described, but the cleanest measurement as shown in this figure comes from a ~10MHz resonator. The 53MHz devices unfortunately did not yield any valuable data). (Right): The switching waveform of the 10MHz beam in the left figure. The 10MHz beam switched a few cycles and then permanently welded to the electrode.

CHAPTER 6 HIGH FREQUENCY RECEIVERS

When trying to operate the free-free beam as resoswitch, using the configuration shown in Figure 73, the beam notably switches for a few cycles before it permanently crashed to the electrode. There are several possible causes to the catastrophic failure.

i) The contact resistance is high, so that it takes a much larger input voltage and input force to drive the beam into harder contact to detect any voltage change at impact electrodes. The bias voltage is applied onto the actuation electrode but the ac drive input is connected to the beam structure. Increasing either bias voltage or ac drive amplitude increases the force by the same amount, but V_P is limited by pull-in voltage. If the needed ac input amplitude to make low-resistance contact is too high, the moment the contact is formed, high ac currents pass through the contact and welds the resonator to the contact electrodes.

ii) The mode shape of the free-free beam is a bit different from the simulation model. Upon contact, the tips of the beam pivot on the contact electrode and the beam continues to deform as shown in Figure 74. If the center portion of the beam deflect enough to make contact with the actuation electrode that is biased at V_P, the beam might weld to the actuation electrode.

iii) The beam does not have sufficient restoring force to counteract the contact stiction, especially during hot contacts when charge transfer between the beam and the contact electrode.

The dominant failure mechanism and solutions need further analysis. The free-free beam resoswitch applies the zero quiescent power receiver technology to MHz frequency range,
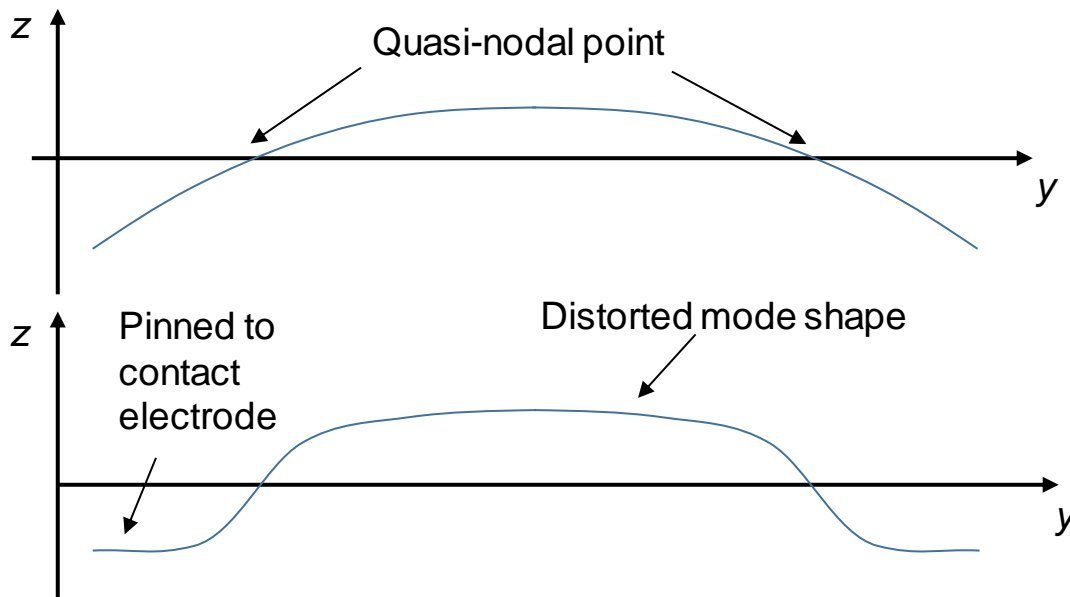
Figure 75: Illustration of the distorted mode shape after impact. The tips of the beam act like a pivotal anchor and the center portion of the beam continues to move.

CHAPTER 6 HIGH FREQUENCY RECEIVERS

allowing all-mechanical receivers to take advantage of the existing infrastructure such as the ubiquitous AM and FM radio stations. Most cell phones, wearables and other mobile devices carry radios compatible with AM or FM communications. Without the cost of building a complete new network system, the all-mechanical receivers can readily integrate into mobile devices and reduce the power consumption of the communication module by orders of magnitude!

W_r	1μm	k_m	214 N/m
L_r	5.3μm	C_x/C_0	9.2%
h	0.2μm	*Sensitivity*	-70dBm
g	20nm	$f_{effective}$	53MHz
$V_{pull\text{-}in}$	5.12V	Q	50000

Table 1: Design parameters of the free-free beam resoswitch

Chapter 7 CONCLUSION

MEMS Resoswitch has previously demonstrated its unique ability to improve switching reliability and its potential to reduce actuation voltage for power converter applications. The demonstration of a five-stage mechanical charge pump that successfully charged V_{DD} of 1V to V_{out} of 5V showed almost zero voltage drop across the switch itself, greatly improving charge pump efficiency comparing to diode based charge pumps. Mechanical devices can also withstand a much higher breakdown voltage, therefore enabling charge pumps to obtain even larger voltage multiplier. The resoswitch power amplifier also successfully demonstrated more than 10dB of power gain using high-Q Al disk resoswitch devices.

This thesis further explores the resoswitch's resonance impact dynamics. The frequency selectivity of the resonance behavior offers inherent filtering functionality. At the same time, the switching operation periodically connects output to voltage source V_{DD}, delivering power. The filter and amplifier combination perfectly satisfies the front-end operations of wireless receivers. With channel-select filtering, the interferers disappear right after the antenna before they have a chance to produce spurious signals. Then the amplifier that follows can become a nonlinear switch. Without the interferers, the switching amplification would suffice the front-end gain. Since the linearity required by the dynamic range is one of the major power hogs, the resoswitch's channel selection and switching amplification together consume orders of magnitude lower power.

The resoswitch is also a passive MEMS device in nature. The mechanical devices consume zero power when in standby. In the case of the resoswitch receiver front-end, the receiver can be armed and listening without consuming any power. For many applications, from cell phones to medical sensors such as blood sugar monitors, the wireless devices listening constantly is essential to reliable communications and even to patients' qualities of life. Especially in applications with low duty cycle, the receiver listening in standby would spend most of the power in the battery. This thesis demonstrated, the first in its kind, an all-mechanical receiver consuming zero power when the receiver is listening. The receiver successfully detected and demodulated a FSK input of -60dBm power in an OOK fashion, sufficient sensitivity for low-speed wireless standards.

Even when the resoswitch receiver is actively receiving, energy is only spent to charge the loading capacitance. Unlike transistor-based switch that suffers from finite leakage current, the mechanical resoswitch has an isolating air gap through which the leakage current is negligible. The loading capacitance is mostly the input capacitance of the digital circuitry of the next stage. On-chip

components can have input capacitance of as little as a few femto-Farads, which translates to several pico-watts of power consumption for receiving the data with a bit rate of 1k bps.

For the current conventional wireless receivers, sleep/wake strategy is necessary to minimize average power consumption. The power bottleneck becomes the clock that regulates sleep and wake cycles in each sensor node. This thesis also proposed a wireless clock scheme in place of the traditional local clock composed of an oscillator with a positive feedback. The oscillator-based clock is very power hungry. A typical real time clock off the market consumes 1μW of power. If receivers can also pick up clock signals wirelessly from a base station, then power consumption of the clock can reduce by hundreds of times. The wireless clock generator in this thesis successfully obtained clock signals using resoswitch receiver consuming tens of nano-watts of battery power.

7.1 FUTURE RESEARCH DIRECTIONS

The resoswitches face many challenges such as frequency stability, switch reliability and so on. The frequency stability is directly responsible for the error rate the receiver. Resoswitches intentionally introduce impact disturbance to resonance dynamics, creating frequency jitters and unreliable impacts. The modeling for this phenomenon is still rough and preliminary. In order to improve the resoswitch's switching frequency stability, more experiments and modeling are needed to further understand and control the switching dynamics.

Another important aspect of switching is the contact reliability. Switching reliability has always been one of the most serious shortcomings for mechanical switches. Resoswitches suffer from the same contact degradation issue over time, but less contact stiction problem. The reliability is also highly dependent on the contact material. More work is needed from both process and measurement characterization point of view to study the reliability of the resoswitches.

7.2 CONCLUDING REMARKS

In summary, this dissertation introduced and analyzed the first all-mechanical receiver that consumes zero quiescent power when listening and consumes only tens of nano-watts of power when actively receiving. The resoswitch receiver successfully detected and demodulated FSK input signal of -68dBm, all while consuming zero quiescent power. This dissertation also demonstrated the resoswitch serving as a mechanical clock generator to regulate sleep/wake cycles in traditional receivers, consuming hundreds of time less battery power.

BIBLIOGRAPHY

[1] J. Rabaey, M. Ammer, J. d. Silva, D. Patel and S. Roundy, "PicoRadio supports ad hoc ultra-low power wireless networking," *Computer,* vol. 33, no. 7, pp. 42-48, 2000.

[2] J. Bryzek, "Roadmap for the Trillion Sensor Universe," iNEMI Spring Member Meeting and Webinar, Berkeley, 2013.

[3] A. Rowe, R. Mangharam and R. Rajkumar, "FireFly: A Time Synchronized Real-Time Sensor Networking Platform," in *Wireless Ad Hoc Networking: Personal-Area, Local-Area, and the Sensory-Area Networks*, CRC Press Book, 2006.

[4] E. H. Armstrong, "The super-heterodyne-its origin, development, and some recent improvements," *Radio Eng. Proc. Inst. Of,* vol. 12, no. 5, pp. 539-552, 1924.

[5] B. Razavi, RF Microelectronics 2nd ed., New York: Prentice Hall, 2011.

[6] C. Toumazou, Trade-Offs in Analog Circuit Design: The Designer's Companion, Springer, 2004.

[7] A. I. Zverev, Handbook of Filter Synthesis, New York: Wiley, 1967.

[8] I. Hunter, Theory and Design of Microwave Filters, IET, 2001.

[9] K. Lakin, G. Kline and K. McCarron, "High-Q microwave acoustic resonators and filters," *IEEE Transactions on Microwave Theory and Techniques,* vol. 41, no. 12, pp. 2139-2146, 1993.

[10] R. Ruby, P. Bradley, D. Clark, D. Feld, T. Jamneala and K. Wang, "Acoustic FBAR for filters, duplexers and front end modules," in *IEEE MTT-S International Microwave Symposium Digest*, 2004.

[11] R. G. Kinsman, "A history of crystal filters," in *Frequency Control Symposium*, 1998.

[12] M. Akgul, "A passband-corrected high rejection channel-select micromechanical disk filter," in *IFCS*, Taipei, 2014.

[13] S.-S. Li, Y.-W. Lin, Z. Ren and C.-C. Nguyen, "A micromechanical parallel-class diskarray filter," in *IEEE International Frequency Control Symposium*, 2007.

[14] J. Naghsh Nilchi, R. Liu and C.-C. Nguyen, "7th order sharp-roll-off bridged micromechanical filter," *Transducers,* 2015.

[15] F. Lin and M. Rais-Zadeh, "Tunable RF MEMS Filters: A Review," in *Encyclopedia of Nanotechnology*, Dordrecht, Springer Netherlands, 2016, pp. 4233-4243.

[16] J. Lowe, "Enhanced WWVB Broadcast Format," in *Time and Frequency Services*, NIST, 2012.

[17] Y. Lin, W.-C. Li, Z. Ren and C. T.-C. Nguyen, "The micromechanical resonant switch ("Resoswitch")," in *Hilton Head*, 2008.

[18] Y. Lin, R. Liu, W.-C. Li, M. Akgul and C. T.-C. Nguyen, "A micromechanical resonant charge pump," in *Solid-State Sensors, Actuators and Microsystems (TRANSDUCERS & EUROSENSORS XXVII), 2013 Transducers & Eurosensors XXVII: The 17th International Conference on*, Barcelona, 2013.

[19] J. B. Muldavin and G. M. Rebeiz, "High-isolation CPW MEMS shunt switches. 1. Modeling," *IEEE Transactions on Microwave Theory and Techniques,* vol. 48, no. 6, pp. 1045-1052, 2000.

[20] W. C. Li, Z. Ren and C. T. C. Nguyen, "A micromechanical high-Q elliptic disk displacement amplifier," in *2016 IEEE 29th International Conference on Micro Electro Mechanical Systems (MEMS)*, Shanghai, 2016.

[21] W.-C. Li, Y. Lin and C. T.-C. Nguyen, "Metal micromechanical filter-power amplifier utilizing a displacement-amplifying resonant switch," in *Solid-State Sensors, Actuators and Microsystems (TRANSDUCERS & EUROSENSORS XXVII), 2013 Transducers & Eurosensors XXVII: The 17th International Conference on*, Barcelona, 2013.

[22] G. M. Rebeiz, K. Entesari, I. C. Reines, S.-j. Park, M. A. El-tanani and A. Grichener, "Tuning in to RF MEMS," *IEEE Microwave Magazine,* 2009.

[23] W. Tang, T.-C. H. Nguyen, M. Judy and R. Howe, "Electro- static-comb drive of lateral polysilicon resonators," *Sensors and Actuators,* Vols. A21-23, pp. 328-331, 1990.

[24] G. M. Rebeiz, RF MEMS: Theory, Design, and Technology, John Wiley & Sons, 2004.

[25] W. C. Tang, M. G. Lim and R. T. Howe, "Electrostatic Comb Drive Levitation and Control Method," *Journal of Microelectromechanical Systems,* vol. 1, no. 4, pp. 170-175, 1992.

[26] S. Shaw and P. Holmes, "A Periodically Forced Piecewise Linear Oscillator," *Journal of Sound and Vibration,* vol. 90, no. 1, pp. 129-155, 1983.

[27] S. S and H. PJ, "A Periodically Forced Impact Oscillator With Large Dissipation," *ASME. J. Appl. Mech.,* vol. 50, no. 4a, pp. 849-857, 1983.

[28] H. P. Gavin, "Numerical integration in strucural dynamics," Duke University, 2016.

[29] W. J. Stronge, Impact Mechanics, Cambridge University Press.

[30] ANSYS, "ANSYS Simulator Training Manual," 2005.

[31] A. Smith-Baumann and F. Gicquel, "FEA Documentation and Standards," 2005. [Online]. Available: http://www-eng.lbl.gov/~als/FEA/.

[32] R. H. Rand, "Lecture Notes on Nonlinear Vibrations," Cornell University, Ithaca, 2012.

[33] D. W. Jordan and P. Smith, Nonlinear Ordinary Differential Equations: An Introduction for Scientists and Engineers, Oxford Universtiy Press, 2007.

[34] I. Kovacic and M. Brennan, "The Duffing Equation: Nonlinear Oscillators and their Behaviour, First Edition," John Wiley & Sons, Ltd., 2011.

[35] P. M. Zavracky, S. Majumder and N. McGruer, "Micromechanical switches fabricated using Nickel surface micromachining," *JOURNAL OF MICROELECTROMECHANICAL SYSTEMS,* pp. 3-9, 1997.

[36] S. Majumder, N. E. McGruer, P. M. Zavracky, G. G. Adams, R. H. Morrison and J. Krim, "Measurement and modelling of surface micromachined, electrostatically actuated microswitches," in *Solid State Sensors and Actuators (Transducers)*, Chicago, 1997.

[37] C.-W. Baek, Y.-K. Kim, Y. Ahn and Y.-H. Kim, "Measurement of the mechanical properties of electroplated gold thin films using micromachined beam structures," *Sensors and Actuators A: Physical,* vol. 117, no. 1, pp. 17-27, 2005.

[38] A. Gole and C. J. Murphy, "Seed-Mediated Synthesis of Gold Nanorods: Role of the Size and Nature of the Seed," *Chem. Mater.,* vol. 16, no. 19, pp. 3633-3640, 2004.

[39] B. Pillans, J. Kleber, C. Goldsmith and M. Eberly, "RF power handling of capacitive RF MEMS devices," in *Microwave Symposium Digest, 2002 IEEE MTT-S International*, 2002.

[40] Y. Lin, "Low phase noise micromechanical reference oscillators for wireless communications," *Ph.D. dissertation, University of Michigan, Ann Arbor, MI, USA,* 2007.

[41] T. L. Naing, "2.97-GHz CVD diamond ring resonator with Q >40,000," in *IFCS*, 2012.

[42] Y. Lin, R. Liu, W.-C. Li and C.-C. Nguyen, "Polycide Contact Interface to Suppress Squegging in Micromechanical Resoswitches," in *MEMS*, San Francisco, 2014.

[43] V. Bansal, H. Jani, J. Plessis, P. Coloe and S. Bhargava, "Galvanic Replacement Reaction on Metal Films: A One-Step Approach to Create Nanoporous Surfaces for Catalysis," *Advanced Materials,* vol. 20, no. 4, pp. 717-723, 2008.

[44] X. H. Xia, C. M. A. Ashruf, P. J. French and J. J. Kelly, "Galvanic Cell Formation in Silicon/Metal Contacts: The Effect on Silicon Surface Morphology," *Chem. Mater.,* vol. 12, no. 6, pp. 1671-1678, 2000.

[45] J. R. Johler, "Propagation of the Low-Frequency Radio Signal," *Proceedings of the IRE,* vol. 50, no. 4, pp. 404-427, 1962.

[46] R. Nathanael, V. Pott, H. Kam, J. Jeon and T.-J. K. Liu, "4-terminal relay technology for complementary logic," in *IEDM*, Washington, 2009.

[47] C. T.-C. Nguyen, "MEMS Technology for Timing and Frequency Control," *IEEE Transactions on Ultrasonics, Ferroelectrics, and Frequency Control,* vol. 54, no. 2, pp. 251-270, 2007.

[48] R. A. Johnson, Mechanical Filters in Electronics, New York, NY: Wiley, 1983.

[49] C-MAX, "CMMR-6 data sheet," 2007.

[50] H. G. Barrow, T. L. Naing, R. A. Schneider, T. O. Rocheleau, V. Yeh, Z. Ren and C. T.-C. Nguyen, "A real-time 32.768-kHz clock oscillator using a 0.0154-mm2 micromechanical resonator frequency-setting element," in *Frequency Control Symposium (FCS), 2012 IEEE International*, 2012.

[51] R. Liu, J. Naghsh Nilchi, T. Naing and C.-C. Nguyen, "Zero Quiescent Power VLF Mechanical Communication Receiver," in *Transducers*, Anchorage, 2015.

[52] J. Brank, J. Yao, M. Eberly, A. Malczewski, K. Varian and C. Goldsmith, "RF MEMS-based tunable filters," *Int J RF and Microwave Comp Aid Eng,* vol. 11, no. 5, pp. 276-284, 2001.

[53] R. Nathanael, V. Pott, H. Kam, J. Jeon and T.-J. King Liu, "4-terminal relay technology for complementary logic," in *IEDM*, 2009.

[54] S. Majumder, N. McGruer, G. Adams, P. Zavracky, R. Morrison and J. Krim, "Study of contacts in an electrostatically actuated microswitch," *Sensors and Actuators A: Physical,* vol. 93, no. 1, pp. 19-26, 2001.

[55] Y. Lin, R. Liu, W.-C. Li and C.-C. Nguyen, "Polycide contact interface to suppress squegging in micromechanical resoswitches," in *MEMS*, San Francisco, 2014.

[56] S. Shaw and P. Holmes, "A periodically forced piecewise linear oscillator," *Journal of Sound and Vibration,* vol. 90, no. 1, pp. 129-155, 1983.

[57] E. Lee and J. Rabaey, "The Swarm at the Edge of the Cloud," *IEEE Design & Test,* vol. 31, no. June, pp. 8-20, June 2014.

[58] Y. Lin, W.-C. Li, Z. Ren and C.-C. Nguyen, "The micromechanical resonant switch ("resoswitch")"," in *Hilton Head*, 2008.

[59] R. Liu, J. Naghsh Nilchi, W.-C. Li and C.-C. Nguyen, "Soft-Impacting Micromechanical Resoswitch," in *MEMS*, Shanghai, 2016.

[60] A.-C. Wong and C.-C. Nguyen, "Micromechanical mixer-filters ("mixlers")," *J. Microelectromech. Syst.,* vol. 13, no. Feb., pp. 100-112, 2004.

[61] Y. Lin, R. Liu, W.-C. Li and C.-C. Nguyen, "Polycide contact interface to suppress squegging in micromechanical resoswitches," in *MEMS*, San Francisco, 2014.

[62] R. Liu, J. Naghsh Nilchi and C. T.-C. Nguyen, "RF-Powered Micromechanical Clock Generator," in *IFCS*, New Orleans, 2016.

[63] R. Liu, J. Naghsh Nilchi, W.-C. Li and C. T.-C. Nguyen, "Soft-Impacting Micromechanical Resoswitch Zero Quiescent Power AM Receiver," in *MEMS*, Shanghai, China, 2016.

[64] C. Budd and F. Dux, "Chattering and Related Behaviour in Impact Oscillators," *Philosophical Transactions of the Royal Society of London. Series A: Physical And Engieering Sciences,* vol. 347, no. 1683, pp. 365-389, 1994.

[65] Budd, C. and Dux, F., "The effect of frequency and clearance variations on single-degree-of-freedom impact oscillators," *Journal of Sound and Vibration,* vol. 184, no. 3, pp. 475-502, 1995.

[66] W.-T. Hsu and C. T.-C. Nguyen, "Stiffness-compensated temperature-insensitive micromechanical resonators," in *IEEE International Conference on Micro Electro Mechanical Systems*, Las Vegas, 2002.

[67] M. Hikita, H. Kojima, T. Tabuchi and Y. Kinoshita, "800-MHz high-performance SAW filter using new resonant configuration," *Microw. Theory Tech. IEEE Trans. On,* vol. 33, no. 6, pp. 510-518, 1985.

[68] S.-S. Li, Y.-W. Lin, Z. Ren and C.-C. Nguyen, "An MSI micromechanical differential diskarray filter," in *Solid-State Sensors, Actuators and Microsystems Conference, TRANSDUCERS*, 2007.

[69] J. Mitola, "The software radio architecture," *Commun. Mag. IEEE,* vol. 33, no. 5, pp. 26-38, 1995.

[70] L. L. W. Chow, J. L. Volakis, K. Saitou and K. Kurabayashi, "Lifetime Extension of RF MEMS Direct Contact Switches in Hot Switching Operations by Ball Grid Array Dimple Design," *IEEE Electron Device Letters,* vol. 28, no. 6, pp. 479-481, 2007.

[71] R. Chan, R. Lesnick, D. Becher and M. Feng, "Low-actuation voltage RF MEMS shunt switch with cold switching lifetime of seven billion cycles," *Journal of Microelectromechanical Systems ,* vol. 12, no. 5, pp. 713-719, 2003.

[72] C. A. Wilson, R. K. Grubbs and S. M. George, "Nucleation and Growth during Al2O3 Atomic Layer Deposition on Polymers," *Chem. Mater.,* vol. 17, no. 23, pp. 5625-5634, 2005.

[73] J. W. Elam, C. A. Wilson, M. Schuisky, Z. A. Sechrist and S. M. George, "Improved nucleation of TiN atomic layer deposition films on SiLK low-k polymer dielectric using an Al2O3Al2O3 atomic layer deposition adhesion layer," *Journal of Vacuum Science & Technology B, Nanotechnology and Microelectronics: Materials, Processing, Measurement, and Phenomena,* vol. 21, no. 3, 2003.

[74] S. D. Senturia, Microsystem Design, springer, 2001.

[75] R. H. Olsson, C. M. Washburn, J. E. Stevens, M. R. Tuck and C. D. Nordquist, "VHF and UHF mechanically coupled aluminum nitride MEMS filters," in *IEEE International Frequency Control Symposium*, 2008.

[76] A. Franke, J. Heck, T.-J. King and R. Howe, "Polycrystalline silicon-germanium films for integrated microsystems," *Journal of Microelectromechanical Systems,* vol. 12, no. 2, pp. 160-171, 2003.

[77] C. W. Low, T.-J. K. Liu and R. T. Howe, "Characterization of Polycrystalline Silicon-Germanium Film Deposition for Modularly Integrated MEMS Applications," *Journal of Microelectromechanical Systems,* vol. 16, no. 1, pp. 68-77, 2007.

[78] M. Akgul, L. Wu, Z. Ren and C. T. C. Nguyen, "A negative-capacitance equivalent circuit model for parallel-plate capacitive-gap-transduced micromechanical resonators," *IEEE Transactions on Ultrasonics, Ferroelectrics, and Frequency Control,* vol. 61, no. 5, pp. 849-869, 2014.